

**THÈSE DE DOCTORAT  
DE L'UNIVERSITÉ DE LILLE**

**LABORATOIRE DE MÉCANIQUE, MULTIPHYSIQUE ET  
MULTIECHELLE (UMR9013, CNRS)**

Présentée par

**Yudan JIN**

pour obtenir le grade de

**DOCTEUR DE L'UNIVERSITÉ DE LILLE**

Domaine

**GÉNIE CIVIL**

Sujet de la thèse

**Etude expérimentale et modélisation numérique de la  
fissuration par retrait de dessiccation des matériaux  
cimentaires: influences de la rigidité et de la taille des  
inclusions**

**(Experimental study and numerical modeling of drying shrinkage  
related cracking in cement-based materials: influence of inclusion  
stiffness and size)**

Soutenue le 29 Janvier 2021 devant le jury composé de :

<b>J. TORRENTI, Professeur</b>	Université Eiffel	<i>Président du jury</i>
<b>F. BENBOUDJEMA, Professeur</b>	Ecole Normale Supérieure de Paris-Saclay,	<i>Rapporteur</i>
<b>H. WELEMANE, MCF HDR</b>	Ecole Nationale d'Ingénieurs de Tarbes	<i>Rapporteur</i>
<b>J.F. SHAO, Professeur</b>	Université de Lille	<i>Examineur</i>
<b>Y. JIA, MCF HDR</b>	Université de Lille	<i>Examineur</i>
<b>T. ROUGELOT, MCF</b>	Université de Lille	<i>Invité</i>
<b>N. BURLION, Professeur</b>	Université de Lille	<i>Directeur de thèse</i>

**LAMCUBE - UNIVERSITÉ DE LILLE**



## Abstract

Drying shrinkage induced cracking is an essential mechanism to be considered in the durability study of cement-based materials and structures. The present thesis is devoted to experimental investigation and numerical modeling of this mechanism by putting the emphasis on the influences of inclusion stiffness and size. The thesis is composed of two parts.

The first part is devoted to experimental study. A series of concrete samples are first casted with artificial inclusions of different rigidities. These samples are subjected to different levels of drying in order to evaluate cracks induced by the drying shrinkage. The dried samples are then examined by using the non-destructive X-ray micro-tomography imaging method. Three-dimensional (3D) distributions of induced cracks in the dried samples are identified, including their location and shape. The influence of inclusion rigidity on the shrinkage induced cracking process is clearly demonstrated. It is found that the shrinkage-induced cracking is strongly enhanced by the stiffness difference between the inclusion and cement paste. Secondly, samples casted with glass balls of different sizes are considered. By using a similar experimental procedure, the influences of inclusion size on the drying shrinkage induced cracking process are investigated.

In the second part, a numerical method based on the peridynamic theory is proposed. The formulation and implementation of the numerical method are first presented and discussed. Its efficiency in modelling the initiation and propagation of multiple cracks in heterogeneous materials is then demonstrated. The proposed method is further applied to the description of cracking process induced by drying shrinkage and temperature change in concrete composites containing different types of inclusions. The emphasis is put on the effects of inclusion stiffness and size on cracking patterns. A series of numerical simulations are performed. Comparisons between numerical results and experimental observations are presented.

**Keywords:** Cement composites, concrete, drying shrinkage, cracking, peridynamics, numerical modeling



## Résumé

La fissuration induite par le retrait de dessiccation est un mécanisme essentiel à prendre en compte dans l'étude de la durabilité des matériaux et structures à base de ciment. La présente thèse est consacrée à l'étude expérimentale et à la modélisation numérique de ce mécanisme en mettant l'accent sur les influences de la rigidité et de la taille des inclusions. La thèse est composée de deux parties.

La première partie est consacrée à l'étude expérimentale. Une série d'échantillons de béton sont d'abord préparés avec des inclusions artificielles de différentes rigidités. Ces échantillons sont soumis à différents niveaux de séchage afin d'évaluer les fissures induites par le retrait de séchage. Les échantillons séchés sont ensuite examinés à l'aide de la méthode non destructive de micro-tomographie au rayon X. Les distributions tridimensionnelles (3D) des fissures induites dans les échantillons séchés sont identifiées, y compris leur emplacement et leur forme. L'influence de la rigidité d'inclusion sur le processus de fissuration induite par le retrait est clairement démontrée. On constate que la fissuration induite par le retrait est fortement amplifiée par la différence de rigidité entre l'inclusion et la pâte de ciment. Deuxièmement, des échantillons coulés avec des billes de verre de différentes tailles sont étudiés. En utilisant une procédure expérimentale similaire, les influences de la taille des inclusions sur le processus de fissuration induite par le retrait de séchage sont étudiées.

Dans la deuxième partie, une méthode numérique basée sur la théorie de la périodynamique est proposée. La formulation et la mise en œuvre de la méthode numérique sont d'abord présentées et discutées. Son efficacité dans la modélisation de l'initiation et de la propagation de fissures multiples dans des matériaux hétérogènes est ensuite démontrée. La méthode proposée est ensuite appliquée à la description du processus de fissuration induit par le retrait de séchage et le changement de température dans les composites de béton contenant différents types d'inclusions. L'accent est mis sur les effets de la rigidité et de la taille des inclusions sur les modèles de fissuration. Une série de simulations numériques est réalisée. Des comparaisons entre les résultats numériques et les observations expérimentales sont présentées.

**Mots clés:** Composites de ciment, béton, retrait au séchage, fissuration, périodynamique, modélisation numérique



## Acknowledgements

It has been a wonderful experience pursuing my doctoral study at Laboratoire de Mécanique, Multiphysique et Multiéchelle (LaMcube). In this exciting moment, I want to express my gratitude to all those who has helped me during the last three years.

First of all, I want to thank my supervisor, Prof. Nicolas BURLION, for his useful suggestions, incisive comments as well as constructive criticism that have contributed greatly to the completion of my thesis.

I also deeply grateful for the help of Prof. Jian-Fu SHAO. Without his precious guidance, patience, confidences and encourage during three years of my research, this thesis and others not covered in would undoubtedly never have achieved fruition.

I am deeply grateful to Ms. Yun JIA for her constant support and help both in academic field and my life during my study in France, starting from my undergraduate studies. I also do appreciate the suggestion and help from Mr. Han-Bing BIAN, Mr. Thomas ROUGELOT and Mr. Qi-Er WU.

Great thanks also give to all the members of the research group in LaMcube, including Mr. Wan-Qing SHEN, Dr. Yu-Long ZHANG, Dr. Bei HAN, Dr. Ya-Jun CAO, Dr. Lun-Yang ZHAO, Dr. Zhan YU, Dr. Yue SUN, Dr. Hai-Ling SHI, Dr. Dong-Mei ZHANG, Dr. Xi CHEN, Dr. Yue TONG, Dr. Jian-Jian ZHAO, Dr. Jue-Liang CHEN, Dr. Si-Yu LIU, Dr. Li-Ping ZHU, Dr. Wang ZHANG ... They gave me not only many help in the research, but also provide much assistance, specially for life.

Last but not least, I have to give a great appreciation to my parents for their unconditional support and encouragement during my academic career. Without their constant support, I would never have had a chance to start and finish a PhD or even to come to study in France.

Finally, I want to thank my husband, WANG Meng. There is so much to say but so little that can be expressed. His unconditional support and help during my PhD, both in my studies and my life, was the most important factor in the success of my doctoral career.

These were the most challenging but exciting three years I have had. Thank you to everyone I have met along the way.

Yudan JIN





# Contents

<b>Contents</b>	<b>i</b>
<b>List of Figures</b>	<b>v</b>
<b>List of Tables</b>	<b>xi</b>
<b>General Introduction</b>	<b>1</b>
<b>I State of the Art</b>	<b>7</b>
1 Introduction . . . . .	7
2 Experimental observations of micro or meso-structure of cementitious materials . . . . .	8
2.1 Experimental observation methods . . . . .	8
2.2 Structural composition of cementitious materials . . . . .	10
2.3 Mechanism of drying shrinkage cracking . . . . .	11
2.4 Contribution of various factors in drying shrinkage cracks . . . . .	13
3 Description of mechanical behavior for cracked concrete . . . . .	18
3.1 Fracture mechanics . . . . .	18
3.2 Damage mechanics . . . . .	20
3.3 Meso and micro-scale model . . . . .	21
4 Overview of modeling methods for concrete materials . . . . .	24
4.1 Local methods and their limitations . . . . .	24
4.2 Non-local methods . . . . .	26
<b>II Experimental Study of the Drying and Cracking of Cement-based Materials by X-Ray Microtomography</b>	<b>29</b>
1 Introduction . . . . .	29
2 Effect of inclusions rigidity . . . . .	30
2.1 Sample preparation and experimental program . . . . .	30
2.2 Experimental results . . . . .	31
3 Effect of the inclusions size . . . . .	36
3.1 Sample preparation and experimental program . . . . .	36
3.2 Experimental results . . . . .	43

4	Concluding remarks . . . . .	48
<b>III Peridynamic Model of Concrete and Numerical Verification</b>		<b>49</b>
1	Introduction . . . . .	49
2	Bond-based peridynamic theory . . . . .	50
2.1	Prototype microelastic brittle model (PMB) . . . . .	53
2.2	Generalized prototype microelastic brittle model (GPMB) . . . . .	55
3	Numerical implementation . . . . .	58
3.1	Spatial discretization and correction . . . . .	58
3.2	Time integration . . . . .	60
4	Numerical simulations . . . . .	63
4.1	Bar under tension . . . . .	63
4.2	Cantilever beam under transverse loading . . . . .	70
5	Concluding remarks . . . . .	71
<b>IV An Improved Bond-based Peridynamics Model for Heterogeneous Concrete Materials</b>		<b>73</b>
1	Introduction . . . . .	73
2	Mesoscale Modeling of concrete . . . . .	74
2.1	Mesoscopic constituents . . . . .	74
2.2	Modeling methods . . . . .	76
3	Damage prediction . . . . .	77
4	Numerical simulations . . . . .	80
4.1	Validation of the numerical implementation . . . . .	80
4.2	Analysis of shrinkage and heating induced cracking . . . . .	84
5	Concluding remarks . . . . .	94
<b>V A Fully Coupled Hydro-mechanical Peridynamic Model for Saturated and Partially Saturated Porous Media</b>		<b>97</b>
1	Introduction . . . . .	97
2	Development of a coupled hydro-mechanical peridynamic model for saturated porous medium . . . . .	98
2.1	Peridynamic thermal diffusion coupling with hydro-mechanics . . . . .	99
2.2	Linear poroelastic constitutive equations in peridynamics . . . . .	100
2.3	Peridynamic motion equations coupling with hydro-mechanical process	101
2.4	Fluid flow state peridynamic equation for porous medium . . . . .	101

---

3	Extension to the partially saturated porous medium . . . . .	102
3.1	Peridynamic motion equation for partially saturated porous medium	103
3.2	Fluid flow state peridynamic equation for partially saturated porous medium . . . . .	103
4	Numerical simulations . . . . .	104
4.1	Validation of proposed numerical model . . . . .	104
4.2	Numerical analysis of drying shrinkage cracking . . . . .	110
4.3	Influence of inclusion size on drying shrinkage cracks . . . . .	115
5	Concluding remarks . . . . .	117
<b>VI Conclusions and Perspectives</b>		<b>119</b>
1	Conclusions . . . . .	119
2	Perspectives . . . . .	120
<b>Bibliography</b>		<b>123</b>



# List of Figures

I .1	Localization maps of the AE events from the beginning (0%) to the given loading stage in D2 beam as function of absolute acoustic energy (aJ) (Alam et al., 2014) . . . . .	8
I .2	Snapshot of the UAV during the flight to scan bridge and a captured thermal image indicating potential delaminated areas (Omar and Nehdi, 2017) . . . .	9
I .3	Micrographs of thin petrographic section illustrating micro-crack maps at four stress levels (Malek et al., 2017) . . . . .	9
I .4	3D Segmented phases without load: (a) Aggregate; (b) Motar; (c) Voids and pores; (d) Combined concrete (Yang et al., 2017) . . . . .	10
I .5	3D segmented phases after load: (a) voids and cracks; (b) Combined concrete; (c) Failed specimen at peak load (Yang et al., 2017) . . . . .	10
I .6	Schematic diagram of meso-structure of cementitious materials . . . . .	11
I .7	Concrete wall exposed to drying: (a) Distribution of relative humidity at different drying times; (b) Inhomogeneous distribution of shrinkage strain; (c) Induced stress and cracking due to restoration of compatibility conditions (Bazant, 1988). . . . .	12
I .8	Microcracks observed in drying sample (Wong et al., 2009). . . . .	12
I .9	Crack patterns observed in shrinkage tests(Hsu et al., 1963). . . . .	14
I .10	Two-dimensional structure with a given size distribution of the aggregates: (a) spherical geometry; (b) polygons geometry; (c) given morphological law (Wittmann et al., 1985). . . . .	14
I .11	Total length of drying shrinkage microcracking (TCL) in studied cement composites and cement paste (AVP:aggregate volume percentage, G.5: 2mm, G1: 1mm, G2: 2mm, G4: 4mm, G6: 6mm) (Bisschop and Van Mier, 2002a) 15	15
I .12	Maximum depth of drying shrinkage microcracking (MCD) in cementitious composites and cement paste (Bisschop and Van Mier, 2002a) . . . . .	15
I .13	(a) Specific crack length and (b) average crack width versus aggregate diameter $\phi$ (Grassl et al., 2010) . . . . .	16

I .14	Effect of aggregate size on induced drying shrinkage microcracking in the composites with 35% aggregates. Upper row: maps of drying shrinkage microcrack; Lower row: orientations of microcracking (Bisschop and Van Mier, 2002a) . . . . .	17
I .15	(a)Accumulated length and (b) measured width of cracks in different samples . . . . .	18
I .16	Illustration of the hypothesis of the discrete and smeared crack model:(a) Micro-structure; (b) Stress distribution and crack boundary; (c) Discrete crack model; (d) Smeared crack model (Rashid, 1968) . . . . .	20
I .17	Research scale of concrete materials (Wittmann, 1983) . . . . .	22
I .18	(a) Regular triangular lattice of beams; (b) External forces and deformations on a single beam element; (c) Stress-strain relation for an element. (Schlangen and Garboczi, 1997) . . . . .	23
I .19	Relationship among local model, non-local model and molecular dynamics . . . . .	26
II .1	Different inclusions used in this study . . . . .	31
II .2	Evolution of relative humidity and temperature over time . . . . .	33
II .3	Evolution of relative mass loss over time . . . . .	33
II .4	Accumulated length of cracks in different samples (step 2) . . . . .	36
II .5	Illustration of the glass beads and the molds used . . . . .	37
II .6	Evolution of the relative mass variation of the samples with drying time . . . . .	38
II .7	Principle of shrinkage measurement with a retractometer . . . . .	39
II .8	Evolution of the shrinkage of the samples with drying time . . . . .	39
II .9	Evolution of the shrinkage of the samples with relative mass variation of the samples . . . . .	40
II .10	The microtomography equipment (platform ISIS4D) . . . . .	41
II .11	Sketch of acquisition and reconstruction of micro-tomography . . . . .	42
II .12	Images of different samples at the end of the drying procedure . . . . .	44
II .13	Visualization of specimen saturated and after drying process under X-ray microtomography in horizontal and vertical sections ( $D = 3mm$ ) . . . . .	44
II .14	Representative cross-sections of different samples at different steps of drying . . . . .	45
II .15	Crack patterns surround the inclusions . . . . .	46
II .16	Evolution of the 3D crack network in different samples . . . . .	47
III .1	Interactions between the points material . . . . .	50
III .2	Function of the force state in Peridynamics . . . . .	51

III .3	Function of the force state in Peridynamics . . . . .	52
III .4	A two-dimensional plate subjected to isotropic expansion . . . . .	54
III .5	Graphs of different influence functions $\kappa(\xi, \delta)$ . . . . .	56
III .6	Graphs of influence function for current study . . . . .	57
III .7	Uniform discretization under different dimensions . . . . .	58
III .8	Illustration of geometrical discretization and volume correction for the col- location points inside the horizon $H_{x_i}$ . . . . .	59
III .9	Illustration of neighborhood of PD points near an interface . . . . .	60
III .10	Geometry of a bar under tension . . . . .	64
III .11	Displacement of the material point near the middle of the bar as time step increases for different $m$ . . . . .	65
III .12	Displacement variations comparison of peridynamics solutions with different $m$ and analytical solution along the location $0.1m$ to $0.2m$ of the bar . . . .	65
III .13	Variation of the mean value of the difference in displacement of the bar for different values of $m$ . . . . .	66
III .14	Displacement of the material point near the middle of the bar as time step increases for different $\Delta x$ . . . . .	67
III .15	Displacement variations comparison of peridynamics solutions with different $\Delta x$ and analytical solution along the location $0.15m$ to $0.2m$ of the bar . . .	67
III .16	Variation of the mean value of the difference in displacement of the bar for different values of $\Delta x$ . . . . .	68
III .17	Displacement of the material point near the middle of the bar as time step increases for different $\delta$ . . . . .	68
III .18	Displacement variations comparison of peridynamics solutions with different $\delta$ and analytical solution along the location $0.15m$ to $0.2m$ of the bar . . . .	69
III .19	Variation of the mean value of the difference in displacement of the bar for different values of $\delta$ . . . . .	69
III .20	Geometry of cantilever beam under transverse loading . . . . .	70
III .21	Load–displacement curves by using various $\delta$ . . . . .	71
IV .1	Multiphase composition of concrete at the mesoscale . . . . .	75
IV .2	Linear damage model . . . . .	78
IV .3	Crack initiation and propagation . . . . .	78
IV .4	Integration domain of micro-potentials crossing a crack surface . . . . .	79
IV .5	Geometry and boundary conditions of tension test on concrete plate and an example of distribution of pores and aggregates . . . . .	80

IV .6	Global stress-displacement curves in tension test of concrete sample . . . . .	83
IV .7	Cracking patterns in eight selected random micro-structures . . . . .	84
IV .8	Selected representative micro-structure of concrete composite for simplified 2D modelling . . . . .	85
IV .9	Evolution of damage distribution in composite case 3 (glass ball) at three instances of drying process represented by prescribe bond stretch value . . . . .	88
IV .10(a)	Distribution of the equivalent stress in composite case 3 (glass ball); (b) Cracked cross section at the end of step 1 of drying . . . . .	89
IV .11	Distributions of damage for different values of the elastic modulus ratio between inclusions and cement paste . . . . .	90
IV .12	Variation of accumulated crack length and average crack width with inclu- sion elastic modulus for a constant modulus of cement matrix ( $15GPa$ ) . . . . .	91
IV .13	Distributions of damage (a) and of equivalent stress (b) at the end of heating phase . . . . .	93
IV .14	Distribution of damage at the end of cooling phase . . . . .	93
IV .15	Experimental observations of cracked cross section before heating (a) and that after heating-cooling process (b) (Li et al., 2020) . . . . .	94
V .1	Composition of the saturated porous medium . . . . .	98
V .2	Composition of the partial saturated porous medium . . . . .	102
V .3	Biot's one-dimensional consolidation: configuration and applied boundary conditions . . . . .	105
V .4	Comparison of analytical and PD pore pressure along the region . . . . .	106
V .5	Comparison of analytical and PD vertical displacements along the region . . . . .	106
V .6	Desaturation of a sand column: Geometry and boundary conditions . . . . .	107
V .7	Comparison between experimental data and numerical results with PD and FEM results: Evolution of fluid pressure . . . . .	109
V .8	Comparison of FEM and PD results: settlement of sand column . . . . .	109
V .9	Selected representative micro-structure of concrete composite for simplified 2D modelling . . . . .	110
V .10	Distribution of the pore pressure in two composites with different size of inclusions (left: $3mm$ ,right: $2mm$ ) . . . . .	112
V .11(a)	Location of line AB, (b) Evolution of pore pressure along the line AB . . . . .	113
V .12	Damage distribution in two composites with different sizes of inclusions (left: $3mm$ ,right: $2mm$ ) . . . . .	114



---

V .13	Inclusions distribution in the numerical concrete-like composites for $\rho_v = 35\%$ with different inclusion sizes $\phi = 1mm$ , (b) $\phi = 2mm$ , (c) $\phi = 3mm$ , (d) $\phi = 4mm$ , . . . . .	115
V .14	Crack patterns of model for $\rho_v = 35\%$ and (a) $\phi = 1mm$ , (b) $\phi = 2mm$ , (c) $\phi = 3mm$ , (d) $\phi = 4mm$ , . . . . .	116
V .15	(a) Crack length and (b) average crack width for different aggregates size .	117



# List of Tables

II .1 Parameters for different materials of inclusions . . . . .	32
II .2 Reconstructed images of representative cross-sections in different samples et different steps of drying (Li et al., 2020) . . . . .	35
II .3 Parameters for materials of inclusions and cement matrix (Li, 2016) . . . . .	37
IV .1 Gradation of coarse aggregates of studied concrete (Hirsch, 1962) . . . . .	81
IV .2 Mechanical properties of constituents (Wang et al., 2015) . . . . .	81
IV .3 Parameters for different materials of inclusions (Li et al., 2020) . . . . .	86
V .1 Material parameters used in the numerical simulate (Callari and Abati, 2009)	108
V .2 Material parameters used in the numerical simulations . . . . .	111



# General Introduction

As one of widely used construction material in the world, cement-based materials is used in various engineering applications: from civil construction to nuclear power plants. Once they are formed, they are generally submitted in an environment with lower relative humidity comparing with its initial fully saturated states. Drying shrinkage cracks formed by restraint to volume changes then caused by loss of excess water. These cracks effect not only the mechanical performance but also the transfer properties. Moreover, the transfer of harmful substances through the cracks may have also an important impact on the durability of construction. Therefore, the durability of cementitious materials and structures needs a good understanding of cracks of concrete structure to improve.

Concrete is essentially composed of cement, water, aggregates, possible additions and/or admixtures. The spatially random distribution of different constituents, having different characteristics, results in a heterogeneity character of concrete at the mesoscale level. According to the internal structural characteristics of cementitious material, the research works in the literature have been performed on three scales: macroscopic, mesoscopic, and microscopic ([Wittmann, 1983](#)).

In general, when the size of concrete is several times larger than the maximum volume of aggregates, cementitious material can be considered as a homogeneous material at the macroscale. Due to the limitations of research methods and experimental techniques, classical theories mostly focus on the mechanical properties and failure behavior. Even though the experimental observation and theoretical/numerical studies are representative and comprehensive ([Hua et al., 1995](#); [Jin et al., 2012](#); [Peron et al., 2009](#); [Sánchez et al., 2012](#)), the heterogeneous nature of material failure is not taken into account. Moreover, these macroscale results are indispensable for the validation of research works obtained at a low scale.

At the mesoscale, concrete is considered to as a composite material, which is composed of coarse aggregate, cement mortar and interfacial transition zones ([Bisshop and Van Mier, 2002a](#)). Due to the random distribution of different components, cement-based material exhibits important inhomogeneity characters. The influence of different phases and their interactions on the overall properties of concrete are studied and lately are used to predict the macroscopic behavior of material/structure. The bonding zones between cement mortar matrix and coarse aggregates are the weakest part of material and significantly affect the macroscopic response of material. In view of this, an accurate description

of properties/behavior of different phases, especially the interfacial properties, is an important issue for the construction of an realistic mesoscopic models. However, due to the weak thickness of interface, which are usually 9 to  $51\mu m$  (Garboczi and Bentz, 1991; Scrivener et al., 2004; Zheng et al., 2005), an accurate estimation of the properties of different phases becomes a major focus and challenge for mesoscopic studies.

At the microscale, the analysis is usually performed at the molecular and atomic level. In this domain, the crystal structure and molecular composition of cement hydrates can be studied experimentally with the aid of scanning electron microscopy. At this scale, cement paste, which is considered homogeneous at the mesoscopic scale, is not homogeneous because of the spatial distribution of hydrated and non-hydrated particles and various pores. Macroscopic properties such as strength, permeability, and durability of concrete are highly dependent on cement hydration. Even though the spatial structure of cement paste is currently well understood, it is still difficult to establish a specific and accurate correspondence between the micro-structure and macroscopic properties of concrete.

Due to the complexity of inter-structure and material composition, the process of dry shrinkage cracking exhibits obvious multi-scale characteristics: at the microscopic scale, the rupture of atomic bonding leads to tensile and slide failure; at the mesoscopic scale, potential defects in the internal structure lead to the initiation and propagation of micro-cracks that eventually penetrate into macroscopic cracks; at the macroscopic scale, unstable regions appear due to stress concentration, and crack propagation leads to instability failure. The failure modes of material at different scales can be related by the change of scales. In order to get a good estimation of macroscale behavior of cementitious material and improve the design of concrete materials and their corresponding structures, it is necessary to study the non-uniformity of mesoscale structure of cementitious material and develop numerical models to study the material damage.

The shrinkage of concrete and cementitious materials is an important issue in the durability study of cementitious material. In general, the shrinkage can be divided into two parts: autogenous shrinkage caused by the cement itself and drying shrinkage induced by water loss (Neto et al., 2008). The level of drying shrinkage is related to the relative humidity of external environment ,the composition of cementitious materials, and the type and proportion of aggregates (Barcelo et al., 2005), etc... As the stiffness of aggregates is generally two or three times bigger than that of cement paste, the shrinkage of cement paste is constrained by the aggregates. This restraining effect is greatly influenced by the characteristics of the aggregates, for instance the type and size content of the aggregate (Bissonnette et al., 1999; Fathifazl et al., 2011). In view of this, this thesis focuses on the

roles of aggregates in the drying shrinkage cracks of concrete. The emphasis is put on the influence of rigidity and size of inclusions on drying shrinkage cracking. Therefore, the contentious composites with different inclusions are made and used for the experimental investigation and numerical simulation.

For the experimental investigation, different types of techniques have been developed to visualize the evolution of micro-structures, such as acoustic emission measurements (Shiotani et al., 2003), infrared thermography, impregnated fluorescence microscopy, and environmental scanning electron microscopy (Bisschop and Van Mier, 2002b) etc... Each method has its advantages and disadvantages (Alam et al., 2014), and some even being destructive and leading to secondary micro-cracking. With the development of imaging and computer processing techniques, X-ray computed tomography (XCMT) has become a very powerful non-destructive monitoring technique. This technique provides high-resolution images to capture the evolution of micro-structure and can be easily combined with in-situ mechanical testing. It has been widely used for micro-structural identification of cementitious materials (Gallucci et al., 2007; Landis and Nagy, 2000; Lu et al., 2006), experimental characterization of induced micro-cracks under different loading conditions (Elaqra et al., 2007; Lu et al., 2006), micro-structural degradation during chemical leaching (Burlion et al., 2006; Rougelot et al., 2010), drying cracking (Szczesniak et al., 2013), etc... XCMT imaging can provide 3D full-field visualization and abundant information on the micro-structure of material, such as crack shape, size and distribution. This approach provides us new possibilities for understanding the mechanisms of fracture and damage in cementitious material. In this study, the XCMT technique will be used to characterize the drying shrinkage cracks that develop in concrete composites with different types of inclusions.

Numerical simulations are able to study the cracks of cementitious material under different loading conditions. During recent decades, some numerical methods have been developed for modelling the nucleation and propagation of cracks in solid materials. Without giving an exhaustive list of all those methods, we only mention here three methods: the extended finite element method (XFEM) by using a nodal enrichment technique to describe crack displacement discontinuities (Moës et al., 1999), the mesh-less methods (Rao and Rahman, 2000) by using high-order continuous approximation functions and the discrete element methods (DEM) with considering cracking as interface debonding (Onate and Rojek, 2004). However, they are not efficient for the description of multiple cracks created in heterogeneous concrete composites. Therefore, Peridynamics theory (PD) (Silling, 2000) will be adopted in the present study for the description of drying shrinkage cracks.

In the PD theory, integral motion (or static equilibrium) equations are solved instead of the partial derivative ones, which are usually used in classical continuum mechanics. Therefore, numerical methods based on the PD theory are particularly suitable to deal with multiple discontinuity problems. Additionally, in PD theory, as the cracking process is directly related to the progressive breakage of internal material bonds, it is very efficient to describe the nucleation and propagation of multiple cracks even with the consideration of the intersections between them (Li and Guo, 2018). Therefore, the PD theory will be used to study the progressive cracking and failure of cement based materials in this thesis.

The objective of our study is to analyze the characteristics and micro-structural evolution of cementitious materials during drying via a series of experimental tests and numerical simulations. Therefore, this thesis is composed of six chapters:

**Chapter I** reviews the mechanism of the drying shrinkage induced cracks in cementitious materials, as well as some of the influence factors based on previous experimental research, outlines several constitutive models commonly used to describe the mechanical behavior for concrete with cracks, and summarizes the advantages and disadvantages of modelling methods based on local theory. Finally, the development and current status of the non-local based method peridynamics (PD) is introduced.

**Chapter II** briefly summarizes the experimental results of Li et al. (Li et al., 2020) on the effects of aggregate stiffness on the shrinkage cracking of cementitious materials. The influence of aggregate size on drying shrinkage cracking is then presented, and the crack morphology is analyzed with the help of XCMT technique.

**Chapter III** briefly describes one of the most widely used theories of peridynamics, the bond-based PD theory, and derives the basic parameters of peridynamics from the elastic potential energy density of PD and the strain energy density of classical continuum mechanics theory, and evaluates the effects of some adopted numerical parameters: horizon particle density, grid size, and horizon size on the computational results.

**Chapter IV** develops a mesoscale heterogeneous concrete damage model. The proposed model is firstly validated by simulating the tensile failure process of the specimens with a random aggregates distribution. Based on the experiments presented in **Chapter II**, the effects of aggregate stiffness on drying cracking are studied via a mesoscale model. The experimental observation and numerical results are compared and discussed.

**Chapter V** proposes a fully coupled peridynamic hydro-mechanics models for saturated and partially saturated porous cementitious materials. Two cases of the drying tests in **Chapter II** are simulated by the proposed model. And the results are compared with the experimental data. Then, several numerical samples with the same aggregate volume



fraction are established to study the influence of aggregate size on the mechanical behavior of the studied material.

**Chapter VI** presents the conclusions and perspectives.



# Chapter I

## State of the Art

### 1 Introduction

Due to its numerous advantages (such as easy to use, low cost and high compression strength, etc...), cementitious material becomes the most widely used building material in the world. However, cementitious materials have a very poor crack resistance. After casting, they are exposed to a lower relative humidity environment than the initial one in its own pore system (Yang et al., 2019). Consequently, they dry and shrink due to water loss, accompanied the occurrence of shrinkage cracks. Shrinkage cracks have an impact on the impermeability and carrying capacity of building: increase in deformation, decrease of mechanical resistance and increase of permeability etc... Therefore, shrinkage cracks of cement based material become one important issue in the framework of durability study of cementitious materials/structures.

This chapter will firstly introduce a synthesis of experimental observation methods for the visualization of the micro-structure of cementitious materials. Then the mechanism of the drying shrinkage cracks in cementitious materials will be discussed. After that, several constitutive models proposed for the description of the mechanical behavior of cracked concrete are presented and discussed based on local theory. Finally, the development and current status of the non-local based method Peridynamics will be presented.

## 2 Experimental observations of micro or meso-structure of cementitious materials

### 2.1 Experimental observation methods

In order to visualize the evolution of micro-structure of cementitious materials, different types of techniques have been developed, for instance, acoustic emission measurement (Ohno and Ohtsu, 2010; Shiotani et al., 2003), infrared thermography (Cheng et al., 2008), impregnating fluorescence microscopy (FEIM) and environmental scanning electron microscope (ESEM) (Bisschop and Van Mier, 2002b). These techniques are capable of studying the micro-structure of cement-based materials. Each technique has its advantages and short comings.

The acoustic emission (AE) is a technique to monitor defect formation and failures in structural materials. It is very suitable to capture the apparition of crack in cement based materials. However, for the detection of micro-structures and micro-cracks, the combination with other techniques is needed for AE technique (Alam et al., 2014). Therefore, the AE signals are largely used to study the initiation and propagation of cracks in cement-based material (Fig. I .1).

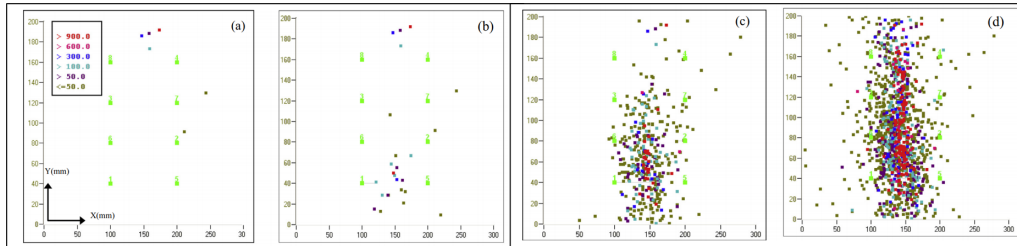


**Figure I .1:** Localization maps of the AE events from the beginning (0%) to the given loading stage in D2 beam as function of absolute acoustic energy (aJ) (Alam et al., 2014)

The infrared thermography (IRT) is an effective tool for getting a fast and qualitative acquisition of structural conditions. However, according to the depth of hidden defects in concrete, IRT can provide only some limited quantitative information. As a result, IRT is more suitable for rapid diagnostic of large-scale engineering structures (Cheng et al., 2008) (see Fig. I .2) and can be used to combine with other imaging techniques (Ghorbel et al., 2011).

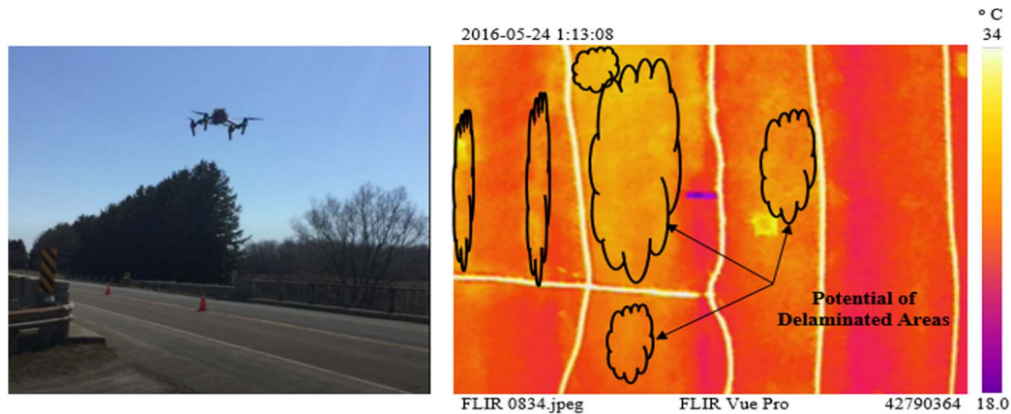


**Figure I .2:** Snapshot of the UAV during the flight to scan bridge and a captured thermal image indicating potential delaminated areas (Omar and Nehdi, 2017)

The environmental scanning electron microscope can be also used to identify and quantify the micro-crack patterns. In this method, the high contrast images can be obtained with a fluorescent epoxy impregnation (Fig. I .3) and then facilitate the quantitative analysis procedure (Malek et al., 2017). However, this technique is generally use in surface areas and is more suitable for the small-scale observation of fine micro-structure, such as morphology and mineral compositions (Knab et al., 1984).

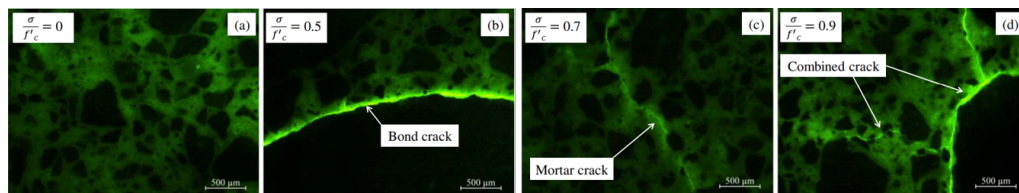


**Figure I .3:** Micrographs of thin petrographic section illustrating micro-crack maps at four stress levels (Malek et al., 2017)

In addition, some of previous mentioned techniques are destructive and induce some new micro-cracks (Bisschop and Van Mier, 2002b). With the development of imaging technology and computer processing, the X-ray computed micro-tomography (XCMT) becomes a very powerful non-destructive monitoring technique. This technique is able to provide high-resolution images to capture the evolution of micro-structure of nonstructural materials and can be easily combined with in-situ mechanical tests. Moreover, the XCMT imaging technique can provide 3D full-field visualization of the material micro-structure, such as crack shape, size and distribution. It has been widely used on the cement-based materials, for instance the identification of micro-structure (Gallucci et al., 2007; Landis

and Nagy, 2000; Lu et al., 2006), the characterization of induced micro-cracks under different loading conditions (Elaqra et al., 2007; Lu et al., 2006), the micro-structural degradation during chemical leaching (Burlion et al., 2006; Rougelot et al., 2010), and the drying cracking (Szczesniak et al., 2013), etc... As shown in Fig. I .4 and I .5, the XCMT technique shows clearly the complicated 3D composites and fracture paths in concrete.

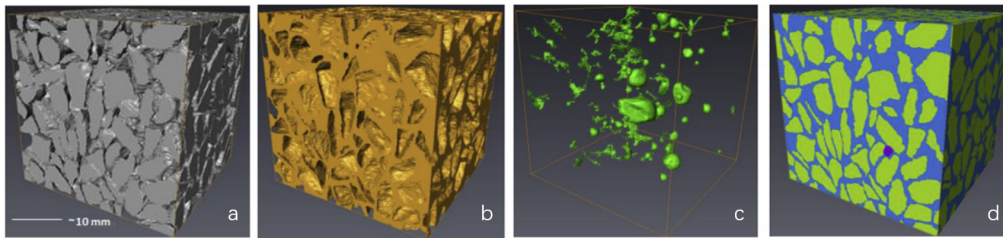


**Figure I .4:** 3D Segmented phases without load: (a) Aggregate; (b) Mortar; (c) Voids and pores; (d) Combined concrete (Yang et al., 2017)

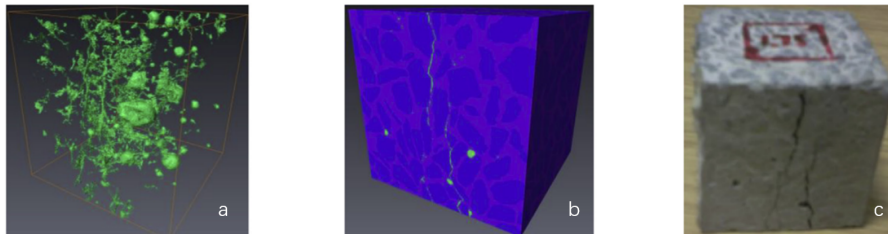


**Figure I .5:** 3D segmented phases after load: (a) voids and cracks; (b) Combined concrete; (c) Failed specimen at peak load (Yang et al., 2017)

## 2.2 Structural composition of cementitious materials

Based on experimental observations at the meso-scale, as shown in Fig. I .6, cementitious materials can be considered as a three-phase material that consists of hard aggregates with a surrounding weak zone called interfacial transition zone (ITZ) embedded in a cement mixture paste (i.e mortar).

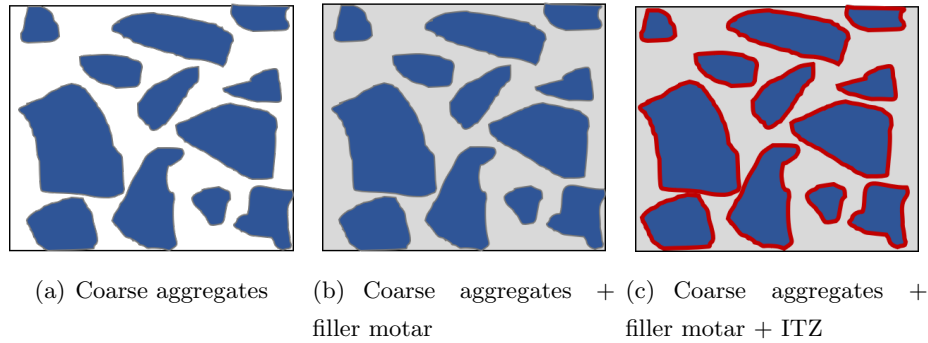


**Figure I .6:** Schematic diagram of meso-structure of cementitious materials

Mortar in cementitious materials can be artificially divided into two categories, one is the filler mortar used to fill the voids where the hard aggregate particles accumulate. Its shrinkage and deformation mainly comes from the free shrinkage. The other one is the wrapping mortar which wraps the coarse aggregate with a certain thickness. This part of mortar plays the role of isolating the coarse aggregate lap, and its shrinkage and deformation is constrained by hard aggregate. The shrinkage and deformation of cementitious materials is related to the average thickness of cement paste wrapping the coarse aggregate, which is generally 9 to  $51\mu m$  (Garboczi and Bentz, 1991; Scrivener et al., 2004; Zheng et al., 2005).

### 2.3 Mechanism of drying shrinkage cracking

Drying shrinkage in cementitious materials may induce additional stresses and cracking when the drying shrinkage is restrained. The amplitude of restraint depends on the degree of shrinkage, internal structure of studied material and mechanical properties of different components. In general, two types of restraint can be identified: external restraint imposed onto the surface of a shrinking sample/structure and internal restraints. According to the internal restraint, two types are generally observed in cementitious material. The first one is related to the moisture gradient developing in the cement paste. Due to low permeability of cementitious material, the drying front penetrates progressively in the material. A shrinkage gradient is observed and then create stresses and cracking in cementitious material (Fig.I .7). The second internal restraint is related to the presence of aggregate which restrains matrix shrinkage. The degree of aggregate restraint can be so important that induces the cracks. Fig.I .8 illustrates the generation of radial and circumferential cracks in concrete samples after drying. This thesis focus on the internal restraint.

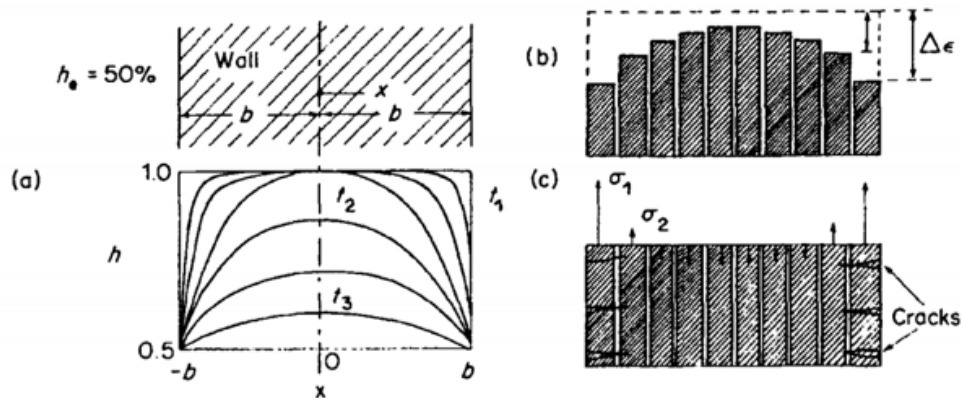


**Figure I .7:** Concrete wall exposed to drying: (a) Distribution of relative humidity at different drying times; (b) Inhomogeneous distribution of shrinkage strain; (c) Induced stress and cracking due to restoration of compatibility conditions (Bazant, 1988).

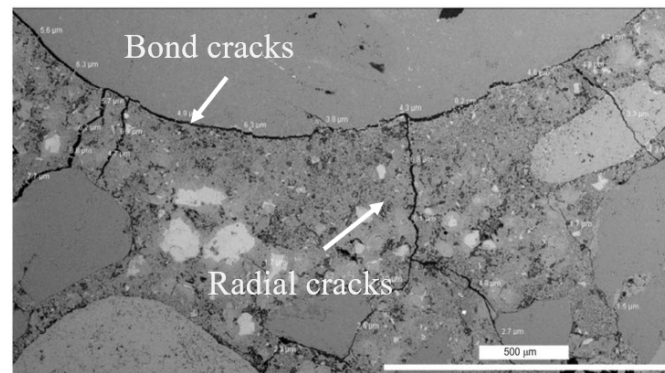


**Figure I .8:** Microcracks observed in drying sample (Wong et al., 2009).

Based on the stress distribution, Goltermann (Goltermann, 1995) has studied the crack patterns around a hard aggregate particle embedded in a shrinkage cement matrix. During drying, aggregate particle will be in hydro-static compression due the shrinking matrix. Inversely, coarse aggregate exerts a reaction force (radial stress) on mortar. The cement matrix is then in compression in radial direction and in tension in tangential direction. The stress magnitude is a function of the distance between the studied matrix point and the aggregate, but is independent of the aggregate size. The most important tensile stress are observed at the boundary of aggregate, where cracks will be created when the stresses exceed the tensile strength of the cement matrix. Furthermore, the cracks radiate out from the edges of the aggregate particles. The width of total radial crack depends on the aggregate particle size. When cracks occur, shear stresses develop along the interface and



may create the banding cracks. Their amplitude depends on the band strength, which is related to the band conditions. Very limit or even zero band cracking is possible in the case of a good band. This phenomenon is due to the fact that radial compression is transferred across the band crack.

## **2.4 Contribution of various factors in drying shrinkage cracks**

During drying, when the restraining stress is greater than the tensile strength of cementitious material, cracks occur and develop. Recently, for concrete with a water-cement ratio of normal range, it is generally accepted that the performance and amount of aggregates are the main issue controlling the shrinkage cracks. Therefore, their influence on drying cracks has been studied by several researchers, such as the effects of aggregate stiffness, volume fraction, size, and contact surface condition, etc... The most important ones are presented in this section to better understand the basic mechanisms leading to microcracking.

### **2.4.1 Effects of aggregate shape**

Shape regularity of aggregates is one of the important issues that alter the concrete quality. It may induce an anisotropic restriction around inclusions and then induces a stress concentration at angular points. In practice, for reason of simplicity, the spherical (3D) or circular (2D) inclusions are largely used in experimental investigation and numerical simulation to study the shrinkage cracks in concrete. For instance, Hsu ([Hsu et al., 1963](#)) used a square array of sandstone discs as aggregates to identify the typical cracking patterns in cementitious materials. Bond cracks between the cement paste and aggregates, as well as radial cracks between the aggregates, were created by the tensile stress related to the drying shrinkage (Fig.I .9). The similar results were also observed by other researchers ([Creath et al., 1969](#); [Dela and Stang, 2000](#); [Hearn, 1999](#)).

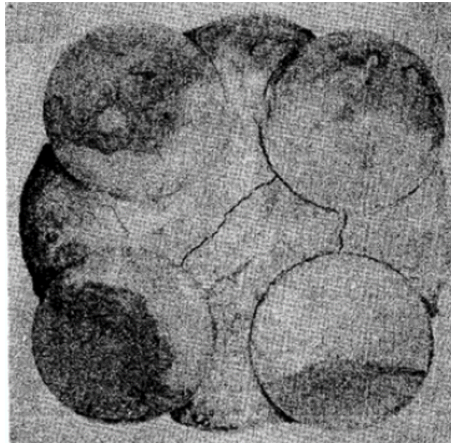


**Figure I .9:** Crack patterns observed in shrinkage tests(Hsu et al., 1963).

According to the numerical simulation, Wittmann (Wittmann et al., 1985; Wittmann, 1983) firstly used randomly distributed polygons to represent the aggregates and construct a mesoscale model of concrete (Fig.I .10), which has been largely used by different researchers since then.

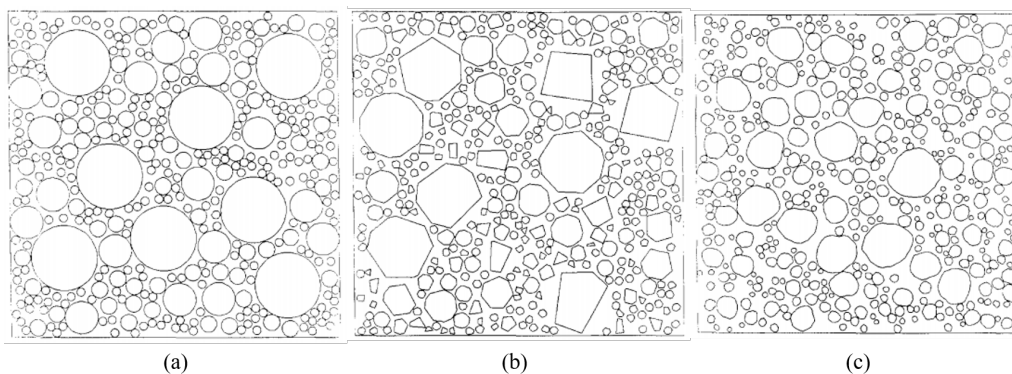


**Figure I .10:** Two-dimensional structure with a given size distribution of the aggregates: (a) spherical geometry; (b) polygons geometry; (c) given morphological law (Wittmann et al., 1985).

#### 2.4.2 Effects of the aggregate volume fraction

In 1969, Mc Creath (Creath et al., 1969) have confirmed the typical cracking patterns observed by Hsu (Hsu et al., 1963) and exhibited that the induced shrinkage cracks were more obvious in the concrete containing higher volume fraction of aggregates. After that, Bisschop et al. (Bisschop and Van Mier, 2002a) confirmed that the degree of constraining effects of aggregates on the shrinkage cracking increases with the volume fraction of

aggregates. They have studied cementitious composites with different sizes of beads and obtained the following conclusions: In the composites with small beads ( $0.5\text{mm}$  and  $2\text{mm}$ ), the increase of bead quantity induces a decrease of crack length; On the other hand, in the composites with big beads ( $2\text{mm}$ ,  $4\text{mm}$ , and  $6\text{mm}$ ), the cracks length increases with the bead quantity (Fig. I .11). In addition, the maximum depth of cracks observed in the composites depends also on the bead quantity: with  $0.5\text{mm}$ ,  $1\text{mm}$  and  $2\text{mm}$  beads, it decrease with increasing of bead quantity while in the composites with  $4\text{mm}$  and  $6\text{mm}$  beads, it increased with the bead quantity (Fig. I .12).

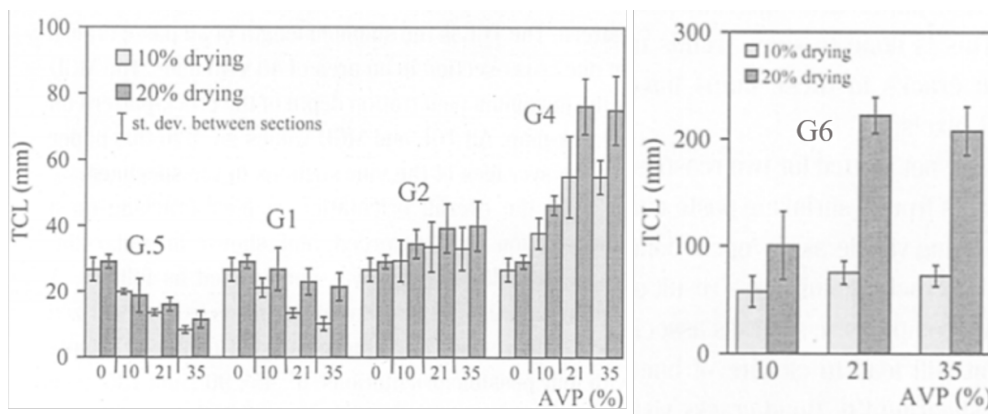


**Figure I .11:** Total length of drying shrinkage microcracking (TCL) in studied cement composites and cement paste (AVP:aggregate volume percentage, G.5:  $2\text{mm}$ , G1:  $1\text{mm}$ , G2:  $2\text{mm}$ , G4:  $4\text{mm}$ , G6:  $6\text{mm}$ ) (Bisschop and Van Mier, 2002a)

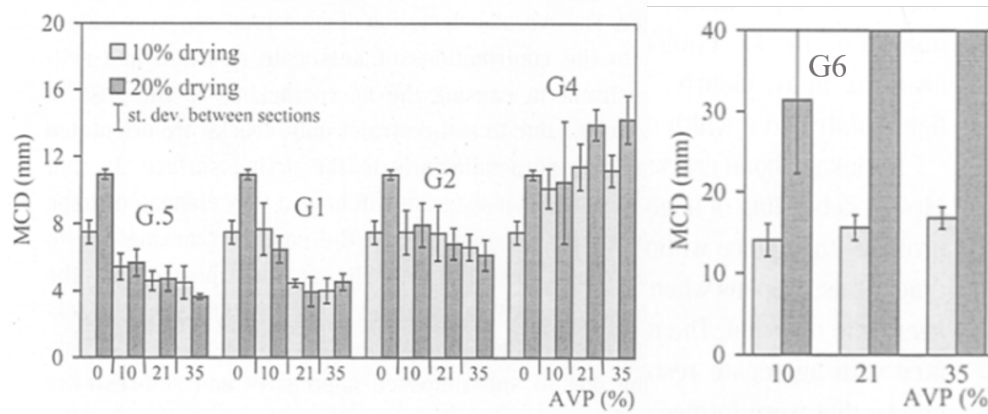


**Figure I .12:** Maximum depth of drying shrinkage microcracking (MCD) in cementitious composites and cement paste (Bisschop and Van Mier, 2002a)

Grassl et al. (Grassl et al., 2010) investigated the effects of volume fraction of aggregate

on dry cracking by using a lattice model. The obtained results show that an increase of aggregate volume fraction induces an decrease of average crack width and an increase of crack length (Fig. I .13).

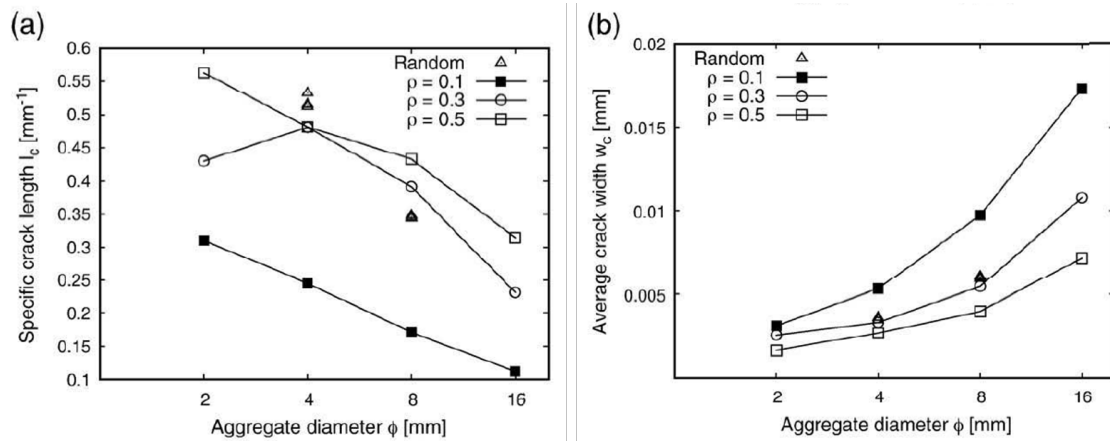


**Figure I .13:** (a) Specific crack length and (b) average crack width versus aggregate diameter  $\phi$  (Grassl et al., 2010)

### 2.4.3 Effect of the aggregate size

In the literature, several researchers (Bisschop et al., 2001; Bisschop and Van Mier, 2002a) have shown that the shrinkage cracking also depends on the aggregate size: the effect of aggregate constraint on shrinkage and the shrinkage cracking increases with increasing of aggregate size while the resistance of studied cementitious composites decreases with increasing of aggregate size. In Fig. I .11 and Fig. I .12, we can observe that the total length and the maximum depth of crack increased with increasing aggregates size. In Fig. I .14 the crack-maps and radar-diagrams are given for all composites containing 35% glass aggregates. It can be seen that the orientation of cracking became more isotropic in composites with larger aggregates.

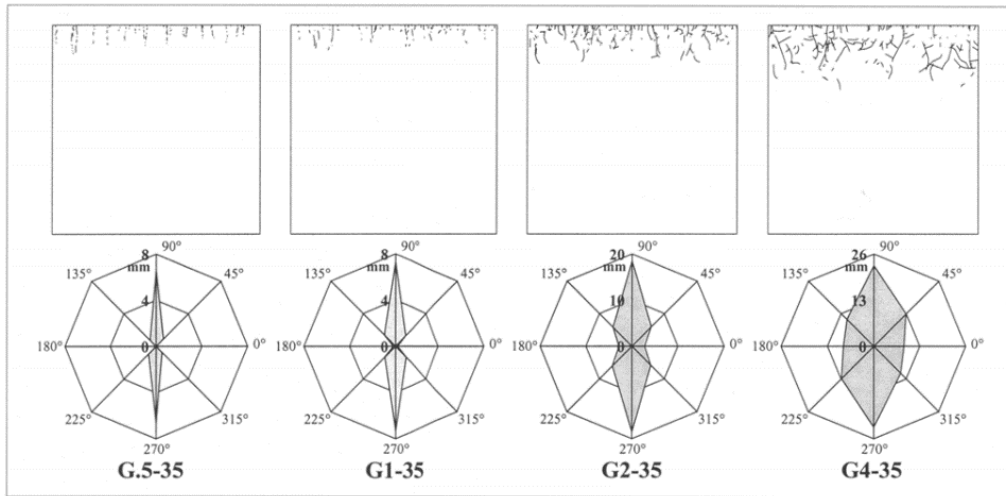


**Figure I .14:** Effect of aggregate size on induced drying shrinkage microcracking in the composites with 35% aggregates. Upper row: maps of drying shrinkage microcrack; Lower row: orientations of microcracking (Bisschop and Van Mier, 2002a)

Grassl et al. (Grassl et al., 2010) (Fig. I .13) have also found that when the diameter of the aggregate becomes larger, the microcracking length decreases and the average width of cracks increases. Idiart et al. (Idiart et al., 2012) have also confirmed that the density of drying cracks increased with increasing aggregate size and volume fraction via a series of numerical simulations and experimental tests.

#### 2.4.4 Effect of the aggregate stiffness

By using the XCMT technique, the effects of aggregate stiffness on drying cracks were studied (Li et al., 2020). The obtained experimental results confirm the important influence of aggregate stiffness on the number of drying cracks: radial cracks are induced and driven by tensile circumferential stresses while the cement paste shrinkage is constrained by the stiffer aggregate. Due to the strong interaction between the aggregates, cracks are also observed in the cement paste between the aggregates. The drying shrinkage cracks increase with the elastic stiffness of aggregates. More specifically, to demonstrate more clearly the effect of inclusion stiffness on drying cracks, the cumulative length and width of the cracks were measured. By comparing the crack lengths in two cases with different types of inclusion, it was tentatively concluded that the crack length increases with the stiffness of the inclusion (Fig. I .15(a)). The crack width, on the other hand, ranges between 3 and 30 pixels, with a particular concentration at 5-6 pixels (Fig. I .15(b)).

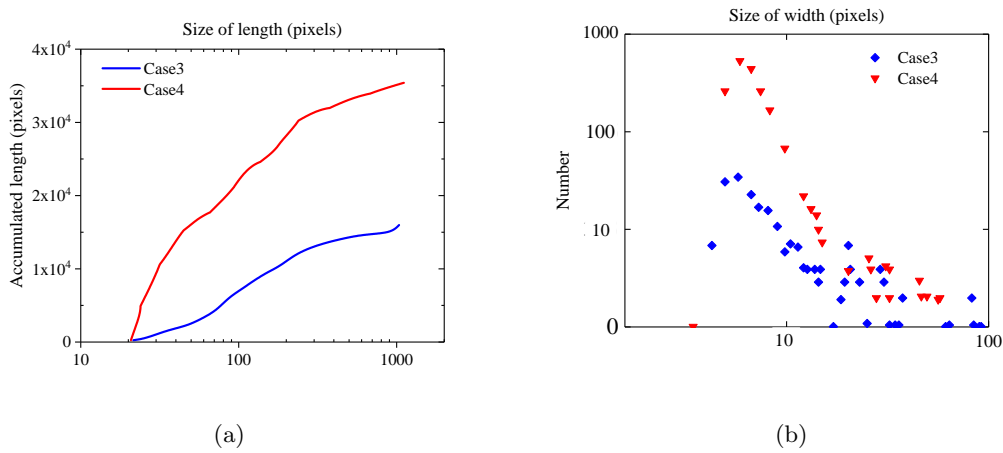


**Figure I .15:** (a)Accumulated length and (b) measured width of cracks in different samples

Based on previous studies, we can conclude that the characteristics of aggregates play an important role in the study of the drying shrinkage cracks of cementitious materials. However, due to the complexity of studied materials and the difficulty in experimental analysis and numerical simulations, the effect of aggregate on drying shrinkage cracking is still under-researched and further research is necessary. Therefore, inspired by Li's research (Li et al., 2020), the present thesis will focus on the effects of aggregate size and stiffness on the shrinkage cracks by using advanced experimental techniques and progressive numerical simulation methods.

### 3 Description of mechanical behavior for cracked concrete

#### 3.1 Fracture mechanics

Since the 1960s, numerous numerical researches have been performed on the fracture and damage of concrete structures. The classical fracture mechanics is formulated on the basis of metal material study. Neville (Neville, 1959), who firstly applies the theory of Griffith (Griffith, 1921) on cementitious materials, proposed that the effect of concrete sample's size on its strength is related to the randomly distributed cracks in concrete. In 1961, the fracture mechanics has been introduced into the study of concrete fracture (Kaplan, 1961). During the early period, most of these research works are based on linear elastic fracture mechanics: the concrete structure is considered as linear elastic body before the onset of cracks; After that, the structure is composed with fractures and linear

elastic materials. With the linear elastic hypothesis, strength factor method and energy method are used to analyse the concrete fracture. However, when the concrete is assumed as a linear elastic material, the heterogeneity of concrete is ignored. A few years after, Kesler (Kesler et al., 1972) pointed that the onset and propagation of fractures in concrete depended on its complex internal structure. Numerous experimental results exhibit that in concrete under loading, some wing cracks and micro-cracks occur around the main cracks and induce non-linear mechanical behavior of concrete. The application of linear elastic fracture mechanics in the analysis of concrete rupture is not capable of taking into account the slow crack propagation (sub-critical crack propagation) and micro-cracks. As a result, the measured fracture toughness exhibits an important size effect. The broken of concrete is generally characterized as brittleness. Specifically, the plastic zone around the crack tip is very small comparing with the fissure zone, where sub-critical crack propagation is dominant. It should be noticed that the mechanism of sub-critical crack propagation zone is different from the plastic zone of metal materials. Therefore, it is also unsuitable to apply the elastic-plastic fracture mechanics into the rupture of concrete: J-integral theory (Rice, 1968) and crack tip opening displacement theory (Wells, 1961). In the literature, numbers of macroscopic fracture models have been proposed to predict the non-linear fracture process of concrete, for instance, the discrete crack model (Ngo and Scordelis, 1967) and the smeared crack model (Rashid, 1968).

### 3.1.1 Discrete crack model

To model the onset and propagation of concrete cracks, Ngo and Scordelis (Ngo and Scordelis, 1967) introduced finite element discrete crack model to study a reinforced concrete beam with pre-cracks. However, in finite element discrete crack model, the propagation of cracks has been restricted at the boundary of elements (as shown in Fig. 1.16.c), and the nodes need to be renumbered in the calculation. Consequently, it is difficult to get the right propagation path and it makes the calculate process very complex. For this reason, an adaptive refinement finite element method (Bauska, 1986) was introduced by using the adaptive mesh and linear elastic fracture mechanics. It has been successfully applied in plane fracture problems, having few crack propagation. But it can not deal with three-dimensional problems or be used in the problems with dense crack density. In order to overcome the difficulties of re-meshing, another way to improve the finite element discrete crack model is to introduce the interface elements. However, this method could not predict correctly the cracking path. Therefore, the discrete crack model is not widely used in engineering applications.

### 3.1.2 Smearred crack model

Based on the variational principles of the finite element method, Rashid (Rashid, 1968) proposed a smeared crack model. As the calculations are performed independently at each integration point of the finite element model, this method do not need pre-cracking or re-meshing (as shown in Fig. I .16.d). Therefore, it has been used widely in the numerical analysis of concrete structures, for example the commercial software ANASYS and ABAQUS include this model. Inversely, as this method could not describe the real shape of the cracks, different failure modes can not be described.

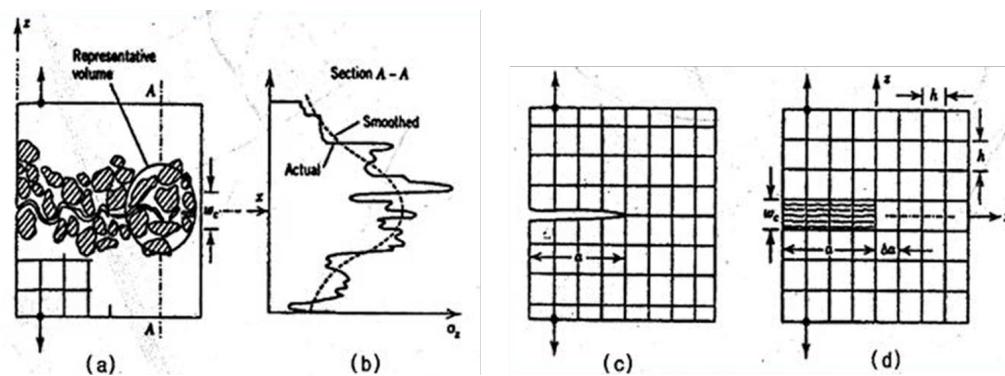


**Figure I .16:** Illustration of the hypothesis of the discrete and smeared crack model:(a) Micro-structure; (b) Stress distribution and crack boundary; (c) Discrete crack model; (d) Smeared crack model (Rashid, 1968)

Based on the previous two models, many crack models have been developed for concrete, such as fictitious crack model (Hillerborg et al., 1976), cohesive slit model (Dugdale, 1960), crack band theory (Bazant and Oh, 1983) and etc... All these models are based on the energy criterion, in which the consumed energy for generating unit length crack is certain. In these models, the problem of numerical instability is often observed by the superposition of positive and negative stiffness of softening and hardening regimes. In order to solve this problem, some non-local models (Bazant, 1984; Bazant et al., 1984), based on the concept of average strain in space, have been proposed. The non-local model can avoid the mesh sensitive problems and has been widely used in many applications. The numerical method used in the present study is based on non-local method.

## 3.2 Damage mechanics

The damage mechanics was firstly applied to the concrete materials by Dougill (Dougill, 1976). Two kinds of research methods are generally used: macroscopic method and mi-



croscopic method. In the macroscopic models, damage is described by the introduction of state variables, such as Loland model (Loland, 1980), Mazars model (Mazars, 1984), Sidoroff model (Sidoroff and Dogui, 2001) and Krajcinovic model (Krajcinovic and Fonseka, 1981). On the other hand, in microscopic method, the damage variable is formed by considering the micro-structure of materials, for instance, the microplane model proposed by Bazant (Bazant and Oh, 1985). The basic idea of these models is that the normal stress on the microplane is a function of normal strain on the same microplane. This strain is further assumed to be equal to the resolved component of the macroscopic strain tensor, while the stress on the microplane is not equal to the resolved component of the macroscopic stress tensor. The normal strain on a microplane may be interpreted as the sum of the elastic strain and of the opening widths (per unit length) of all micro-cracks in the same direction of microplane. The normal strain or shear strain on the microplane could be used as the state variables of damage. Therefore, the relationship between the damage and crack propagation path can be established in concrete. But it is difficult and complex to superimpose the strain and stress of all microplanes.

As the fracture mechanics focuses on the initiation and propagation of the localized cracks, it could not take into account the influence of micro-cracks on the mechanical behavior of studied material. On the other hand, the damage mechanics could recompense this deficiency of fracture mechanics. As a result, it is interesting to combine the fracture mechanics and damage mechanics to study the rupture mechanism of concrete structures.

### 3.3 Meso and micro-scale model

Concrete and cementitious materials are inherently multiscale materials: micro, meso and macro structures, as shown in Fig.I .17. The three scales method is firstly applied on concrete materials by Wittmann (Wittmann, 1983). At the macroscale, concrete is considered as a homogeneous material without the consideration of the internal structure. At a lower level of observation, called mesoscale, concrete can be considered as a three-phase cementitious material that consists of coarse aggregates with a surrounding weak zone called interfacial transition zone (ITZ) embedded in a cement paste. At this scale, aggregate particles and larger voids can be observed. The interaction between aggregate particles and mortar matrix is then a key factor for the study of concrete. When going down again one scale, called microscale, the cement paste is more detailed and composed of unhydrated cement particles, hydration products and capillary pores.

On the macroscopic scale, as the internal structure of concrete is ignored, cementitious material can be assumed as a uniform and isotropic material. The obtained results can be

easily used in the engineering application. Therefore, based on experiment investigation obtained at the macroscopic research scale, numerous theoretic/numerical research have been performed on concrete by using fracture mechanics and damage mechanics. Moreover, a series of mechanical models have been proposed to study the complex mechanical characteristics of fracture process. However, the realized research works on this scale cannot reveal the relationship between the internal structure/composition and the macroscopic behavior/properties of concrete. Therefore, the research at lower scales become a very interesting topic in solid mechanics.

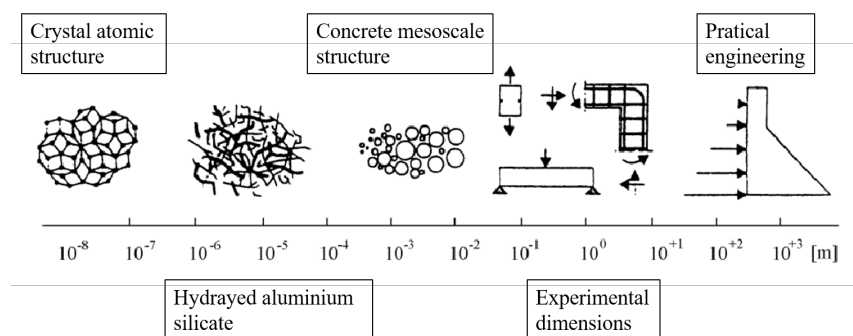


**Figure I .17:** Research scale of concrete materials ([Wittmann, 1983](#))

At the microscale, the more widely used microscopic concrete models are lattice models ([Chiaia et al., 1997](#); [Schlangen and Garboczi, 1997](#); [Van Mier, 1996](#)), micro-mechanical models ([Mohamed and Hansen, 1999](#)) and particle models ([Bazant et al., 1990](#); [Cundall and Hart, 1993](#)).

### 3.3.1 Lattice model

In order to simulate the gradual destruction process of concrete, Schlangen and Van Mier ([Chiaia et al., 1997](#); [Schlangen and Garboczi, 1997](#); [Van Mier, 1996](#)) introduced the lattice model, in which the studied material is a lattice system formed by connecting elastic bands and beam units, as shown in Fig. I .18. In spite of that, the element deformation and the unloading residual strength of structure can not be estimated by this method.

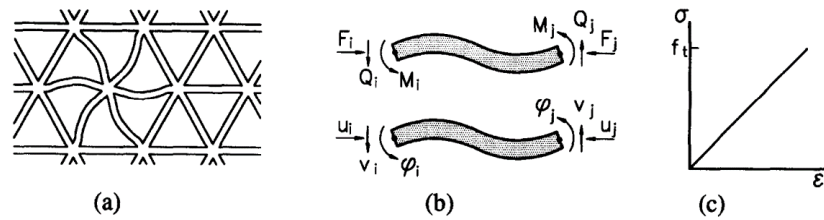


**Figure I .18:** (a) Regular triangular lattice of beams; (b) External forces and deformations on a single beam element; (c) Stress-strain relation for an element. (Schlangen and Garboczi, 1997)

### 3.3.2 Micro-mechanical model

Mohamed (Mohamed and Hansen, 1999) considered the concrete as a composite of three phases. The random distribution of material properties was considered by generating a random distribution of aggregate. The established concrete model has a complete meso-structures. As only a tensile failure is used in this model, it is particularly advantageous in the problems dominated by tensile failure. But it can not be used to study the concrete failure under complex stress states.

### 3.3.3 Particle model

In 1971, the particle model (Cundall and Hart, 1993) has been proposed to predict the mechanical behavior of particulate composite material. As the aggregate has been assumed as a round rigid elastic particle, this type of particle is more suitable to study the granular materials. Thereafter, many models have been developed based on the particle model, such as discrete element method (DEM) (Cundall and Strack, 1979) and Random particle model (Bazant et al., 1990). Most of these models adopt one hypothesis: the damage is induced by tensile stress. As a result, the tensile strength is a key parameter for these models. Moreover, these models require a great number of parameters: not only the geometric and mechanical parameters of the aggregate particles, but also the cohesion and friction angle of studied material. As the available experimental data is limited, it is difficult to find reasonable parameters for the numerical simulation and ensure the accuracy of the simulation results.

The research work performed at the macroscale is capable of predicting the damage and failure of concrete structures. However, it could not take into account the internal structure and components of material. To sum up, it is necessary to establish a bridge between the macro- and micro-scale numerical mode for concrete structures, which could

study the onset and propagation of micro-cracks, the formation of localized cracks and the failure mode of structure. The multi-scale model has a significant contribute to a comprehensive and scientific understanding of concrete fracture mechanism as well as the further improvement of concrete structure design (Malbois, 2019).

## 4 Overview of modeling methods for concrete materials

### 4.1 Local methods and their limitations

Since last century, numerous numerical methods have been proposed to simulate the non-linear mechanical behavior of concrete. The classical finite element method, which has been widely used in solid mechanics and engineering problems, has great advantages in simulating the structures with complex geometry boundaries and multi materials. However, the governing equations of finite element method are based on classical continuum mechanics. For this reason, they are difficult to solve the cracking problems or the discontinue deformations along the crack surface. To solve the numerical singularity of the crack tips, a special element is introduced into the classical finite element method. Meanwhile, when the crack extends, it should be re-meshed to predict the onset and propagation path of cracks. Therefore, it is almost impossible to use the classical finite element method to solve the problems with complex boundary conditions or multi cracks.

To overcome the drawback of the classical finite element method in solving the discontinue deformation problems, numbers of methods have been developed, for instance, discrete element method (DEM) (Cundall and Strack, 1979), meshfree methods (Liu and Gu, 2005) and extend finite element method (XFEM) (Moës et al., 1999).

The discrete element method (DEM), originally developed by Cundall (Cundall and Strack, 1979) for rock materials, is a family of numerical methods for computing the motion of a large number of particles, for instance molecules or grains of sand. This method is based on Newton's second law to determine the force, acceleration, velocity and displacement of all particles in the materials. The DEM is capable of simulating this type of non-linear large deformation character very well by using a discontinuous discrete medium. Thanks to its advantages in discontinuity simulation, the DEM has been widely used in study of slope, landslides and seepage problems. However, there is few examples of DEM can be found in the analysis of concrete structures.

Belytschko (Belytschko et al., 1994) developed the Element-free methods (EGM) based on the DEM to analyze the propagation of cracks in rock-like materials. EGM is more precise than DEM in the problems with crack growth, crystal growth and large deformation.

The Element-free method depends on the meshing and can solve the problems with higher efficiency and precision, for instance, mesh distortion problems. However, by using the continuous arbitrary higher-order functions in this method, the crosses of discontinuous interface cost too much computational resource. As a fracture criteria is necessary for the crack initiation, EGM cannot resolve satisfactorily the problems of multi cracks or crack branching .

In order to overcome these difficulties, the extended finite element method (XFEM) has been developed (Belytschko and Black, 1999; Moës et al., 1999). In this method, the discontinuous enrichment functions are added in the finite element approximation to describe a discontinuous displacement field. The crack is considered as a completely separate geometric entity and interacts with the mesh in the selection of the enriched nodes and the quadrature of the weak form. However, for severely curved cracks, some re-meshing near the crack root may be necessary. As re-meshing near the crack root is much easier than re-meshing at the crack tip (it may only need to be done in a few steps of a crack growth simulation), the method requires a minimal re-meshing. Therefore, XFEM can be applied in the various problems (Sukumar and Prévost, 2003) involving singularities, material interfaces and regular meshing of micro-structural features etc... However, due to the introduction of discontinuous expansion displacement, additional fracture criteria need to be introduced to predict the propagation of fracture. Therefore, the application of XFEM in concrete structures is mostly limited to study the linear elastic cracking ,without the consideration of non-linearity of material. Therefore, the stiffness recovery after crack closure can not be treated by XFEM as well as the multi-crack propagation and intersection problems.

In view of these previous difficulties, Dugdale (Dugdale, 1960) and Barenblatt (Barenblatt et al., 1962) proposed a new method named as cohesive zone model (CZM) based on linear elastic fracture mechanics (LEFM). Subsequently, CZM was used to study the fracture of brittle materials like concrete (Hillerborg et al., 1976), (Xu and Needleman, 1994)). As the main idea of the CZM is to treat the cohesive zone element as surface cracks, the crack grows between the classical elements while the cohesive zone is used to reproduce the cracks. Therefore, this method is the most consistent numerical method with the physical mechanism. However, crack path obtained by CZM exhibits a highly sensitivity of the used mesh (Klein et al., 2001).

## 4.2 Non-local methods

In practice, material is composed of discrete particles, whose interactions occurs within a certain spatial distance. The classical continuum mechanics and related theories developed on its basis, which are called as local theory, cannot take into account these interactions. On the contrary, the non-local theory has established a bridge between classical continuum mechanics and molecular dynamics (see Fig. I .19). The idea of non-local continuum theory originated from the end of nineteenth century. In 1893, Duhem (Duhem, 1893) pointed out that the stress at one point should depend on the state of whole structure. Different non-local theories are developed to solve different problems in subsequent researches.

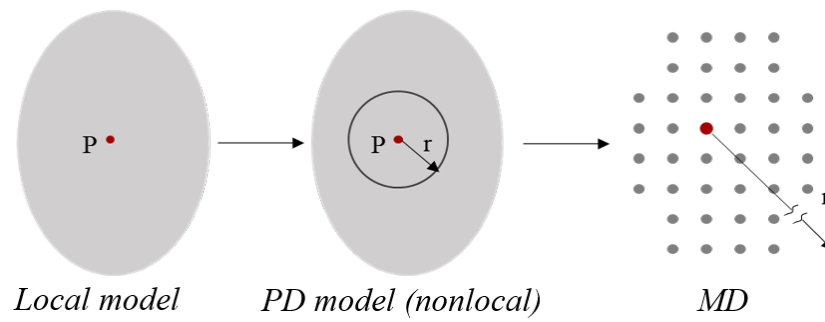


**Figure I .19:** Relationship among local model, non-local model and molecular dynamics

In 1964, Mindlin (Mindlin, 1963) imaged the micro-structure of materials as a volumetric micro-element attached to each material point. With the assumption that the macroscopic coordinate system is related to the microscopic deformation, the deformation and kinetic energy density can be defined. Combined with the principle of variation, a set of non-local governing equations are obtained. But these governing equations contain too many independent parameters for the engineering applications (Aifantis, 1992, 1999). Compared with the classical continuum mechanics theory, the differential non-local theory introduces characteristic scales and high-order differentials in space and time. Although it can consider the influence of the micro-structure of media, it requires more smoothness of physical quantities and is difficult to deal with discontinuity. Eringen and his colleges (Edelen et al., 1971; Edelen and Laws, 1971; Eringen, 1972; Eringen and Edelen, 1972) developed a non-local theory with the strain integration by using a weight function. This method is used to analyze the growth of linear elastic cracks (Eringen and Kim, 1974). The non-local theory has a great advantage in predicting the stress field around crack tip. Even though, similar with classical local theory in which the derivative of displacement is

contained in governing equations, most of non-local theory can not deal with the problems with discontinue deformation, such as cracks.

In 1980s, with the help of early work, Kunin ([Kunin, 1982, 1984](#)) developed the one- and three-dimensional elastic non-local theory based on the idea of continuous lattice model. This non-local theory doesn't contain space differential function and can then be used to solve the discontinuous problems. On the other hand, Lattice model ([Schlangen and Van Mier, 1992](#)) and molecular dynamics(MD) models ([Rountree et al., 2002](#)) are capable of simulating material damage and fracture at meso- and micro-scale, and they are the most detailed and practical method for predicting material fracture. In the MD simulations, the locus of atoms and molecules are determined by numerically solving Newton's equations of motion for a system of interacting particles. Additionally, the forces between the particles and their potential energies are often calculated using the interatomic potentials or molecular mechanics force fields. The difficulties associated with discontinue in classical continuum mechanics can be then resolved. However, it costs expensively calculation resources for simulating millions of atoms and molecules and is quasi impossible to modeling the real engineering constructions. Therefore, atomic research has always focused on the basic understanding of the basic physical processes of dynamic fracture, rather than being predictive ([Cox et al., 2005](#)). Although with the development of computer technology, large-scale molecular dynamics simulation becomes possible. Nevertheless, it is still not enough to use molecular dynamics to simulate the fracture process in actual structures.

In 2000, Silling ([Silling, 2000](#)), from Sandia National Laboratories, USA, proposed a non-local continuous model considering the long-range force in the absence of stress and strain, called peridynamics or peridynamic theory. In this method, the structure is discrete as particles, and their displacement is calculated by the integration in space. Multiple cracks are allowed to initiate and grow freely in any direction naturally without other special settings. The peridynamics overcomes the solution of complex spatial differential equations. For multi-scale problems, this method presents a great advantage in solving both macro- and micro-scale discontinuous problems ([Askari et al., 2008](#); [Jenabidehkordi et al., 2020](#)). In conclusion, PD is very efficacy in solving the crack initiation and propagation or progressive failure of solid materials such as concrete. The PD theory will be used to study the drying shrinkage cracks in cementitious materials.





## Chapter II

# Experimental Study of the Drying and Cracking of Cement-based Materials by X-Ray Microtomography

### 1 Introduction

In this part, the XCMT technique will be used to characterize the drying shrinkage cracks developed in concrete composites with different types of inclusions (aggregates). The emphasis is put on the effect of inclusion stiffness or rigidity and size on the process of drying shrinkage induced micro-cracking. In concrete, due to the great variability of inclusions (i.e. shape, size, distribution and porosity, etc.) and the potential reaction between cement matrix and inclusion, it is very difficult to analyze the mechanisms controlling the creation and development of cracks. In order to better study the effect of drying as well as the cracking characteristics, it is interesting to study materials with a simplified structure. For the sake of simplification and considering the idea initially proposed by Bisschop and van Mier ([Bisschop and Van Mier, 2002b](#)), the present work is performed on a cementitious composite. This type of composite allows us to study a simplified cementitious composite, in which spherical inclusions are distributed in a monodisperse manner.

A series of cementitious materials samples are fabricated by using different kinds of artificial inclusions of different rigidities and size. These samples are subjected to different levels of drying in order to create shrinkage-induced cracks. High-resolution X-ray micro-

tomographic images are taken from the cracked samples. The three-dimensional patterns of shrinkage-induced cracks are established and compared between the different samples. The influence of inclusion rigidity and size on the cracking patterns is analyzed and discussed. Then, the experimental data and results in this chapter will serve as the basis and starting point for the following numerical simulations.

This chapter is organized as follows. Firstly, a summary of the experimental study and main results obtained in a previous experimental study reported in (Li et al., 2020) is presented. The main objective of this experimental study was to investigate the influence of inclusion stiffness on drying shrinkage induced cracks in a concrete composite. Referring to the experimental analysis method of this experiment, and considering the influence of other factors of aggregate on the mechanical properties of concrete, the following experimental study of the effect of inclusions size on drying cracks morphology is presented. In this section, first of all, the sample preparation procedure, experimental device and testing program is described in detail. Qualitative results on the shrinkage-induced cracks patterns are shown.

## 2 Effect of inclusions rigidity

In this section, the experimental study and main results obtained in the work of Li et al. (Li et al., 2020) is presented. The main objective of this experimental study was to investigate the influence of inclusion stiffness on drying shrinkage induced cracks in a concrete composite.

### 2.1 Sample preparation and experimental program

A typical CEM I 52.5 cement was used according to the European standards. A W/C ratio of 0.5 was adopted and the volume fraction of inclusions was 40%. Five types of artificial aggregates (inclusions) with different stiffness were used: Zirconium (Zr-200), Titanium (Ti-112), Glass (Gl-68), Polyamide (Pom-3) and polyoxymethylene (Pam-2) (see Fig.II .1). Therefore, five groups of concrete composite samples were fabricated. These five spheres have a smooth, rounded surface with the objective of minimizing the bonds at the interfaces between cementitious matrix and spheres. The diameter of spheres is  $2mm$  in order that the opening of cracks is sufficient to be detectable at the available resolution of  $7\mu m$ . It should be noted that the volume fraction of inclusions is 40% in each composite. In order to fit the field of view of camera used in the microtomographic analysis, the cylindrical samples is selected to be  $8mm$  in diameter and  $15mm$  in height.

The main properties of inclusions (density, Young's modulus, Poisson's ratio, Hardness, thermo-hydric properties) are given in the Table.II .1. And the coefficient of linear thermal expansion for the cement paste used in this study is  $10 \times 10^{-6} / ^\circ C$  (Chen and Chung, 1995).

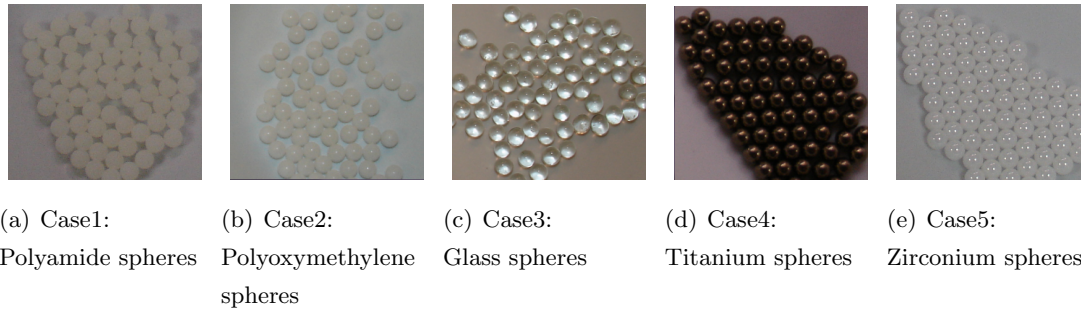


**Figure II .1:** Different inclusions used in this study

All the samples were firstly conserved in a lime saturated solution at a temperature of around  $20^\circ C$  to ensure the maturation of cement matrix and a full water saturation state. In order to accelerate drying process and enhance shrinkage induced cracking, two successive accelerated drying steps with high moisture gradient were adopted. In the first step, the fully saturated samples were suddenly put into a climate chamber with a relative humidity (RH) of 12% and a temperature (T) of  $20^\circ C$ , during 30 days until the mass stabilization of samples. During the second drying step, the temperature was increased to  $105^\circ C$  and maintained for about 20 days, and finally cooled to  $20^\circ C$ . The evolution of relative humidity and temperature and relative mass loss over time is shown in Fig.II .2 and Fig.II .3, respectively.

## 2.2 Experimental results

The micro-structural evolution and cracking patterns of dried samples are characterized with the help of X-ray micro-tomographic imaging technique (Li et al., 2020; Limodin et al., 2020). For this purpose, images are taken at the initial saturated state, at the end of the first step of drying and at the end of the second step of drying after cooling. Due to the limitation of the experimental equipment, we have not been able to scan the sample at a constant temperature of  $105^\circ C$ , therefore the effects of thermal expansion caused by the increase in temperature were not specifically considered separately in the experiment, and there were no images scanned at the beginning of the second stage. As a result, for the cracks of the second stage of case 1 and 2, we cannot do the quantitative analysis. However, for case 3, 4, and 5, due to their little difference with the coefficient of

	Case1	Case2	Case3	Case4	Case5
Meteriels	Polyamide 6.6	Polyoxymethylene	Glass	Titanium	Zirconium
Density ( $g/cm^3$ )	<u>1.14</u>	<u>1.40</u>	<u>2.50</u>	<u>4.45</u>	<u>6.05</u>
Young's modulus ( $GPa$ )	1.70-2.00	2.40-2.80	<u>68</u>	112	<u>200</u>
Hardness**	<u>100D</u>	<u>80D</u>	<u>465-585HK</u>	<u>28-42HRC</u>	1100HV
	78-121HRR	69-121HRR	450-550HV	290-420HV	
	85-180MPa BIH	30-179MPa BIH			
Coefficient of linear thermal expansion ( $10^{-6}/^{\circ}C$ )	70-100	80-100	<u>9.6</u>	8.9	<u>10</u>
Conductivity thermal ( $W.m^{-1}.K^{-1}$ )	0.2-0.3	0.2-0.31	<u>1</u>	16	<u>2</u>
Water absorption	2-4%	0.25%	-	-	-
Poisson's ratio	0.38-0.45	0.35-0.43	0.17-0.25	0.26-0.34	0.23-0.32

**Table II .1:** Parameters for different materials of inclusions\*

\* The underlined numbers are provided by the material production company, the others numbers are obtained from data investigation and for reference.

\*\* Hardness Knoop (HK); Hardness Shore Durometer (D); Hardness Vickers (HV); Hardness Brinell (HB); Hardness Rockwell (HR); Ball Indentation Hardness (BIH). These methods are suitable for measuring different kind of material, and there is no direct and unique conversion formula, only some empirical methods.

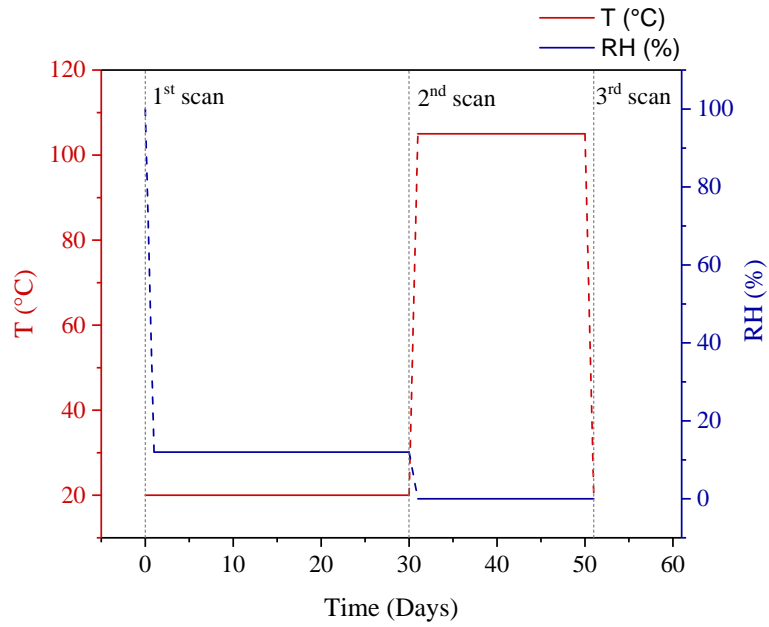


Figure II .2: Evolution of relative humidity and temperature over time

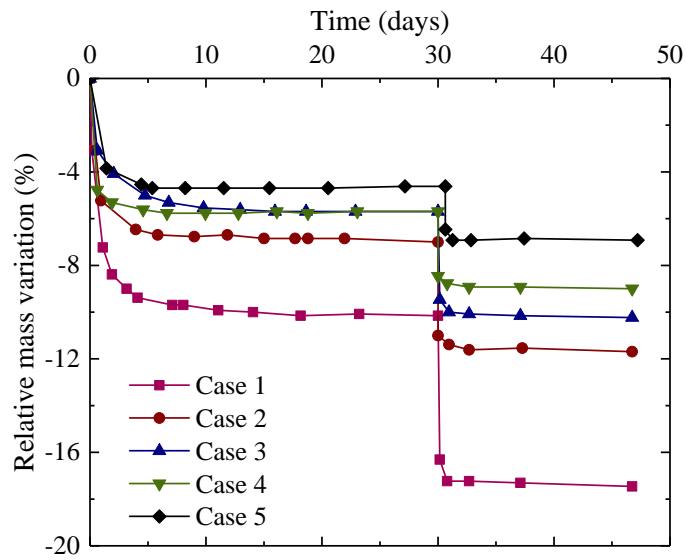


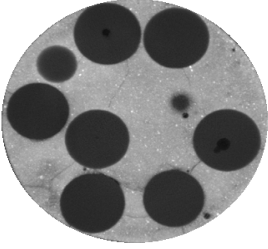
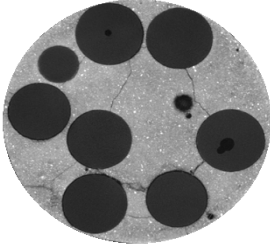
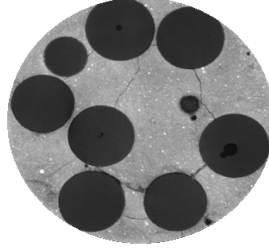
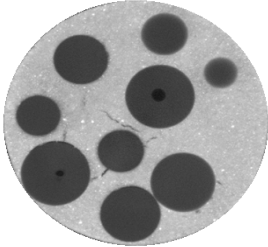
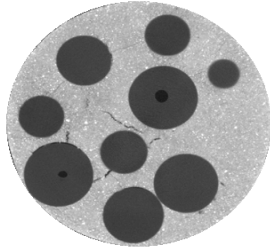
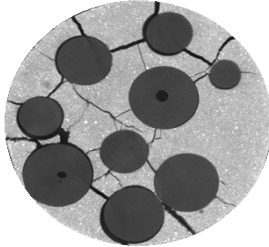
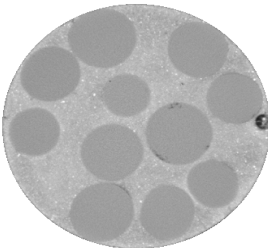
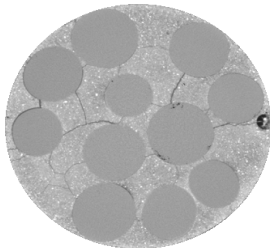
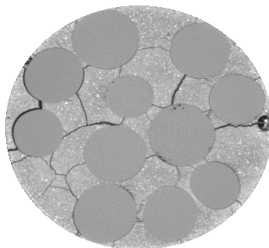
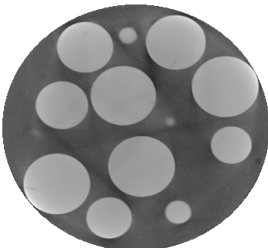
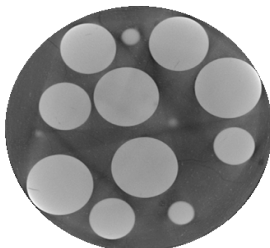
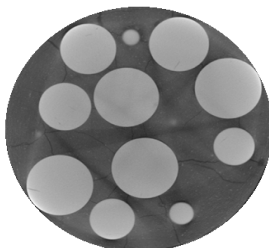
Figure II .3: Evolution of relative mass loss over time

linear thermal expansion of cement paste and low thermal dilatation coefficients, we can assume that thermal expansion effect is supposed negligible on cracks. While full three-dimensional images were obtained by using X-ray micro-tomography, as examples, only the reconstructed images of some selected cross sections at the mid-height of samples are presented in this paper and shown in Table.II .2. It worth noticing that for the samples with Zirconium (Zr-200) balls, the contrast between cement matrix and inclusions was not high enough to get clear reconstructed images of cracks. They are not presented in Table.II .2.

For different types of specimens, a growing quantity of cracks is observed as the drying process proceeds. The crack generation pattern of case 1 and case 2 is not quite the same as the other cases due to the water-absorbent characteristics and the high thermal expansion coefficient of inclusions. In the other cases, the crack generation and distribution patterns which are similar, are mainly in two forms. One is the debonding between the cement matrix and inclusions. Another one is radial cracks around the inclusions which connect different inclusions.

In general, cracking characteristics in the samples strongly rely on the inclusions type. When moisture is lost from the sample to the surrounding environment, a moisture gradient will be formed in the entire sample, resulting in differences in matrix shrinkage. The presence of rigid inclusions would restrain the free shrinkage of cementitious matrix. This restraining will cause radial and tangential stresses around the aggregate particles, called local effects, and cause radial and bonded micro-cracks. The local effects increase with the Young's modulus.

In the samples with a higher Young's modulus, a greater increase in the crack surface is observed with an increase of the inclusions' stiffness , specially in the dramatically dried specimens ( $T= 105^{\circ}\text{C}$ ). This observation tends to be confirmed by a greater number of thin cracks and a greater cumulative length of cracks in titanium composite than in glass one (see Fig.II .4).

	Saturated (T = 20°C)	Drying, end of step 1 (T=20°C HR=12%)	Drying, end of step 2 (T=105°C)
Case1 (Pam-2)			
Case2 (Pom-3)			
Case3 (Gl-68)			
Case4 (Ti-112)			

**Table II .2:** Reconstructed images of representative cross-sections in different samples et different steps of drying (Li et al., 2020)

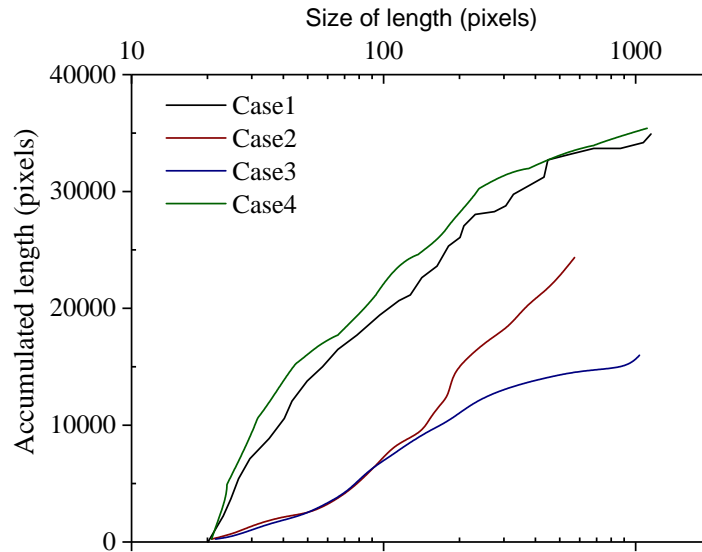


Figure II .4: Accumulated length of cracks in different samples (step 2)

### 3 Effect of the inclusions size

As an important component of concrete, the properties of aggregates have a great influence on the drying cracks in concrete (Idiart, 2009). However, the evolution of micro-cracks and their dependence on the size of aggregates is not fully understood yet. Inspired by the previous experimental approach, a similar experimental study on the effect of inclusions size on drying shrinkage cracks is carried out in this section.

#### 3.1 Sample preparation and experimental program

##### 3.1.1 Sample preparation and drying procedure

In order to study the effect of inclusions size on cracks, the samples of cementitious composite were made with a volume fraction 35% of spherical inclusions and a volume fraction 65% of cement paste, and the inclusions were selected with glass beads of 2mm and 3mm diameter, respectively.

The material of glass has been selected to better achieve micro-tomographic imaging and taking advantage of the difference of X-ray attenuation coefficient between cement paste matrix and inclusions: its attenuation is not too different from the cementitious matrix and this can limit (but not totally avoid) the loss of precision of the image at



the matrix-inclusion interface, while allowing to distinguish the 2 phases of matrix and inclusions. Moreover, the glass beads (i.e., the silicone material) have a rigidity close to that of the more commonly used silicone aggregates in concrete.

The diameter of inclusions with  $2mm$  and  $3mm$  is selected so that the opening of cracks is sufficient to be detectable at the available resolution (Li et al., 2018). The specimens were manufactured as cubes measuring  $20mm \times 20mm \times 160mm$  where the height is much larger than the length and width. Therefore, in subsequent numerical simulations, the intermediate cross-section can be considered as a plane strain problem for the numerical modeling of the evolution of dry cracking. To eliminate the influence of some factors, three samples with the same diameter of inclusions for every cases has been made for the purpose of comparison. A typical CEM I 52.5 of cement is used with respect to the European standards. The W/C ratio 0.5 is adopted and is capable of ensuring a casting without requesting strong vibration. For each type of cementitious composite, samples are casted and conserved in lime saturated solution under  $20^\circ C$  for more than one month to ensure a hydration already well advanced and a micro-structure that will not evolve too much in the future.

Materials	Density ( $g/cm^3$ )	Young's modulus (GPa)	Poisson's ratio
Glass	2.50	68	0.17-0.25
Cement paste	1.53	15	0.1-0.18

**Table II .3:** Parameters for materials of inclusions and cement matrix (Li, 2016)

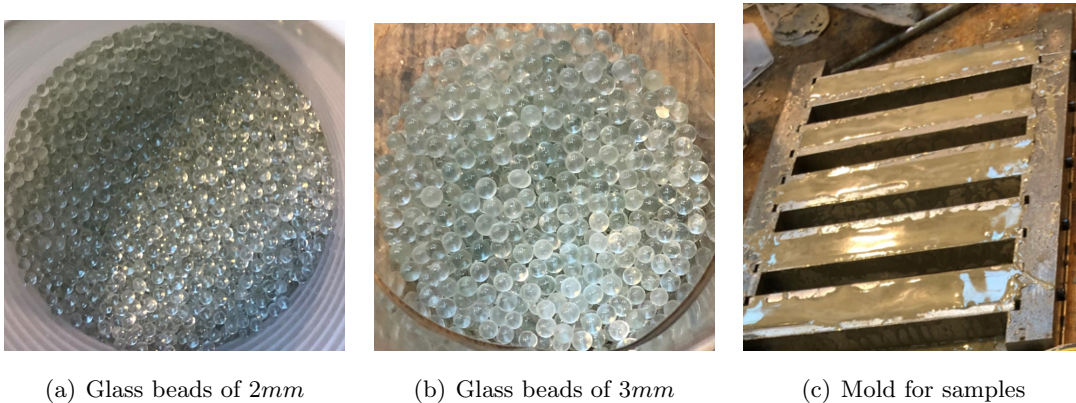


**Figure II .5:** Illustration of the glass beads and the molds used

In order to study the evaluation of cracks induced by drying shrinkage of the cement paste on first-drying stage in low humidity environment, all the samples are firstly kept at a temperature of 20°C in a lime saturated solution to ensure the maturation of the cementitious matrix and a full water saturation of specimens. Then they are subjected to drying at a temperature (T) of 25°C and a relative humidity (RH) of 50% until the stabilization of the mass of the sample. In the laboratory tests, the temperature and relative humidity are controlled by a Vötsch® or Binder® climatic chamber. The weight measurement is performed by using a balance with precision of ±0.01g. When the weight variation of studied sample is less than 0.1% during 7 days, the stabilization of the drying process is supposed achieved. A normalized weight loss of the cementitious matrix by assuming no mass loss of inclusions of the samples are given in Fig.II .6. The percentages of weight loss are similar for both types of samples.

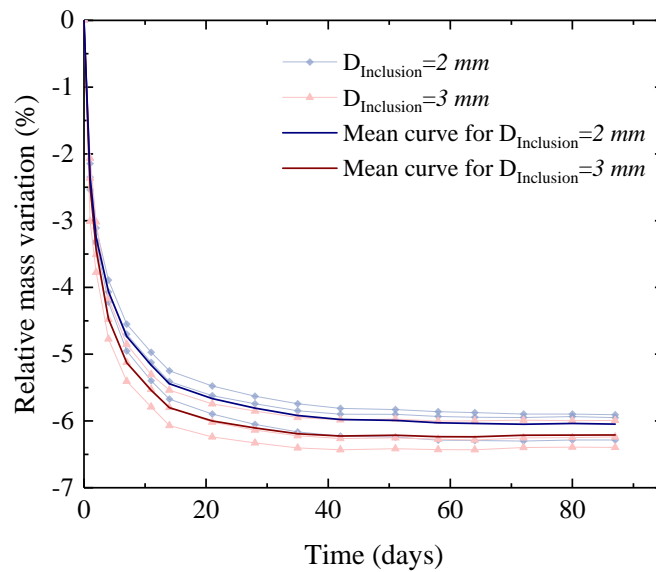


**Figure II .6:** Evolution of the relative mass variation of the samples with drying time

The shrinkage of the specimen was measured using a retractometer. Since the specimen was fitted with a stud before casting, the length difference between the specimen and a known length of reference bar in Invar (160 mm) was read with the help of the ball on the bottom of the retractometer’s measuring bar (see Fig. II .7). The shrinkage of the samples are given in Fig.II .8. The different shrinkage for each type of sample in the figure are mainly due to the different amount of cracking created during the drying process. This

measurement of shrinkage on a macroscopic scale shows clearly different shrinkage for the two size of inclusion. Moreover, it is necessary to study these phenomena on a smaller scale in order to properly observe the effect of inclusions and their diameter on cracking.

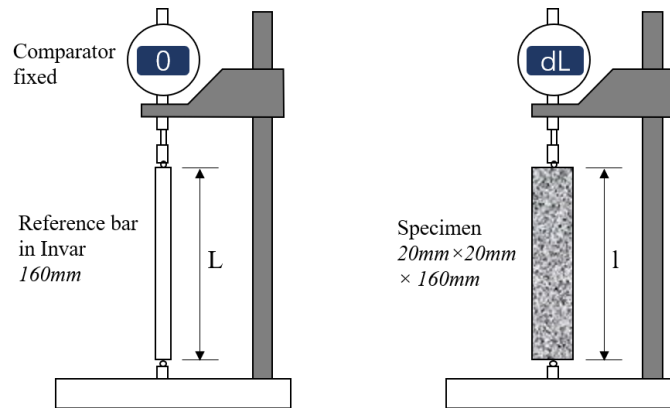


**Figure II .7:** Principle of shrinkage measurement with a retractometer

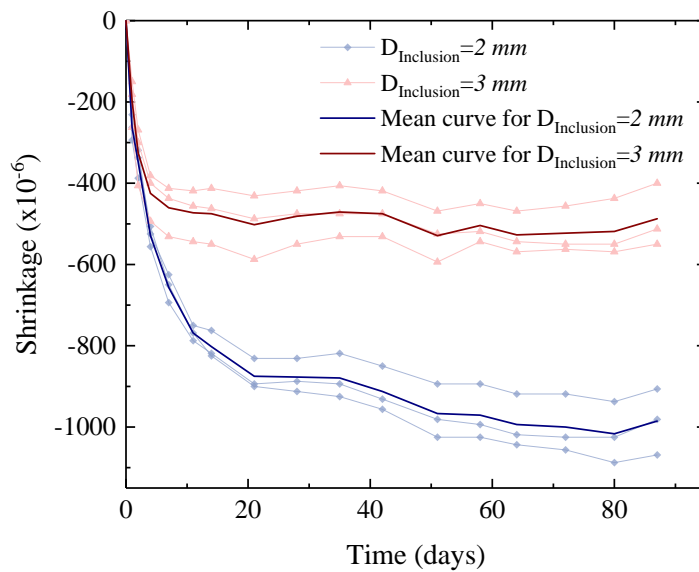


**Figure II .8:** Evolution of the shrinkage of the samples with drying time

The relationship between mass loss and shrinkage is shown in Fig. II .9. It can be seen that the variation of drying shrinkage with mass loss during the drying process shows three stages, as indicated in the figure. The first stage shows a strong shrinkage change accompanied by mass loss. The drying front develops from the edges of the material to the

inner part of the material, causing shrinkage under the influence of capillary depressions. The second stage exhibits mass loss without significant shrinkage changes. The advance of the drying front leads to a homogenization of the saturation (an important mass loss), accompanied with shrinkage reaching a stable value. Finally, the third stage shows an increase in shrinkage without mass loss. In this stage, since the saturation of the material at the end of the previous stage has reached a state homogeneous, capillary depressions no longer play a role and the shrinkage rate has also reached a steady state in the previous stage. Therefore, the shrinkage in this phase is a phenomenon of drying creep in concrete (Wittmann and Roelfstra, 1980).

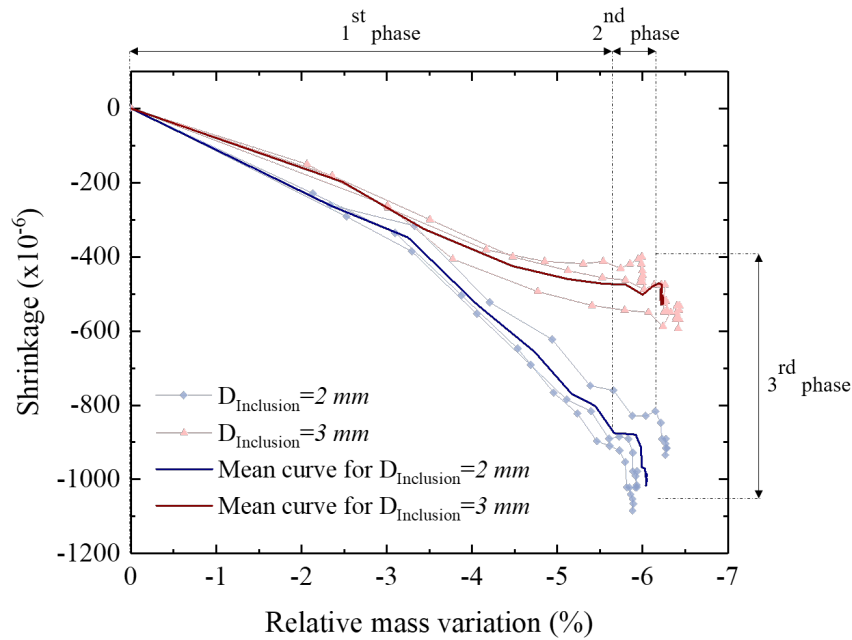


**Figure II .9:** Evolution of the shrinkage of the samples with relative mass variation of the samples

### 3.1.2 Micro-tomographic acquisition

The micro-structural evolution of dried samples are analyzed with the help of X-ray micro-tomographic imaging technique. For this purpose, images are taken at the initial saturated state and at the end of drying. The acquisition of micro-tomography data is carried out in the ISIS4D imaging platform (Limodin et al., 2020), as shown in Fig.II .10. X-ray micro-tomography is a fast-growing non-destructive method that aims at obtaining 3D non-destructive images of the material structures (Shi et al., 2020), which is mainly composed of a signal source and a detector. The voxel size in these images is in the

micrometer scale. The basic principle is to use X-ray to penetrate the object. Due to the different internal components of the sample, different absorption rates will be generated. Then the detector collects the attenuated X-rays and converts them. Transmission microtomography exploits the Beer-Lambert's law and transforms it into inverse Radon and the 3D reconstruction is generally performed through a filtered back projection algorithm. After the X-ray emitted by the X-ray generator penetrates the object, the attenuated signal conforms to the following attenuation equation of Beer-Lambert's law (Latiere and Mazerolle, 1987):

$$I = I_0 \exp(-\mu x) \quad (\text{II}.1)$$

Where:  $I$  is the attenuated intensity X-ray,  $J/(\text{cm}^2 \cdot \text{s})$ ;  $I_0$  is the incident intensity of X-ray,  $J/(\text{cm}^2 \cdot \text{s})$ ;  $\mu$  is the absorption coefficient of the substance irradiated by X-ray,  $x$  is the thickness of the object.

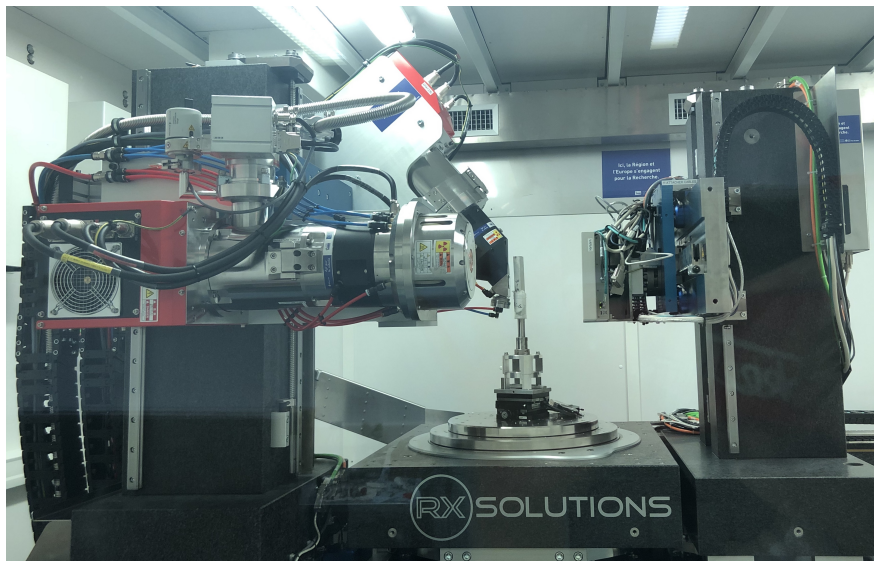


**Figure II .10:** The microtomography equipment (platform ISIS4D)

The key step of X-ray micro-tomography to realize the 3D imaging of material interior is to use different projections (radiographs) under different angles obtained during the rotation of the sample. The objective of computed tomography image reconstruction is to determine how much attenuation of the X-ray beam occurs in each voxel of the reconstruction matrix. These calculated attenuation values are then represented as gray levels in a two-dimensional image of the slice (Goldman, 2007). After all the 2D images

are stacked in order, a 3D image can be obtained. The procedure for a tomographic scan is summarized in the Fig.II .11. The spatial resolution of X-ray micro-tomography can generally vary from several hundred nanometers to several hundred microns.

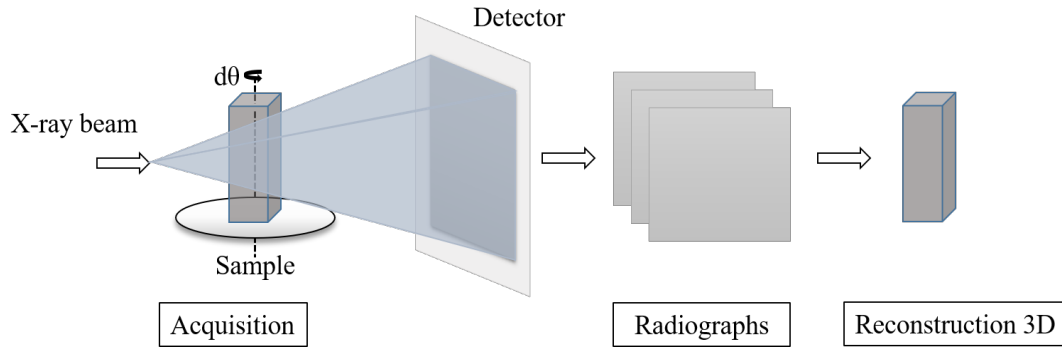


**Figure II .11:** Sketch of acquisition and reconstruction of micro-tomography

Usually, the sample is rotated  $180^\circ$  or  $360^\circ$  along its vertical axis. A series of acquired two dimensional radiographs can be used to obtain a three dimensional reconstructed image through different existing calculation methods, such as filtered back projection algorithm (Goldman, 2007). The operation voltage was set at  $80kV$  and the filament current was set to  $250\mu A$ . The X-Ray beam is produced by a microfocus X-ray tube with a tension of  $230kV$ . The flat panel detector has a resolution of  $1874 \times 1496$  pixels. In our scanning experiment with XCMT, we assume that the voxel size is the resolution of the instrument. As the voxel size used in this study is about  $18\mu m$  which is also the resolution, cracks with a width smaller than this value were not demonstrated in the present study while the cracks with a width between  $18\mu m$  and  $36\mu m$  were also difficult to distinguish. In order to eliminate the influence of the boundary and to improve the scanning efficiency, we selected a height of  $2cm$  in the middle of the specimen for scanning analysis. 4320 radiographs were taken while one sample was rotated through  $360^\circ$  along its vertical axis. Reconstruction of the tomographic data is performed with a filtered back projection algorithm using X-act software (Shi et al., 2020). Based on the reconstructed 3D volume, the cracks networks developed in the samples are identified, visualized and quantified. The image segmentation is performed by using the gray values of every voxel. The various constituents can be distinguished visually by the difference of gray level induced by their different X-ray absorption coefficients.

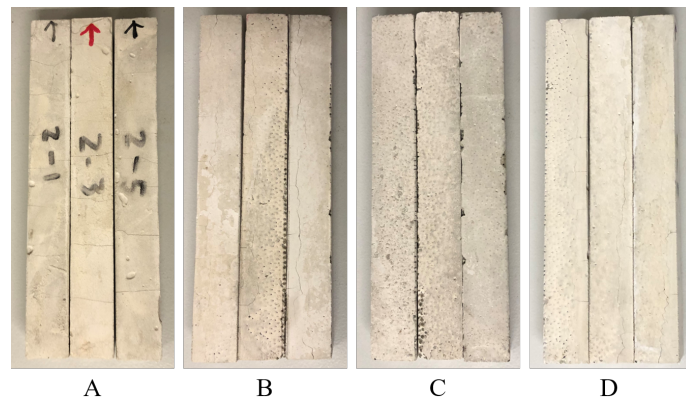
## 3.2 Experimental results

### 3.2.1 First qualitative results of cracking patterns

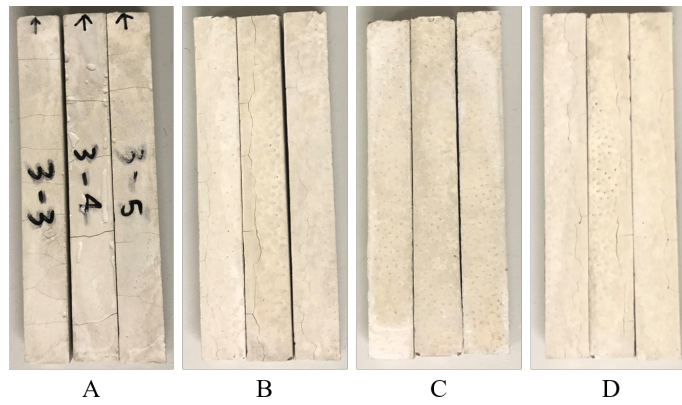
The main experimental results obtained on two types of laboratory samples are presented in this section. In order to illustrate the influence of the inclusion size on the shrinkage cracks of cementitious composite, the experimental results of saturated and after drying states are compared and analyzed. The debonding at the interfaces between the cementitious matrix and inclusions can also be clearly seen.

Fig. II .12 presents the surfaces cracking of two specimens with different diameter inclusions after the drying process. Due to the segregation of inclusions during the sample preparation process, the material in the upper part of the sample is mainly cement matrix, and surface cracks are mostly found in this part (A side). On the B and D side, cracks are located at the part dominated by cement matrix and at the interface between inclusions and matrix. On the C side, surface cracks are difficult to be observed in this part where the inclusions are concentrated due to the segregation. These are only surface observations which give only a partial view of the effects of drying on cracking.

The microtomographic acquisitions will be able to more deeply investigate the effect of drying on those samples. After the 3D reconstruction, a three-dimensional image of the specimen is obtained. Thus, it is possible to make "virtual" slices within this image at any position of the specimen, an example of a specimen with 3mm diameter inclusions is shown in Fig. II .13. As it can be seen that the presentation of the experimental results and numerical simulation model are the cross-sections perpendicular to the axis of revolution of the sample, it is for the reason that the drying process is mainly radial. The Fig. II .14 shows selected cross-sections inside the samples. The different components can be visually distinguished according to the obtained X-ray attenuation: the weaker the attenuation, the darker color the figure presents. As a darker color indicates a low density of the material, anhydrous cement grains are presented in the form of very white spots while air bubbles appear in the form of dark circles. And in the corners, they are artifacts because of the shape of the section (square section). In the initial saturated states, no cracks are visible in the samples. In the end of the drying stage, cracks can be observed in the sections of two samples with a similar distribution pattern. In the crack distribution pattern, cracks are mainly found in the interface debonding between inclusions and matrix and in the connections between different inclusions.

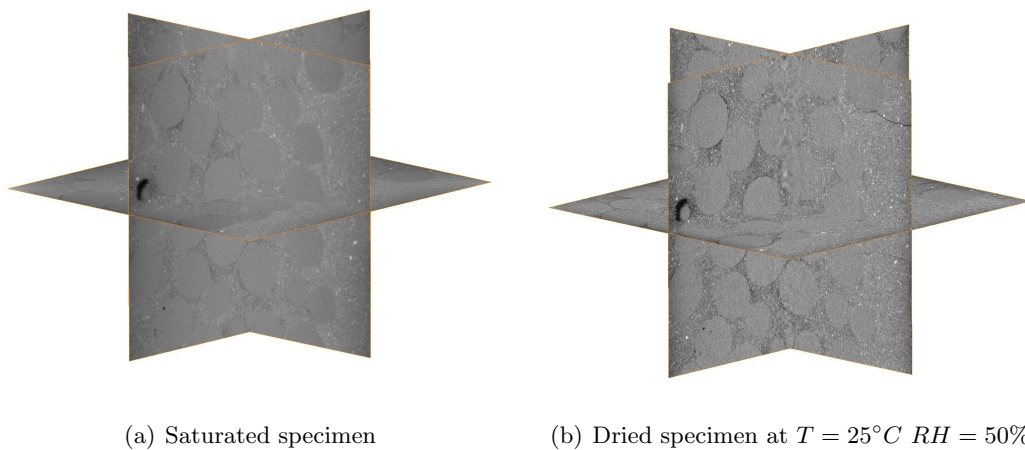


(a) Sample with inclusion of 2mm



(b) Sample with inclusion of 3mm

**Figure II .12:** Images of different samples at the end of the drying procedure



(a) Saturated specimen

(b) Dried specimen at  $T = 25^{\circ}C$   $RH = 50\%$

**Figure II .13:** Visualization of specimen saturated and after drying process under X-ray microtomography in horizontal and vertical sections ( $D = 3mm$ )



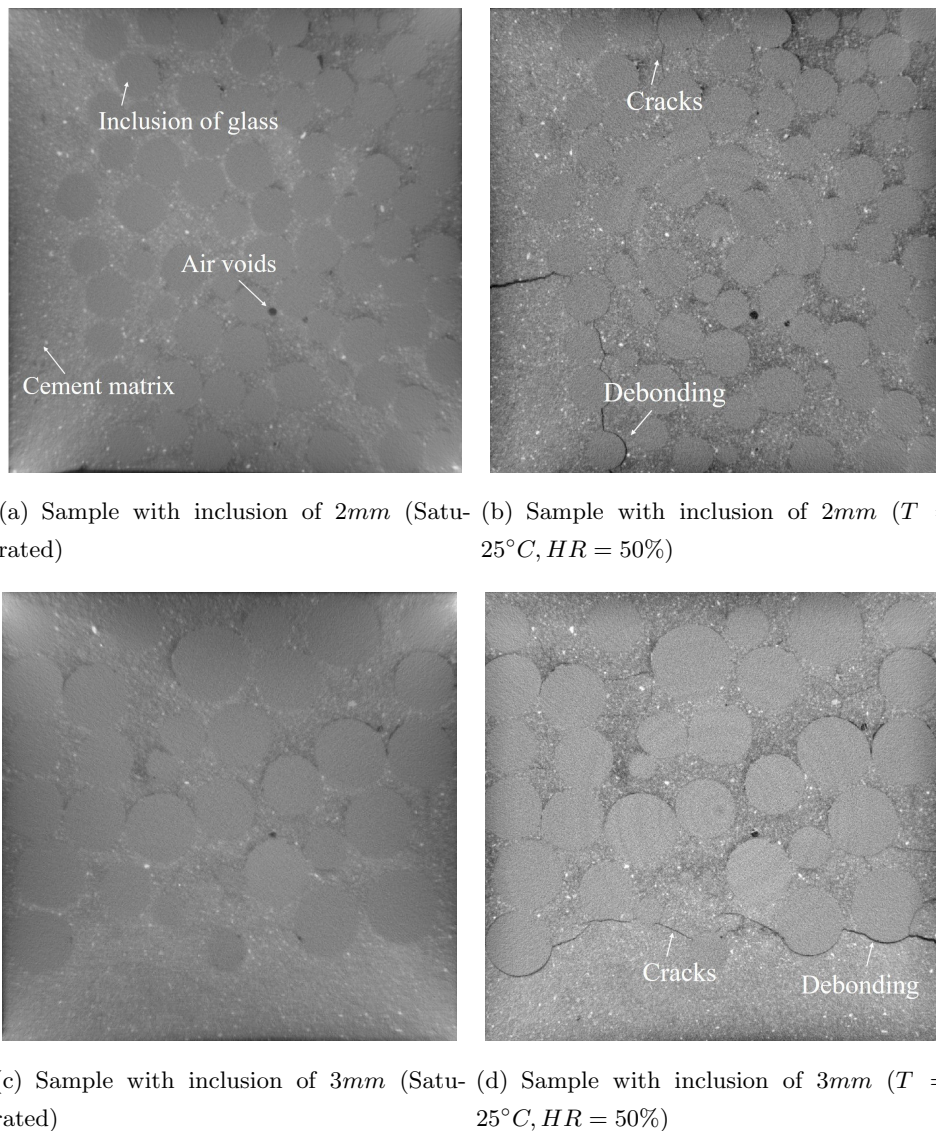


**Figure II .14:** Representative cross-sections of different samples at different steps of drying

Indeed, by assuming that no water is present inside the inclusions, the drying leads to the decrease of water content in the cement paste. The desaturation induced the volumetric shrinkage of cement paste. Due to the presence of inclusions with a higher stiffness than that of the cement paste, the free shrinkage of the cement paste is restrained. This will generate a stress concentration around the inclusions and the creation of cracks. In the case of spherical particles, tensile tangential and compressive radial stresses are generally generated around the inclusions. The tensile tangential stress leads to the nucleation and

propagation of radial cracks. When cracks appear, shear stresses will develop along the interface and reach the maximum near the interface, which may cause a bonding crack (see Fig.II .15).

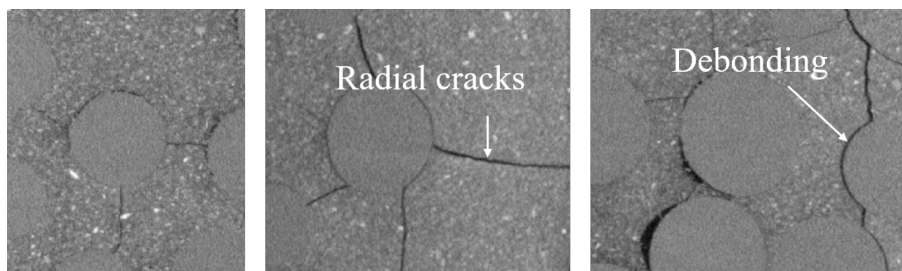
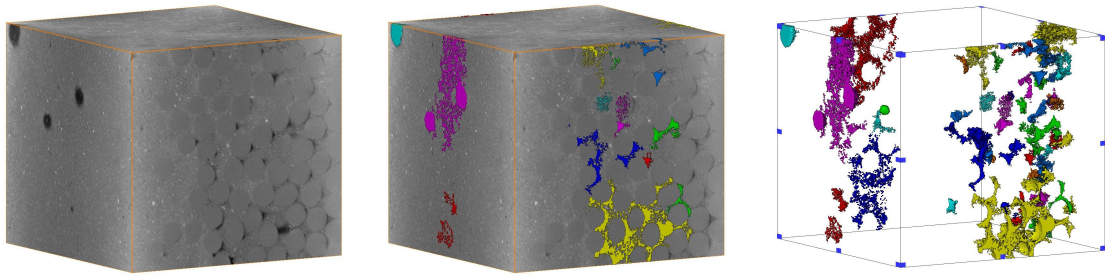


**Figure II .15:** Crack patterns surround the inclusions

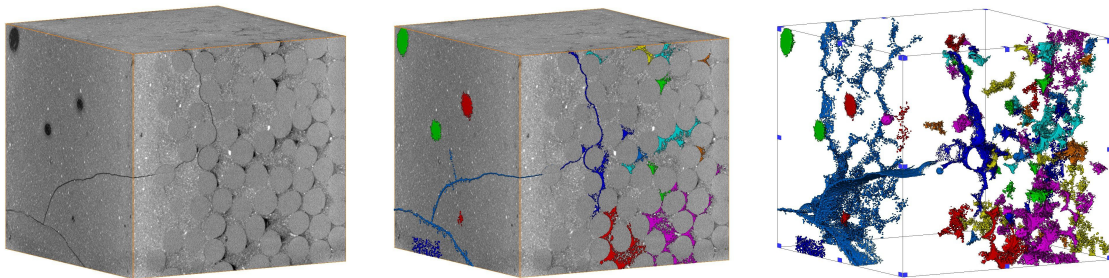
### 3.2.2 Identification and quantification of the crack network

The crack network in two types of cementitious composite are compared and analyzed in this section. The image analysis is realized by the method of image segmentation. It is obtained by using the gray values of every voxel. It is a more or less automated procedure that allows to remove unnecessary structures from the image. The objective is to be able to quantify on all samples the evolution of the micro-structure, and in particular the cracking with drying. By using this image analysis procedure, cracks can be clearly visualized and given in 3D reconstruction volume (see Fig.II .16). Different colors represent different unconnected cracks. The color assignment is also randomly generated by the image analysis software. One can note that the gray values at surfaces of the specimen are often prone to bias and interference information are more easily introduced during image segmentation. Therefore, in Fig. II .16, the surface of the scanned specimen has many dense areas of cracks in both the saturated and dried states.

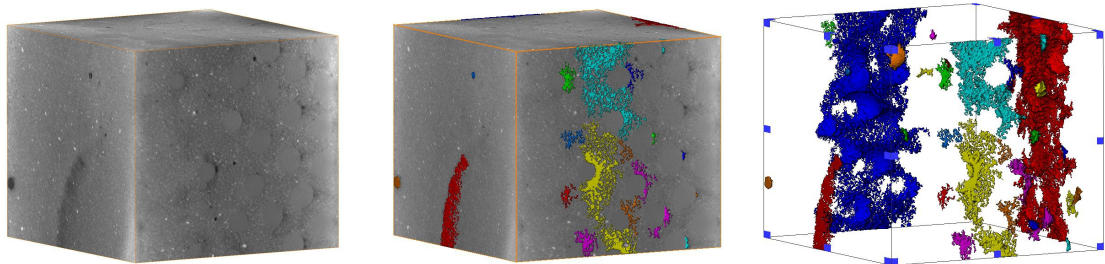
Here we are more concerned with the development of the crack network, so that the cracked area is separated and compared in the following quantitative analysis according to the level of drying. Compared with the initial state, the initiation and development of cracks in the dry state can be clearly observed. In the figure, it can be seen that the largest cracks can be observed in the part where the volume fraction of inclusions is lower. The change in volume fraction of cracks and pores was 47% for the 3mm sample, which was higher than the 42% change for the other type of sample.



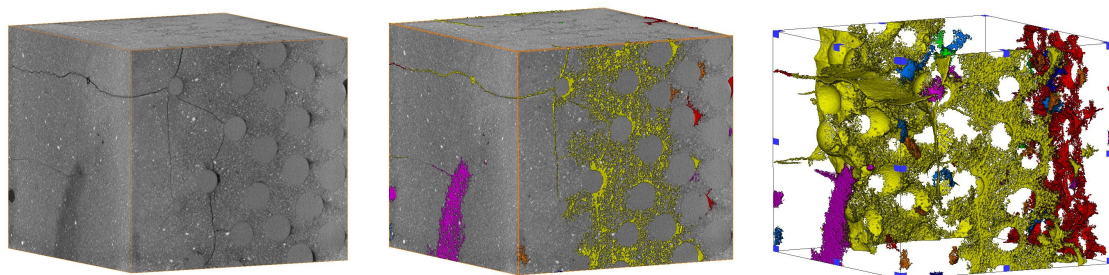
(a) Sample with inclusions of 2mm (Saturated)



(b) Sample with inclusions of 2mm ( $T = 25^{\circ}C$ ,  $HR = 50\%$ )



(c) Sample with inclusions of 3mm (Saturated)



(d) Sample with inclusions of 3mm ( $T = 25^{\circ}C$ ,  $HR = 50\%$ )

**Figure II .16:** Evolution of the 3D crack network in different samples

## 4 Concluding remarks

In the present work, an experimental study has been performed to investigate the influence of inclusion size on drying shrinkage-induced cracking in concrete composites. Based on the obtained results and the experimental observations of the previous work (Li et al., 2020), the following main remarks can be formulated.

- X-ray micro-tomography permits us to acquire three-dimensional images of the interior structure with high resolution. It is a powerful non-destructive technique which is well applicable for the analysis of crack propagation during the drying of cementitious composites;
- The experimentally observed results show that the distribution of cracks induced by dry shrinkage is independent of the inclusions size. More specifically, the cracks are mainly generated around the interface between the inclusions and the matrix and show an emission pattern connecting the different inclusions;
- Based on the change in the volume fraction of cracks and pores before and after drying, it can be concluded that the quantity of cracks generated by the drying process increases with the increase of inclusions size.
- Due to the fact that grayscale values on the specimen surface are often prone to deviation, it is easier to introduce interfering information in the image segmentation process. More work needs to be done in experimental and numerical simulations to quantify the quantity of cracks more precisely and to analyze the effect of different inclusions on the evolution of micro-structure and cracks in the drying process.
- By the experimental observations of the previous work (Li et al., 2020), it can be concluded that the restraining effects of inclusions become more important during the drying processes with the increase of the Young's modulus of inclusions.

## Chapter III

# Peridynamic Model of Concrete and Numerical Verification

### 1 Introduction

The peridynamics theory (PD) has been initially developed by Silling ([Silling, 2000](#)) in order to describe the mechanical behaviors of continuum media with or without discontinuities. It has been extended and applied to different kinds of mechanical and multi-physical problems during the last two decades. Like all numerical methods, the PD theory has its advantages and short comings. In this theory, integral equations are solved instead of partial derivative equations in classical continuum mechanics framework. The PD theory is then particularly suitable for solving problems with discontinuities such as cracking process. It is able to naturally capture the nucleation of cracks through the damage of internal material bonds and to reproduce different modes of fracture. It is also very convenient to deal with heterogeneous materials. This theory has been successfully applied to modeling damage and progressive failure in concrete materials and structures ([Li and Guo, 2018](#)).

In this chapter, the rapid review of the Bond-based Peridynamics theory is firstly presented. By using the developed PD code, a one-dimensional bar in tension is firstly analyzed to study the influence of adopted numerical models: the horizon size  $\delta$ , the grid size  $\Delta x$  and other factors on the calculation simulation accuracy. Then a numerical simulation of the typical problem of bending a two-dimensional concrete cantilever beam is performed and to verify the accuracy and effectiveness of the method in 2D simulating concrete problems.

## 2 Bond-based peridynamic theory

Peridynamics is a non-local model in continuum mechanics, there is an interaction between the material point and any material points within a finite distance in the reference configuration  $\mathbf{R}$ . Each pair of particles interacts via a vector function  $\mathbf{f}$ , in function of the position  $\mathbf{x}$  and the displacement  $\mathbf{u}$  to the reference point (Fig.III .1). According to the Newton's law, the peridynamics (PD) equation of motion at a material point  $\mathbf{x}$  and the time  $t$  is given as (Silling and Askari, 2005)

$$\rho(\mathbf{x})\ddot{\mathbf{u}}(\mathbf{x}, t) = \int_{H_x} \mathbf{f}(\mathbf{x}, \mathbf{x}', \mathbf{u}(\mathbf{x}, t), \mathbf{u}'(\mathbf{x}', t))dV' + \mathbf{b}(\mathbf{x}, t) \quad (\text{III .1})$$

where  $\rho$  is the mass density of material point,  $\mathbf{u}$  is the displacement vector field,  $\mathbf{b}$  is the prescribed loading force density field which represents the external force per unit reference volume.  $H_x$  is the neighborhood of material point  $\mathbf{x}$  within the horizon size of  $\delta$  (Fig.III .1), which is usually taken as a sphere in 3D problems (or a circle in 2D problems) centered at  $\mathbf{x}$

$$H_x = H(\mathbf{x}, \delta) = \{x' \in R : \|\mathbf{x}' - \mathbf{x}\| \leq \delta\} \quad (\text{III .2})$$

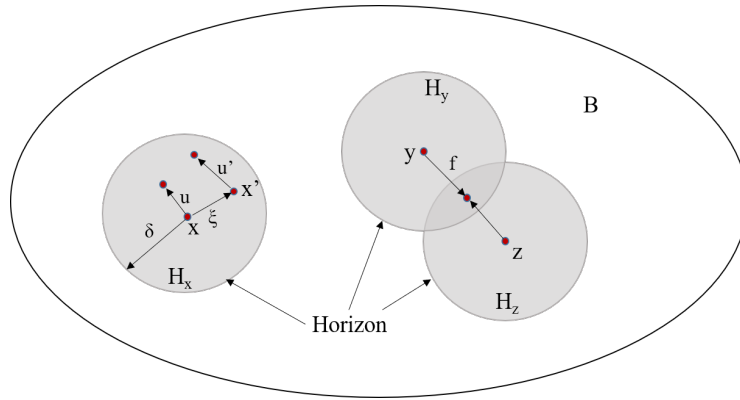


**Figure III .1:** Interactions between the points material

At present, Peridynamics mainly include two branches, Peridynamics based on "bonds" (BBPD) and Peridynamics based on "states" (SBPD). The bond-based Peridynamics assumes that the interaction forces between material points are equal in magnitude and opposite in direction, all along the direction of the line between two material points. According to whether the direction of the force state is consistent with the direction of the deformed form (the direction of the connection between the two material points after deformation), the state-based Peridynamics can be divided into two major categories, the ordinary state-based Peridynamics and the non-ordinary state-based Peridynamics. In the

ordinary state-based Peridynamics, the direction of the deformation and the direction of force state are consistent while in the non-ordinary state-based Peridynamics method, they are generally inconsistent. The difference between the interaction force function between BBPD and SBPD is as follows.

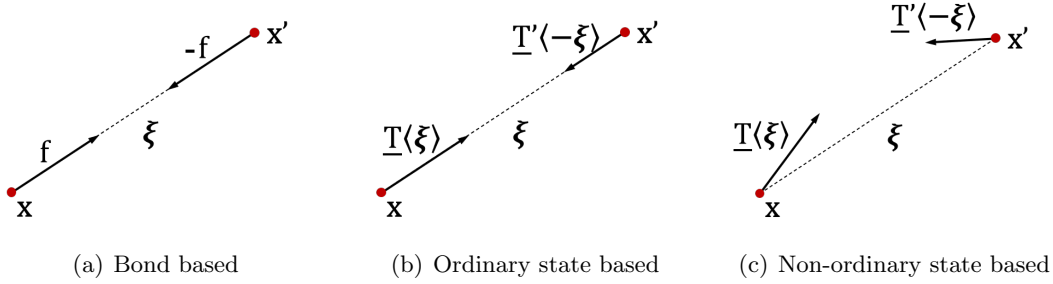


**Figure III .2:** Function of the force state in Peridynamics

The bond-based theory was developed prior to the state-based theory. And due to its simplicity, the BBPD method is widely used in Peridynamics studies and simulations. Nevertheless, the bond-based theory does suffer from certain limitations, with the most notable being the restriction of the Poisson ratio to 1/4 for isotropic elastic materials in plane strain and three-dimensional condition and 1/3 for plane stress (Gerstle et al., 2005). The recently developed state-based PD reformulations (Breitenfeld et al., 2014; Silling, 2010; Silling et al., 2007; Warren et al., 2009) and several modified bond-based PD models [38–40] have been devoted to eliminating such restrictions (Gerstle et al., 2007a,b, 2009).

In bond-based peridynamics each bond has its own constitutive relation that is independent of other bonds (Silling and Lehoucq, 2010). The function  $\mathbf{f}$  can be defined as the function of relative position of two particles in the reference configuration  $\xi = \mathbf{x}' - \mathbf{x}$  and their relative displacement  $\eta = \mathbf{u}(\mathbf{x}', t) - \mathbf{u}(\mathbf{x}, t)$ . And the function satisfies the conservation of momentum and angular momentum, so that the function  $\mathbf{f}$  can be expressed as

$$\mathbf{f}(-\eta, -\xi) = -\mathbf{f}(\eta, \xi) \quad \forall \eta, \xi \quad (\text{III .3})$$

$$(\eta + \xi) \times \mathbf{f}(\eta, \xi) = 0 \quad \forall \eta, \xi \quad (\text{III .4})$$

And  $\mathbf{f} = 0$  when  $\|\xi\| \geq \delta$ .

The direction of a pairwise force can be expressed by an absolute displacement vector

$\eta + \xi$ . Therefore, the general expression of the function  $\mathbf{f}$  can be expressed as follows

$$\mathbf{f}(\eta, \xi) = \begin{cases} \frac{\eta + \xi}{\|\eta + \xi\|} f(\eta, \xi) & \text{when } \|\xi\| \leq \delta \\ 0 & \text{else} \end{cases} \quad (\text{III .5})$$

In the above equation  $\mathbf{f}(\eta, \xi)$  represents the scalar value of force vector function, and the material information contained in the function can be used to describe various material behaviors. The non-local effect of particles  $\mathbf{x}$  and  $\mathbf{x}'$  at time  $t$  in the reference coordinate system are shown in Fig.III .3.

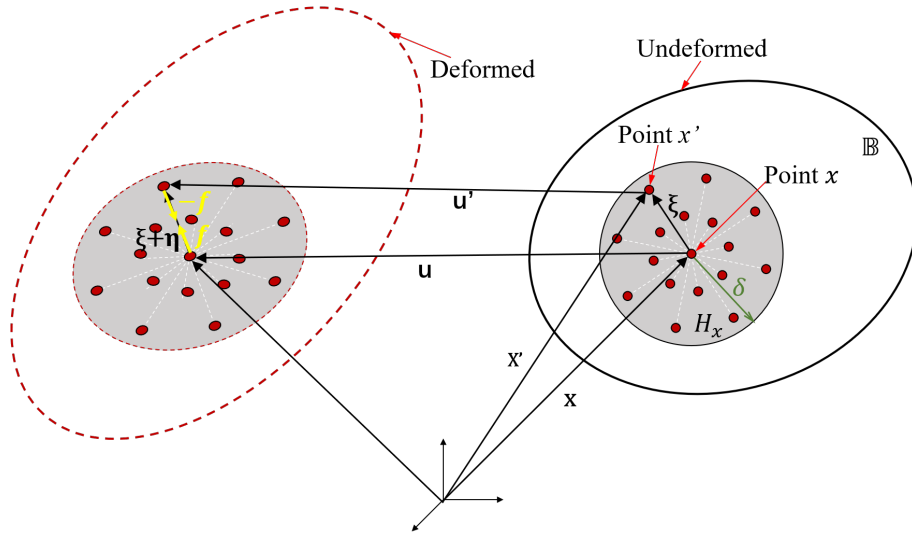


**Figure III .3:** Function of the force state in Peridynamics

Aforementioned, numerous experimental investigations have exhibited that under low confining pressure, the mechanical behavior of cementitious material is brittle and can be described by an elastic damage model (Jamet et al., 1984; Sfer et al., 2002). In view of this, the mechanical behavior of studied cementitious composites is described by using an elastic damage model. In the classical mechanics theory, if the material is considered as PD micro-elastic material, the pairwise force vector  $\mathbf{f}(\eta, \xi)$  needs to satisfy the net work done by the interaction between any particle  $\mathbf{x}'$  and the reference particle  $\mathbf{x}$  along any closed curve is zero, that is

$$\int_{\Gamma} \mathbf{f}(\eta, \xi) d\eta = 0 \quad (\text{III .6})$$

where  $d\eta$  represents the integral path length along the closed curve  $\Gamma$ . According to Stokes' theorem, the necessary and sufficient condition for PD material to be an elastic material is



that for any  $\xi$  not zero,  $\nabla_\eta \times \mathbf{f}(\eta, \xi) = 0$  and there must be a differentiable scalar function  $\omega$  that satisfies

$$\mathbf{f}(\eta, \xi) = \frac{\partial \omega(\eta, \xi)}{\partial \eta} \quad (\text{III .7})$$

where  $\omega(\eta, \xi)$  is called pairwise potential function (Jamet et al., 1984; Silling and Askari, 2005), it represents the potential energy in the bond of two particles ( $\xi$ ), each particle of the bond occupies 1/2 of the potential energy, so the potential energy per unit volume  $w$  (also called the local strain energy density) in an object can be expressed as

$$w = \frac{1}{2} \int_R \omega(\eta, \xi) dV_\xi \quad (\text{III .8})$$

## 2.1 Prototype microelastic brittle model (PMB)

After the BBPD theory was proposed, the prototype microelastic brittle model (PMB) proposed by Silling et al. (Silling and Askari, 2005) is the most widely used. The model assumes that the force between particles (bonds) is similar to a spring and depends on the elongation of the bond without considering lateral or torsional deformation. Therefore, the linear micro-elastic potential energy contained in the bond is also similar to the Hooke's law spring potential energy form. It can be expressed as the following

$$\omega(\eta, \xi) = \frac{c_0 s^2(\eta, \xi)}{2} \quad (\text{III .9})$$

where  $c_0$  represents the elastic stiffness of the pairwise bond and is constant, called "micro-modulus", which is similar to spring stiffness, and  $s(\eta, \xi)$  represents the normal deformation (stretch) of a bond

$$s = \frac{\|\eta + \xi\| - \|\xi\|}{\|\xi\|} \quad (\text{III .10})$$

After substituting from Eq. (III .9) into Eq. (III .7), the pairwise force function can be rewritten as

$$\mathbf{f}(\eta, \xi) = \begin{cases} \frac{\eta + \xi}{\|\eta + \xi\|} c_0 s(\eta, \xi) & \text{when } \|\xi\| \leq \delta \\ 0 & \text{else} \end{cases} \quad (\text{III .11})$$

In this study, we take a two-dimensional BBPD problem as an example to derive the expression of the micro-modulus  $c_0$ . In classical continuum mechanics, the strain energy density at point  $\mathbf{x}$  can be expressed as

$$W_{CM}(\mathbf{x}) = \frac{1}{2} \sigma^T \varepsilon \quad (\text{III .12})$$

where  $\sigma$  and  $\varepsilon$  represents the stress tensor and strain tensor respectively. For an elastic plane stress problem as shown in Fig.III .4, the strain tensor components are set as  $\varepsilon_x = \varepsilon_y = s, \gamma_{xy} = 0$ , then the stress tensor  $\sigma$  can be expressed as

$$\sigma = \begin{Bmatrix} \sigma_x \\ \sigma_y \\ \sigma_{xy} \end{Bmatrix} = \frac{E}{1-\nu^2} \begin{bmatrix} 1 & \nu & 0 \\ \nu & 1 & 0 \\ 0 & 0 & \frac{1-\nu}{2} \end{bmatrix} \begin{Bmatrix} \varepsilon_x \\ \varepsilon_y \\ \gamma_{xy} \end{Bmatrix} \quad (\text{III .13})$$

Where  $\sigma_x, \sigma_y, \sigma_{xy}$  represent the corresponding normal stress and shear stress components. And  $\nu$  is the Poisson's ration,  $E$  is the Young's modulus. Then the strain energy density at point  $\mathbf{x}$  can be rewritten as

$$W_{CM}(\mathbf{x}) = \frac{1}{2} \frac{E}{1-\nu^2} \begin{Bmatrix} \varepsilon_x \\ \varepsilon_y \\ \gamma_{xy} \end{Bmatrix}^T \begin{bmatrix} 1 & \nu & 0 \\ \nu & 1 & 0 \\ 0 & 0 & \frac{1-\nu}{2} \end{bmatrix} \begin{Bmatrix} \varepsilon_x \\ \varepsilon_y \\ \gamma_{xy} \end{Bmatrix} = \frac{E}{1-\nu} s^2 \quad (\text{III .14})$$

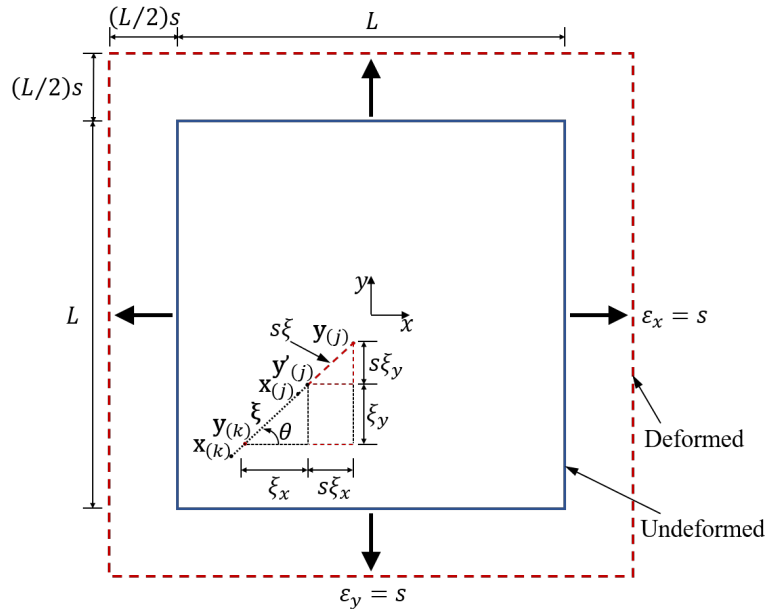


**Figure III .4:** A two-dimensional plate subjected to isotropic expansion

For the BBPD model, the strain energy density expression at point  $\mathbf{x}$  can be obtained

by combined Eq. (III .8) and Eq. (III .9)

$$W_{PD}(x) = \frac{1}{2}h \int_R \omega(\eta, \xi) dV_{x'} = \frac{1}{2}h \int_0^\delta \left(\frac{c_0 s^2 \xi}{2}\right) 2\pi \xi d\xi = \frac{\pi h c_0 s^2 \delta^3}{6} \quad (\text{III .15})$$

Where  $h$  is the thickness of structure model,  $V_{x'}$  is the volume of the point  $\mathbf{x}'$ ,  $\xi$  is the distance from material point  $\mathbf{x}'$  to  $\mathbf{x}$ , and  $\delta$  represents the size of the horizon.

Therefore, through Eq. (III .14) and Eq. (III .15), and the equivalent of the strain energy density,  $W_{PD}(x) = W_{CM}(x)$ , the micro-modulus in two-dimensional condition can be obtained as:

$$c_0 = \frac{6E}{\pi h \delta^3 (1 - \nu)} \quad (\text{III .16})$$

The same procedure can be performed for the problem with  $\varepsilon_x = -\varepsilon_y = s, \gamma_{xy} = 0$ , then the micro-modulus leads to

$$c_0 = \frac{12E}{\pi h \delta^3 (1 + \nu)} \quad (\text{III .17})$$

From Eq. (III .16) and Eq. (III .17), it can be concluded that in order to ensure the consistency of the micro-modulus, for the two-dimensional plane problem, the Poisson's ratio should be limited to 1/3. The same considerations for three-dimensional conditions, the Poisson's ratio should be limited to 1/4 (Gerstle et al., 2005; Huang et al., 2015a). Similar derivation process can be used to derive the micro-modulus under the three-dimensional condition, and finally get the expression of the micro-modulus for different dimensions

$$c_0 = \begin{cases} \frac{2E}{A\delta^2} & 1D \\ \frac{9E}{\pi h \delta^3} & 2D \text{ plane stress} \\ \frac{48E}{5\pi h \delta^3} & 2D \text{ plane strain} \\ \frac{12E}{\pi \delta^4} & 3D \end{cases} \quad (\text{III .18})$$

## 2.2 Generalized prototype microelastic brittle model (GPMB)

In the simulations of material fracture, the PMB model does not consider the influence of the distance between particles on the force (See Eq. (III .11)), but only the effect of bond stretch on force in the constitutive force function, which is inconsistent with the actual situation. The micro-modulus  $c$  get weaker when the bond length  $\xi = \|\xi\|$  increases, and its value become zero when the length of bond is equal to the horizon  $\delta$ . For heterogeneous and anisotropic materials, the force between particles even changes non-linearly. Many researches have been made to change the distribution of non-local interactions between

particles and other particles in the horizon by introducing different influence functions (kernel function)  $\kappa(\xi, \delta)$  on the basis of the PMB model (Butt et al., 2017; Ha and Bobaru, 2010; Huang et al., 2015a; Kilic, 2008; Seleson et al., 2011). These models are collectively referred to as the Generalized prototypic microelastic brittle model (GPMB).

The influence function  $\kappa(\xi, \delta)$  describes the spatial distribution of the intensity of long-range forces in materials, and it holds the following relations

$$\left\{ \begin{array}{l} \kappa(\xi, \delta) = \kappa(-\xi, \delta) \\ \lim_{\xi \rightarrow 0} \kappa(\xi, \delta) = \kappa_{max} \\ \lim_{\xi \rightarrow \delta} \kappa(\xi, \delta) = 0 \\ \int_{-\infty}^{\infty} \lim_{\xi \rightarrow 0} \kappa(\xi, \delta) = \int_{-\infty}^{\infty} \Delta(\xi) d\mathbf{x} = 1 \end{array} \right. \quad (\text{III .19})$$

According to the different shape of the influence function, it is mainly divided into the following three types, as shown in Fig.III .5. The cylindrical shape is the PMB model without considering the influence function.

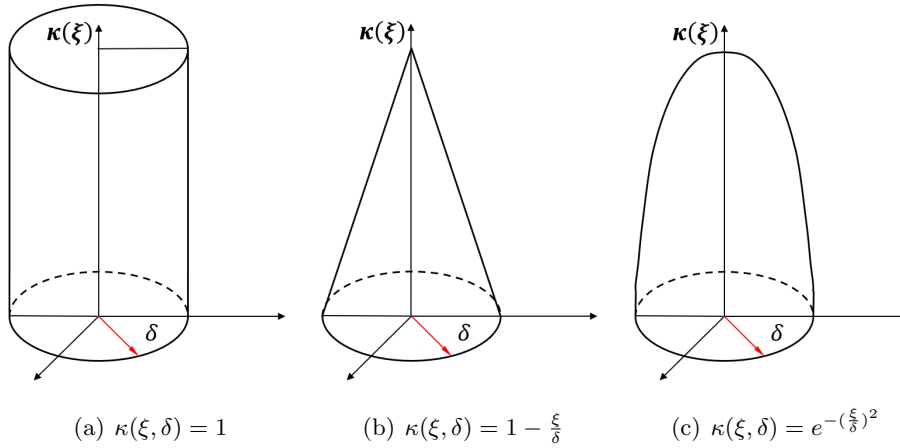


**Figure III .5:** Graphs of different influence functions  $\kappa(\xi, \delta)$

After introducing the influence function  $\kappa(\xi, \delta)$ , the the linear micro-elastic potential energy in Eq. (III .9) can be rewritten as

$$\omega(\eta, \xi) = \frac{c_0 s^2(\eta, \xi) \kappa(\xi, \delta) \xi}{2} \quad (\text{III .20})$$

So that the pairwise force function in Eq. (III .11) can be rewritten as

$$\mathbf{f}(\eta, \xi) = \begin{cases} \frac{\eta+\xi}{\|\eta+\xi\|} c_0 s(\eta, \xi) \kappa(\xi, \delta) & \text{when } \|\xi\| \leq \delta \\ 0 & \text{else} \end{cases} \quad (\text{III .21})$$

Then the micro-modulus in two-dimensional plane condition can be expressed as

$$c(\xi, \delta) = \frac{2E}{(1-\nu) \int_R \kappa(\xi, \delta) \xi dV_{x'}} \quad (\text{III .22})$$

In this paper, according to previous studies (Huang et al., 2015b; Sfer et al., 2002), the kernel function is chosen as

$$\kappa(\xi, \delta) = \begin{cases} (1 - (\frac{\xi}{\delta})^2)^2 & \xi \leq \delta \\ 0 & \xi > \delta \end{cases} \quad (\text{III .23})$$

The influence function is then represented graphically as shown in Fig.III .6

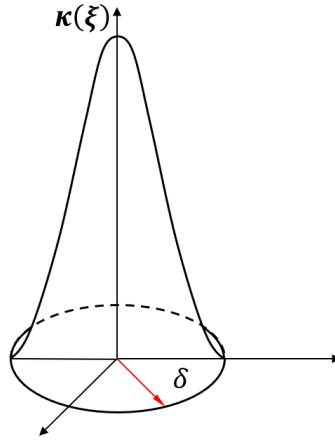


**Figure III .6:** Graphs of influence function for current study

Then the micro-modulus for different dimensions can be given by:

$$c(\xi, \delta) = \begin{cases} \frac{6E}{A\delta^2} \kappa(\xi, \delta) & 1D \\ \frac{315E}{8\pi h\delta^3} \kappa(\xi, \delta) & 2D \text{ plane stress} \\ \frac{42E}{\pi h\delta^3} \kappa(\xi, \delta) & 2D \text{ plane strain} \\ \frac{72E}{\pi\delta^4} \kappa(\xi, \delta) & 3D \end{cases} \quad (\text{III .24})$$

### 3 Numerical implementation

The bond-based peridynamics equation contains time and space integrals. Similar to molecular dynamics, after the model is discretized into particles, it is assumed that the movement of the particles obeys Newton's second law, and the time integration algorithm is used to further solve the integration of time for the parameters such as particle velocity, acceleration and displacement.

#### 3.1 Spatial discretization and correction

Similar with other numerical methods, the model structure needs to be discretized and defined before solving, such as method FEM. For the BBPD method, before solving the equation of motion, a numerical approximation method is usually used to discretize the model into a combination of particles with a specific volume. As shown in Fig.III .7, uniform discretization under different dimensions can be used according to calculation requirements. This article adopts the uniform discrete form, and the research of non-uniform discrete can refer to references (Bobaru and Ha, 2011; Ni et al., 2018).

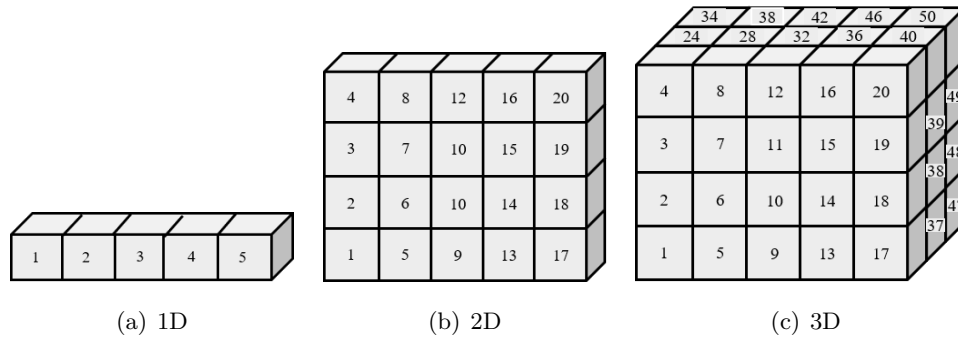


**Figure III .7:** Uniform discretization under different dimensions

Each elementary volume represents a mass particle localized by the coordinates of its center, as shown in Fig.III .8. The size of grid is denoted by  $\Delta x$ . Accordingly, the integral in Eq. (III .1) is transformed into a summation over all the bonds included in the horizon region of a particle (Silling, 2000). For instance, the discretized motion equation of the  $i^{th}$  particle at the  $n^{th}$  time step is written as:

$$\rho \ddot{\mathbf{u}}_i^n = \rho \ddot{\mathbf{u}}(\mathbf{x}_i, t^n) = \sum_{j=1}^{N_{H_{x_i}}} \mathbf{f}(\mathbf{u}_j^n - \mathbf{u}_i^n, \mathbf{x}_j^n - \mathbf{x}_i^n) V_j + \mathbf{b}_i^n \quad (\text{III .25})$$

$N_{H_{x_i}}$  is the total number of particles inside the horizon of the  $i^{th}$  particle.  $V_j$  denotes the volume of the  $j^{th}$  particle. In the 2D conditions, one has  $V_j = \Delta x^2 h$ . The choice

of horizon size  $\delta$  can have an important influence on numerical results and computing time. A common choice used in many PD simulations is  $3\Delta x$  (Silling, 2000). Values much smaller than this typically result in undesirable grid effects. Values much larger than this may result in excessive wave dispersion and require very large computing times. Thus, this choice is also adopted in this study. In practice, a value slightly larger, for instance,  $\delta = 3.015\Delta x$ , is used. This avoids that a floating point error causes certain pairs of particles inside a horizon to be debonded.

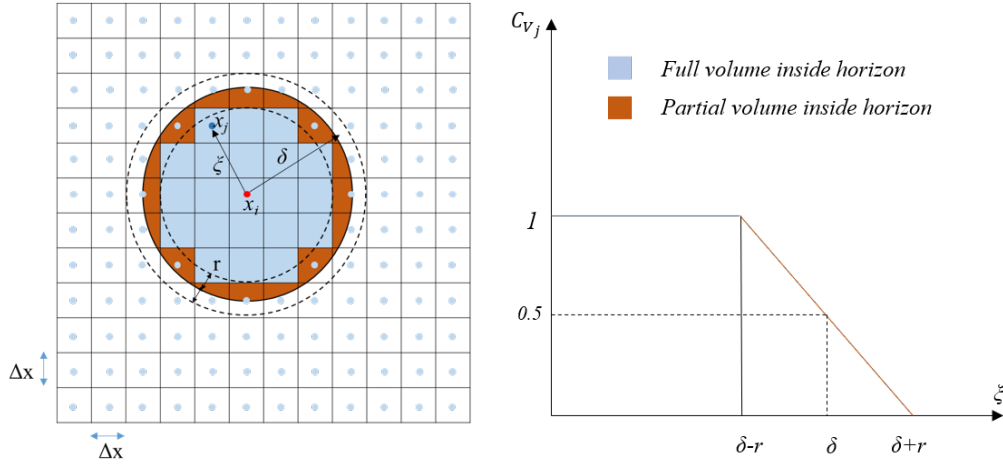


**Figure III .8:** Illustration of geometrical discretization and volume correction for the collocation points inside the horizon  $H_{x_i}$

Further, as shown in Fig. III .8, for the material particles located on the exterior boundary of a horizon zone  $H_{x_i}$ , their volume is partially involved inside the horizon. Therefore, it is needed to make a correction of volume  $V_j$  in the motion equation (III .25). This is done by introducing a volume correction coefficient  $C_{V_j}$ , which is defined by:

$$C_{V_j} = \begin{cases} 0 & \text{when } \|\boldsymbol{\eta} + \boldsymbol{\xi}\| \geq \delta \\ 1 & \text{when } \|\boldsymbol{\eta} + \boldsymbol{\xi}\| \leq (\delta - r) \\ \frac{\delta + r - \|\boldsymbol{\eta} + \boldsymbol{\xi}\|}{2r} & \text{when } (\delta - r) \leq \|\boldsymbol{\eta} + \boldsymbol{\xi}\| \leq \delta \end{cases} \quad (\text{III .26})$$

with  $r = \frac{\Delta x}{2}$ .

In the PD formulation presented above, it is assumed that all points inside the horizon of  $\mathbf{x}$  are localized in a single bulk material. However, near a surface, for instance, external boundaries or interface between two different materials as shown in Fig. III .9, material points do have a full neighboring or horizon region. Consequently, effective materials

properties near the surface of a PD model can be different with those in the real bulk medium. Therefore, a surface correction method is needed. Based on previous studies (Le and Bobaru, 2018; Madenci and Oterkus, 2014), an energy-based method is here adopted. For this purpose, a surface correction coefficient  $g$  is introduced for each of three axes of the coordinates frame. It is defined as the ratio of strain energy of real bulk material at the  $k^{th}$  point  $w_{cm_k}$  and that of the PD model  $w_{pd_k}$ :

$$g_k^\beta = \frac{w_{cm_k}^\beta}{w_{pd_k}^\beta}, (\beta = x, y, z) \quad (\text{III .27})$$

The surface correction coefficient of a bond linking the points  $i$  and  $j$  is calculated as the average of  $g_i^\beta$  and  $g_j^\beta$ :

$$g_{ij}^\beta = \frac{g_i^\beta + g_j^\beta}{2} \quad (\text{III .28})$$

Then, for a material bond oriented in an arbitrary orientation defined by the normal relative position vector between two points  $i$  and  $j$ ,  $\mathbf{n} = \frac{\mathbf{x}_j - \mathbf{x}_i}{|\mathbf{x}_j - \mathbf{x}_i|}$ , a global surface correction coefficient  $G_{ij}$  is defined by an ellipsoidal projection method and one gets:

$$G_{ij} = \frac{1}{\sqrt{\left(\frac{n_x}{g_{ij}^\beta}\right)^2 + \left(\frac{n_y}{g_{ij}^\beta}\right)^2 + \left(\frac{n_z}{g_{ij}^\beta}\right)^2}} \quad (\text{III .29})$$

Finally, by taking into account the volume and surface corrections, the motion equation (III .25) becomes:

$$\rho \ddot{\mathbf{u}}_i^n = \sum_{j=1}^{N_{H_{x_i}}} G_{ij} \mathbf{f}(\mathbf{u}_j^n - \mathbf{u}_i^n, \mathbf{x}_j^n - \mathbf{x}_i^n) C_{V_j} V_j + \mathbf{b}_i^n \quad (\text{III .30})$$

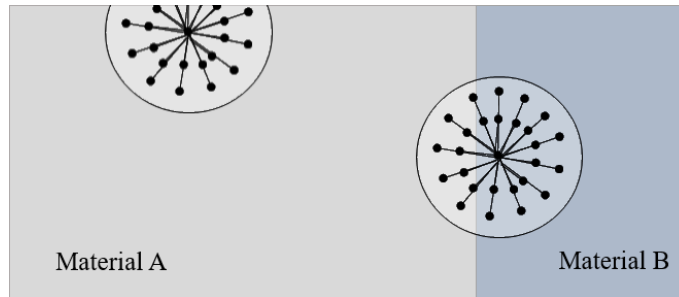


**Figure III .9:** Illustration of neighborhood of PD points near an interface

### 3.2 Time integration

After the geometrical discretization, it is needed to solve the system of discrete motion equations given in Eq. (III .30). Both static and dynamic problems can be solved in the



same framework. The time integration can be performed by using explicit forward and backward difference techniques (Silling et al., 2006). After solving the discrete equation of motion Eq. (III .30), the acceleration of the reference particle  $x$  at  $n^{th}$  time step,  $\ddot{\mathbf{u}}_x^n$  can be obtained, and then the velocity and displacement of point  $x$  at the next time step can be calculated by using explicit forward and backward difference techniques in two steps.

The first step determines the velocity at  $(n + 1)^{th}$  time step by using the acceleration and the known velocity at  $n^{th}$  time step

$$\dot{\mathbf{u}}_x^{n+1} = \ddot{\mathbf{u}}_x^n \Delta t + \dot{\mathbf{u}}_x^n \quad (\text{III .31})$$

The second step calculate the displacement at  $(n + 1)^{th}$  time step by using the velocity  $\dot{\mathbf{u}}_x^{n+1}$  calculated from Eq. (III .31) and the known displacement at  $n^{th}$  time step.

$$\mathbf{u}_x^{n+1} = \dot{\mathbf{u}}_x^{n+1} \Delta t + \mathbf{u}_x^n \quad (\text{III .32})$$

### 3.2.1 Numerical stability

Although the explicit time integration scheme is straightforward, it is only conditionally stable. Therefore, a stability condition is necessary to obtain convergent results (Silling and Askari, 2005). The standard von Neumann stability analysis can be performed by assuming as

$$\mathbf{u}_x^n = \zeta^n \exp(\varrho x \sqrt{-1}) \quad (\text{III .33})$$

where  $\varrho$  is a positive real number and  $\zeta$  is a complex number. To determine the value range of time step  $\Delta t$  is to determine the stability condition of the algorithm, that is, for  $\forall \varrho \in R$ ,  $|\zeta| \leq 1$  should be satisfied.

The equation of motion of the linearized Peridynamics model (refer to Eq. (III .30)) can be expressed as

$$\rho \ddot{\mathbf{u}}_i^n = \sum_j K(\mathbf{u}_j^n - \mathbf{u}_i^n)(\mathbf{x}_j^n - \mathbf{x}_i^n) V_0 + \mathbf{b}_i^n \quad (\text{III .34})$$

where  $K$  represents all constant coefficients in the equation of motion,  $V_0$  represents the volume of the element in discretization. Suppose  $\chi = j - i$ ,  $K_\chi = K(\mathbf{x}_j^n - \mathbf{x}_i^n)$ , substituting Eq. (III .31) to Eq. (III .33) into Eq. (III .34), we have

$$\frac{\rho}{\Delta t^2} (\zeta - 2 + \zeta^{-1}) = \sum_{\chi=-\infty}^{\infty} K_\chi (\exp(\varrho \chi \sqrt{-1}) - 1) V_0 = \sum_{\chi=1}^{\infty} 2K_\chi (\cos \varrho \chi - 1) V_0 \quad (\text{III .35})$$

Since the micro-modulus function is an even function, so write  $M_\varrho = \sum_{\chi=1}^{\infty} 2K_\chi (\cos \varrho \chi - 1) V_0$ , and by solving the this formula, we have

$$\zeta = 1 - \frac{M_\varrho \Delta t^2}{\rho} \pm \sqrt{\left(1 - \frac{M_\varrho \Delta t^2}{\rho}\right)^2 - 1} \quad (\text{III .36})$$

To satisfy  $\forall \varrho \in R, |\zeta| \leq 1$ , we have

$$\Delta t < \sqrt{\frac{2\rho}{M_\varrho}}, \quad \forall \varrho \quad (\text{III .37})$$

To ensure that the above equation is applicable to all  $\varrho$ ,  $M_\varrho$  should satisfy

$$M_\varrho \leq 2V_0 \sum_{\chi=1}^{\infty} K_\chi \quad (\text{III .38})$$

So

$$\Delta t < \sqrt{\frac{\rho}{V_0} \sum_{\chi=1}^{\infty} K_\chi} \quad (\text{III .39})$$

### 3.2.2 Adaptive Dynamic Relaxation (ADR)

When solving static problems such as shrinkage induced cracking, a specific numerical algorithm is necessary to approximate the dynamic motion as a quasi-static process. Usually, the target time period is divided into a finite number of intervals (or steps). The time step should be small enough to ensure numerical stability. This can lead to a high computing cost when the number of material points is important. In this study, an adaptive dynamic relaxation method initially proposed in (Madenci and Oterkus, 2014; Underwood, 1986) is adopted to reduce the calculation time for static problems. At the  $n^{\text{th}}$  time step, the motion equations Eq. (III .30) for all material points are assembled and transformed into a series of ordinary differential equations by introducing a fictitious density matrix  $\mathbf{M}$  and damping terms  $d_c$ :

$$\mathbf{M}\ddot{\mathbf{U}}^n(\mathbf{X}, t) + d_c^n \mathbf{M}\dot{\mathbf{U}}^n(\mathbf{X}, t) = \mathbf{F}^n(\mathbf{U}, \mathbf{X}) \quad (\text{III .40})$$

The vectors  $\mathbf{X}$  and  $\mathbf{U}$  contain the initial positions and displacements of all materials points, respectively. The vector  $\mathbf{F}$  includes the interactions and body forces of all material points, and its  $i^{\text{th}}$  component can be expressed as:

$$\mathbf{F}_i = \sum_{j=1}^{N_{Hx_i}} G_{ij} \mathbf{f}(\mathbf{u}_j - \mathbf{u}_i, \mathbf{x}_j - \mathbf{x}_i) C_{V_j} V_j + \mathbf{b}_i \quad (\text{III .41})$$

The fictitious density matrix  $\mathbf{M}$  is a diagonal one, with the entries on the main diagonal as follows:

$$M_{ii} = \frac{\pi \delta^2 h c_{max} \Delta t^2}{4 \Delta x} \quad (\text{III .42})$$

where  $c_{max}$  is the maximum value of the microscopic elastic stiffness of bonds given in Eq. (III .24).

The damping coefficient  $d_c^n$  can be determined by using the lowest frequency of the system (Underwood, 1986), which is given as:

$$d_c^n = 2\sqrt{\frac{(\mathbf{U}^n)^T K^n \mathbf{U}^n}{(\mathbf{U}^n)^T \mathbf{U}^n}} \quad (\text{III .43})$$

where  $K^n$  is the diagonal "local" stiffness matrix, with the main diagonal written as

$$K_{ii}^n = \frac{\mathbf{F}_i^n - \mathbf{F}_i^{n-1}}{M_{ii} \Delta t u_i^{t-1/2}} \quad (\text{III .44})$$

According to the central-difference explicit integration scheme, the velocities for  $n^{\text{th}}$  time step are expressed as:

$$\dot{\mathbf{U}}^n = \dot{\mathbf{U}}^{n-\frac{1}{2}} + \frac{1}{2} \ddot{\mathbf{U}}^n \Delta t \quad (\text{III .45})$$

Combining with Eq. (III .40), the displacements and velocities for the next time step are given by:

$$\dot{\mathbf{U}}^{n+\frac{1}{2}} = \frac{(2 - d_c^n \Delta t) \dot{\mathbf{U}}^{n-\frac{1}{2}} + 2\mathbf{M}^{-1} \mathbf{F}^n \Delta t}{2 + d_c^n \Delta t} \quad (\text{III .46})$$

and

$$\mathbf{U}^{n+1} = \mathbf{U}^n + \dot{\mathbf{U}}^{n+\frac{1}{2}} \Delta t \quad (\text{III .47})$$

By assuming that  $\mathbf{U}^0 \neq 0$  and  $\dot{\mathbf{U}}^{-1/2} = 0$ , the integration is started by

$$\dot{\mathbf{U}}^{\frac{1}{2}} = \frac{\mathbf{M}^{-1} \mathbf{F}^0 \Delta t}{2} \quad (\text{III .48})$$

where  $\Delta t$  is the time step. It is interesting to note that the only physical term in this dynamic relaxation method is the force vector  $\mathbf{F}$ . On contrary, the fictitious density matrix  $\mathbf{M}$ , damping coefficient  $d_c$ , and time step size  $\Delta t$ , do not have to be physical quantities. Thus, their values can be chosen a priori in order to obtain fast convergence, for instance, a time step size of  $\Delta t = 1$  is a common choice (Madenci and Oterkus, 2014).

## 4 Numerical simulations

### 4.1 Bar under tension

In the Peridynamics theory, the selection of parameters (such as the density of particles within the horizon  $m$  (ratio between the horizon and the 'volume' of a point material), the spacing between material points (grid size)  $\Delta x$ , and the horizon size  $\delta$ , etc.) has an important influence on the computational process. It is important to determine the optimum values of these parameters in order to achieve high accuracy with sufficiently small amount of computational time.

A uniform and isotropic concrete bar with length  $L = 1m$  subjected to a quasi-static tension is considered, to analyze the influence of the selection of parameters  $\Delta x$  and  $\delta$  on the simulation results. As shown in Fig., the bar is clamped at the left end and subjected to the tension loading of  $F = 20N$ . The concrete parameters are chosen as Young's modulus  $E = 20GPa$  and  $\rho = 2400kg/m^3$ . And the ADR method is used with  $\Delta t = 1$  and time steps  $n_t = 100000$ .

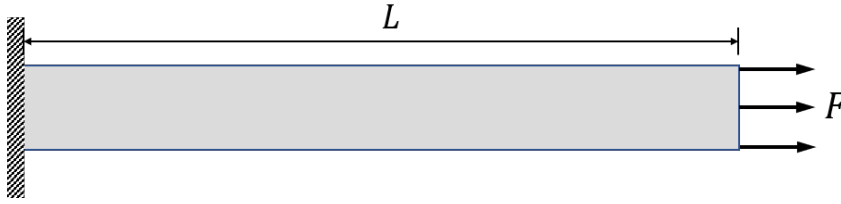


**Figure III .10:** Geometry of a bar under tension

The influence of the density of particles within the horizon  $m$  on the numerical simulation is firstly studied. Keep the horizon size  $\delta = 0.01m$  unchanged, and choose  $m = 1, 2, 3, 4$ . As observed in Fig.III .11, the displacement of the material point near the middle of the bar for different  $m$  reaches a stable convergence value after about 4000 time steps. Therefore, after the calculation, the displacement of the material point on the bar can be compared with the analytical solution which is expressed as

$$u_x = \frac{F}{AE}x = 0.001x \quad (\text{III .49})$$

It can also be observed from Fig.III .11 that the smaller the value of  $m$ , the faster the computation reaches stability, i.e., the more efficient the computation is. In order to present the difference of the results with different values of  $m$  more clearly, the displacements of the points located at  $0.15m$  to  $0.2m$  of the bar are shown in Fig.III .12, and the variations of the mean value of the difference in displacement of the bar for different values of  $m$  is shown in Fig.III .13. It can be observed that while keeping other parameters unchanged, the error between the PD solution and the analytical solution decreases as the value of  $m$  increases, which shows that the larger the particle density in the horizon, the higher the accuracy of the calculation result.

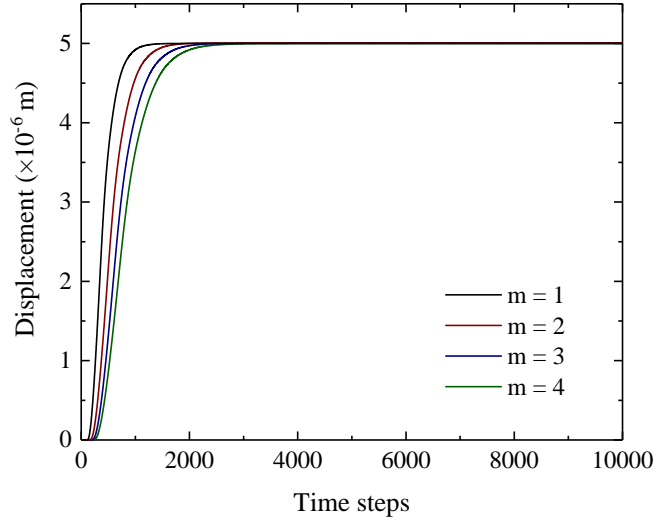


**Figure III .11:** Displacement of the material point near the middle of the bar as time step increases for different  $m$

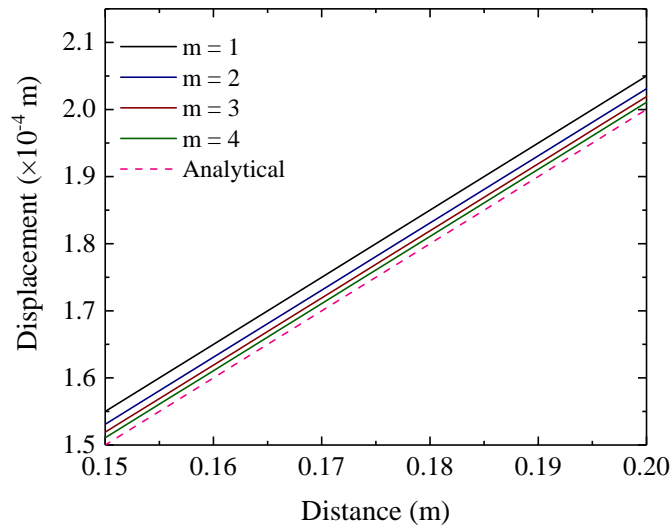


**Figure III .12:** Displacement variations comparison of peridynamics solutions with different  $m$  and analytical solution along the location  $0.1m$  to  $0.2m$  of the bar

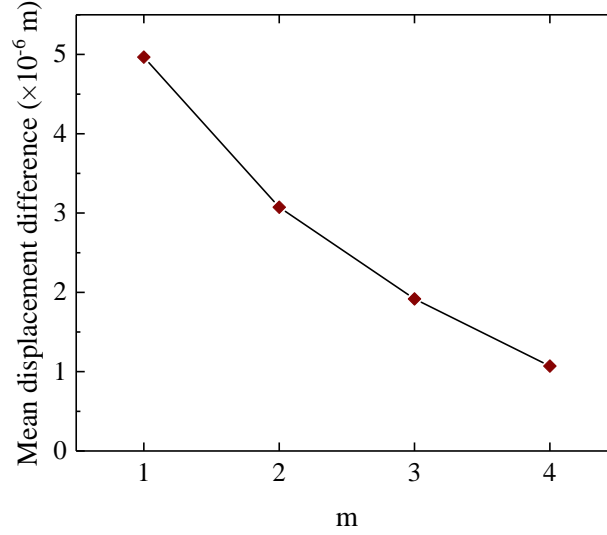


**Figure III .13:** Variation of the mean value of the difference in displacement of the bar for different values of  $m$

Then the influence of the grid size  $\Delta x$  is studied. Choose  $\Delta x = 0.0001m, 0.001m, 0.01m, 0.1m$  with constant  $m = 3$ . Fig.III .14 shows that the time steps required to reach a stable convergence value decreases as the value of  $\Delta x$  increases. The results compared with the analytical solution is shown in Fig.III .15 and Fig.III .16. We can observed from the figure that with other parameters unchanging, the error between the PD solution and the analytical solution decreases as the value of  $\Delta x$  decreases, which shows that the smaller the particle distance, the higher the accuracy of the calculation result.

Finally, the influence of the horizon size  $\delta$  on the simulation is studied. Keep the particle spacing  $\Delta x = 0.001m$ , select  $\delta = \Delta x, 2\Delta x, 3\Delta x, 4\Delta x$ . The Fig.III .17 shows that the computational time decreases as the value of  $\delta$  increases. The comparison between the simulation results and the analytical solution is shown in Fig.III .18 and Fig.III .19. It can be observed that the highest accuracy is achieved for the horizon size of  $\delta = 2\Delta x$ . Considering the small difference in calculation accuracy between  $\delta = 2\Delta x$  and  $\delta = 3\Delta x$  and in the interest of computational efficiency,  $\delta = 3\Delta x$  is commonly used in PD simulation. In this paper, we use  $\delta = 3.015\Delta x$  which is slightly greater than  $3\Delta x$  to avoid the floating point error which can induce three mesh spacing between certain pairs of elements, which are fail to be bonded.

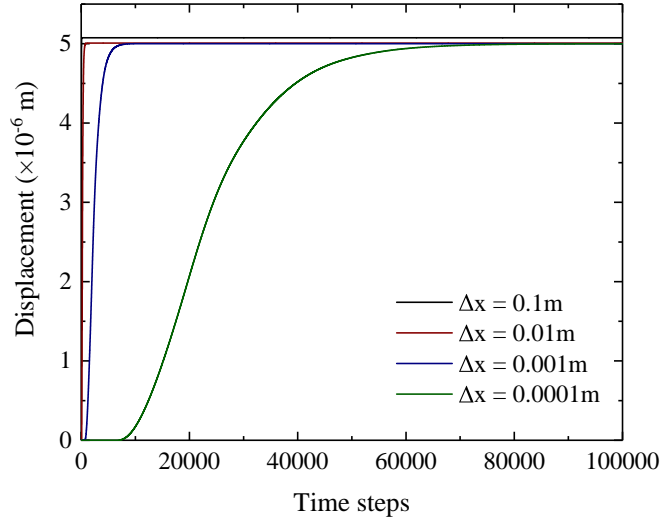


**Figure III .14:** Displacement of the material point near the middle of the bar as time step increases for different  $\Delta x$

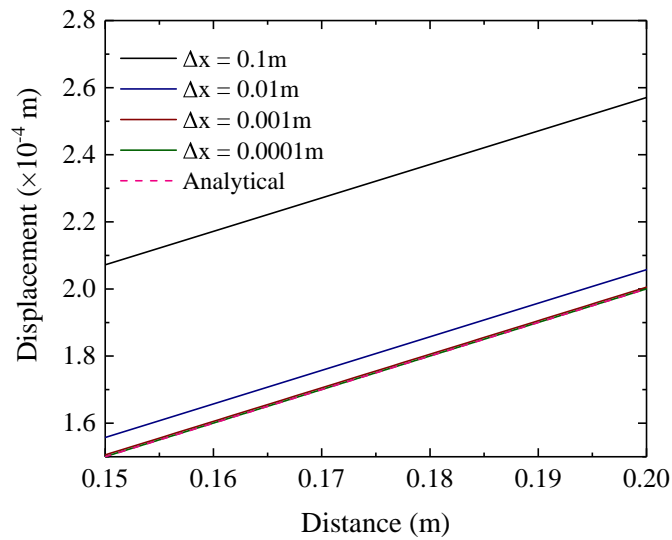


**Figure III .15:** Displacement variations comparison of peridynamics solutions with different  $\Delta x$  and analytical solution along the location  $0.15m$  to  $0.2m$  of the bar

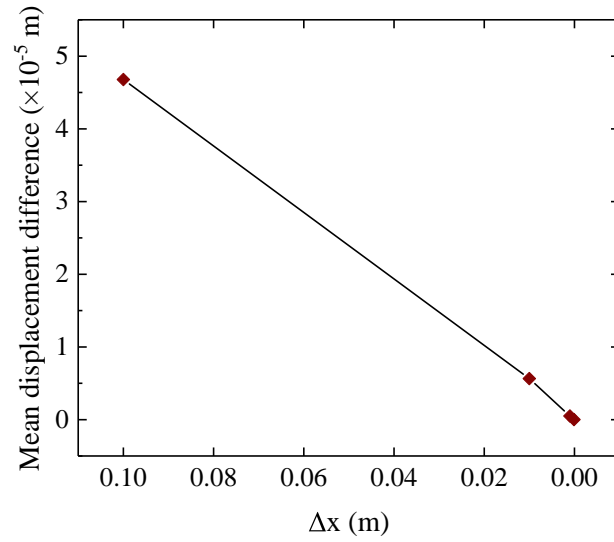


**Figure III .16:** Variation of the mean value of the difference in displacement of the bar for different values of  $\Delta x$

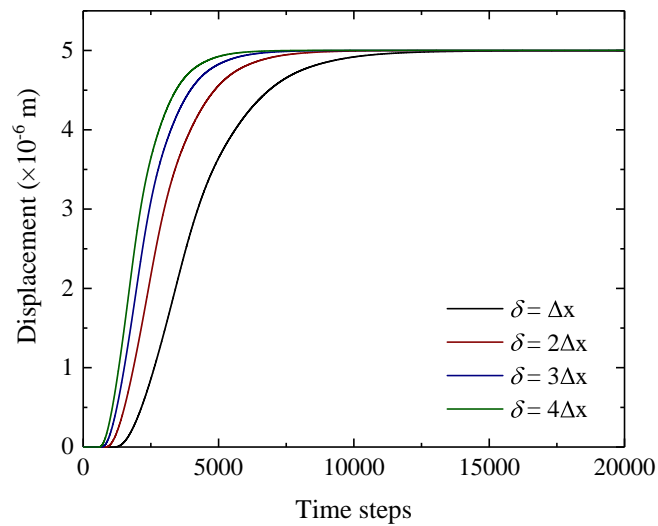


**Figure III .17:** Displacement of the material point near the middle of the bar as time step increases for different  $\delta$



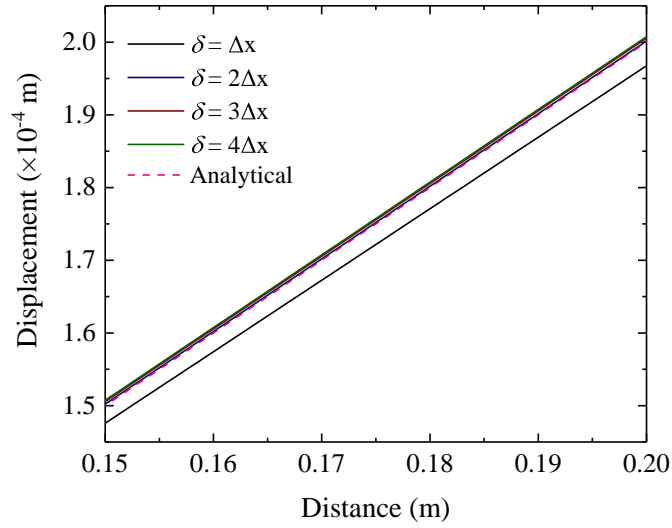


**Figure III .18:** Displacement variations comparison of peridynamics solutions with different  $\delta$  and analytical solution along the location  $0.15m$  to  $0.2m$  of the bar

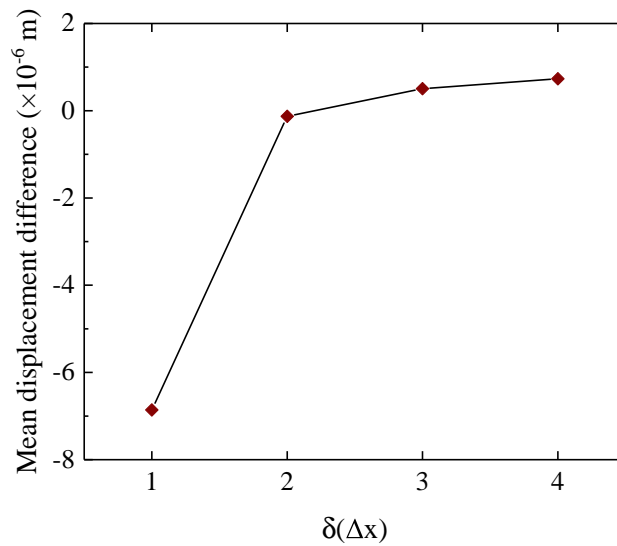


**Figure III .19:** Variation of the mean value of the difference in displacement of the bar for different values of  $\delta$

## 4.2 Cantilever beam under transverse loading

In this section, to verify the quantitative accuracy of the improved bond-based PD model for the computational prediction of elastic behavior and to demonstrate its applicability in simulating the entire mechanical response during elastic deformation. A typical and commonly used 2D cantilever beam engineering model with a length of  $1.0m$  and a width of  $0.25m$  is established as shown in Fig.III .20.

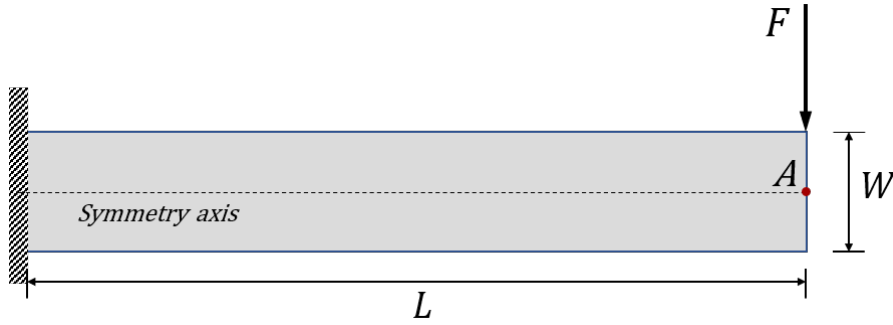


**Figure III .20:** Geometry of cantilever beam under transverse loading

The beam is subjected to an uniform load  $F$  at the free end. In the numerical model the uniformly discrete and fixed particle spacing  $\Delta x = 0.01m$  is used in the analysis, so the model is divided into  $100 \times 25 = 2500$  particle points. Horizon sizes  $\delta$  are selected as  $2.015\Delta x$ ,  $3.015\Delta x$ ,  $4.015\Delta x$ , and  $5.015\Delta x$ , respectively. In order to develop a model similar to typical concrete materials, Young's modulus  $E = 28GPa$ , density  $\rho = 2500kg/m^3$  were chosen, except that the Poisson's ratio for the planar stress problem was limited to  $1/3$  in the bond-based PD framework. And the ADR method is used for the time integration. Considering the shear deformation of the cantilever beam, the vertical displacement of point  $A$  in Fig.III .20 can be calculated by the following equation:

$$u_{A,y} = \mathbf{F}\left(\frac{L^3}{3EI} + \frac{L}{kGA}\right) \quad (\text{III .50})$$

where  $EI$  and  $GA$  are the bending and shear stiffness of the beam, respectively, and  $k = 5/6$  is the shear correction factor.

Fig. III .21 shows the comparison between the analytical solution of the relation of the load-displacements at the right end point  $A$  of the cantilever beam and the solution of the peridynamics method using different horizon size  $\delta$ . It can be seen from the figure that the results obtained in the bond based PD model are in good agreement with the analytical solution. Comparing the peridynamics solutions with different horizon size  $\delta$ , the horizon size  $\delta = 3.015\Delta x$  can predict the deformation of the concrete structure well.

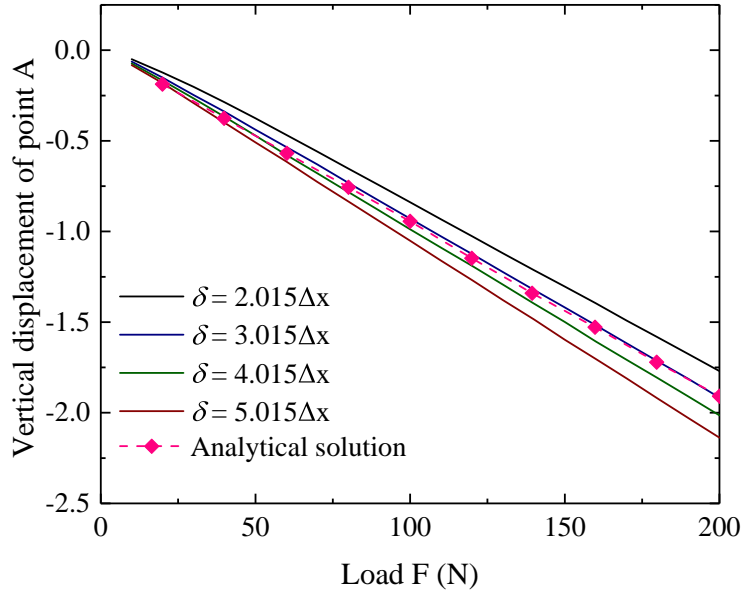


Figure III .21: Load–displacement curves by using various  $\delta$

## 5 Concluding remarks

In this chapter, the theoretical foundations of the peridynamics method are firstly introduced, including the principles and fundamental equations of motion, etc. Then the two important branches of the peridynamics theory, namely, bond-based and state-based, are outlined. The commonly used bond-based peridynamics models are classified into the prototype microelastic brittle model (PMB) and the generalized prototype microelastic brittle model (GPMB) according to the different influence functions. Afterwards, the effects of the factors on the calculation accuracy and efficiency are evaluated by parametric simulations with horizon particle density, grid size, and horizon size, providing a theoretical basis for the selection of parameters and program design in the following chapters. Finally, the numerical simulation of the classical problem of bending a two-dimensional concrete cantilever beam is performed and the capability of the bond-based PD model to the macroscopic concrete problem is demonstrated.



## Chapter IV

# An Improved Bond-based Peridynamics Model for Heterogeneous Concrete Materials

### 1 Introduction

Concrete materials are widely used in various engineering structures. The durability of concrete structures is mainly controlled by the initiation and propagation of cracks. In most situations, those structures are subjected to multi-physical processes including mechanical loads, hydraulic flow and moisture change, heat transfer and temperature variation, as well as chemical degradation. Moreover, concrete materials are heterogeneous composites with the presence of cement paste, aggregates and pores. Their mechanical behavior is intimately related to the multiple mechanisms occurring at different length scales, from macro, meso to microscale and even atomic or sub-atomic scales. Therefore, the multi-scale experiments and simulations of concrete have become a hot research area, providing more accurate insights into the mechanical behavior of concrete materials and structures ([Havlásek and Jirásek, 2016](#); [Li et al., 2020](#); [Rodrigues et al., 2020](#); [Tal and Fish, 2018](#)). For instance, subjected to drying-wetting process, non-uniform strain fields are induced due to the difference of shrinkage deformation between aggregates and cement paste. As a consequence, cracks are initiated around interfaces between aggregates and cement paste ([Bisschop and Van Mier, 2002a](#); [Samouh et al., 2018](#)). The induced cracking can strongly affect the integrity of thermal-hydro-mechanical properties of materials, such as the decrease of elastic stiffness and failure strength ([Burlion et al., 2005](#); [Yurtdas et al., 2011](#)), and the increase of permeability and thermal conductivity ([Chen et al., 2010](#); [Grassl](#)

et al., 2010). The final failure of structures is generally caused by the coalescence of micro-crack into macroscopic cracks or fractures. On the other hand, according to a number of previous studies (Grassl et al., 2010; Idiart et al., 2012), the initiation and propagation of cracks of concrete composites are clearly driven by the volume fraction, geometrical size and shape and mechanical properties of aggregates (or inclusions). Therefore, it is an important issue to develop efficient numerical methods for the description of full cracking process by taking into account influences of materials heterogeneity.

The theory of bond-based peridynamics was proposed early (Silling, 2000) and is widely used in the study of fracture damage of various solid materials, including geotechnical materials, fiber composites, functional gradient materials and so on (Hu et al., 2012; Ni et al., 2018; Wang et al., 2018; Zhou et al., 2020), and less concerning concrete materials. In this chapter, the damage is introduced into the PD model under the basic theory of the previous chapter, and the accuracy and effectiveness of this model in simulating and analyzing the mechanical properties of concrete is verified through the comparison of the existing experimental and simulation results. Numerical simulations based on experimental results are then performed to analyze the effect of inclusions stiffness on the process of cracking due to dry shrinkage and temperature variations.

## 2 Mesoscale Modeling of concrete

In mesoscale studies of concrete, it is generally considered that concrete consists of three phases (Grassl et al., 2012; Li et al., 2016) with cementitious matrix, coarse aggregates and interfacial transition zone (ITZ) or four phases plus pores (Wang et al., 2015; Yaghoobi et al., 2017). The macroscopic mechanical properties of concrete are affected by concrete gradation, porosity and aggregate content. Establishing a mesoscopic model reflecting the inhomogeneity of concrete structures can effectively consider the differences in mechanical parameters of various materials in concrete and the diversity of mechanical properties of concrete structures, and better characterize the fracture behavior of concrete.

### 2.1 Mesoscopic constituents

Concrete is a heterogeneous material consisting of cement, sand (fine aggregate), stone (coarse aggregate), water (often mixed with appropriate admixtures and additives) and other materials mixed in a certain proportion. The macroscopic mechanical properties of concrete are a reflection of its microscopic, mesoscopic composition and structure. As illustrated in Fig. IV .1, at the mesoscopic level, concrete materials can be divided into

four phases, that is, coarse aggregates, cementitious matrix, and the interface transition between them and pores.

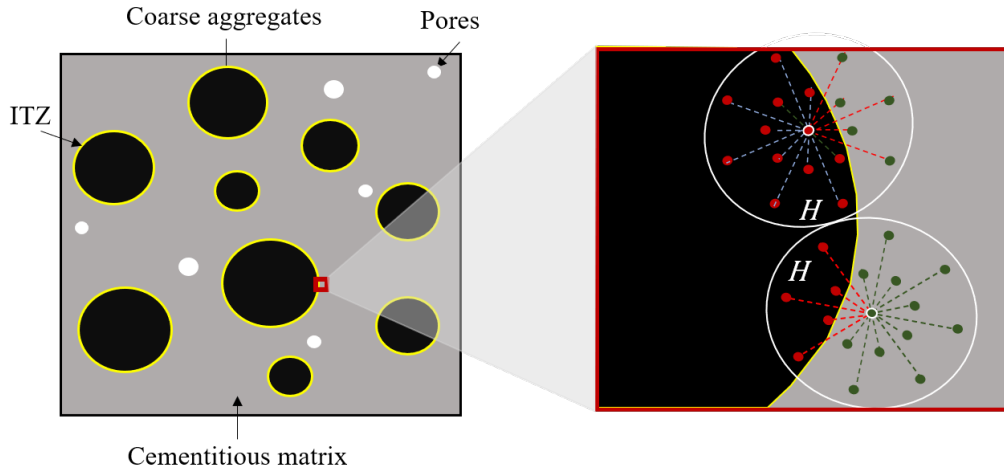


**Figure IV .1:** Multiphase composition of concrete at the mesoscale

**Cementitious matrix:** The cementitious matrix can be regarded as a composite material consisting of a hardened cement paste, sands and the interface between them. Similarly with concrete, the performance of the matrix mainly depends on the cement used in the concrete, the compaction and furthermore on the quantity of pores, the water-cement ratio and the environmental conditions (e.g. temperature, humidity) during the solidification procedure (Kumar and Bhattacharjee, 2003; Unger and Eckardt, 2011). In the mesoscale numerical simulations, the cementitious matrix is considered as a homogeneous phase.

**Coarse aggregates:** The volume of coarse aggregate in concrete constitutes a large part of the total volume of concrete (the coarse aggregate content in normal concrete is typically 30% to 40%, while in some other concrete, such as that used in dams, it is 60% to 70% (Wriggers and Moftah, 2006)), so the mechanical properties of concrete are strongly influenced by the coarse aggregate (type, shape, distribution, gradation, etc.). For example, the presence of coarse aggregate results in a concentration of stresses within the concrete under loading, but since the strength of coarse aggregate is usually high, it can act as a constraint on the development of cracks. Increasing the strength of coarse aggregates can improve the fracture energy of concrete to some extent.

Depending on the type of aggregate and the manufacturing process, the aggregate can have different shapes and be crushed (split, crushed fines) and uncrushed (gravel, sand), and in the numerical simulations in this paper, the aggregate is assumed to be

circular for the 2D simulations and spherical for the 3D simulations and linearly elastic and unfractured. Simulations with other shapes of aggregates and fractured aggregates have also been studied and can be found in (Liu et al., 2014; Wang et al., 2016, 1999).

**Interfacial transition zone (ITZ):** The transition zone between the aggregate and the cement paste is a thin layer that surrounds the aggregate particles. During concrete blending, some of the water is enriched near the coarse aggregate, forming water vesicles that result in a weaker bond between the cement paste and the aggregate. At the same time, due to the existence of "wall effect" (Diamond, 1986), the water is enriched in the surface area of the aggregate, leading to the actual water-cement ratio of the cement paste around the aggregate is greater than that in the matrix, which forms a more sparsely structured area. Due to the low strength of the interfacial transition zone, concrete failure under loading often begins from this region.

In the simulation using the PD method, the structure is discretized into a large number of material points occupying a certain volume, and "bonds" are generated according to the horizon zone. Due to the thin thickness of the interface between aggregates and cement matrix, generally in the range of 9 to  $51\mu m$  (Garboczi and Bentz, 1991; Scrivener et al., 2004; Zheng et al., 2005), which is much smaller than or close to the distance between the material points. Therefore in this paper, the material points are not arranged at the interface, but only within the aggregate and cement matrix. Thus, the model contains a total of two types of material points, with three types of bonds, respectively, the aggregate bonds, the cement matrix bonds and the interface bonds (Fig. IV .1), they have different mechanical properties as a way to reflect the heterogeneity of the concrete.

**Pores:** Mesoscopic pores are distributed throughout the cement paste and may reduce the compressive strength of the concrete. In the numerical simulation, pores with a diameter of 2 – 4mm are placed.

## 2.2 Modeling methods

There are essentially two type methods for generating meso-scale models of concrete: the digital image-based modeling methods and the parameterization modelling methods.

In the former, cameras, microscopes, or more advanced 3D techniques (e.g., nuclear magnetic resonance spectroscopy (NMR) and X-ray computed tomography (XCMT) scanners) are used to capture digital images of mesoscopic structures. The images are then converted into finite element (FE) meshes that model multi phases with actual size, shape, and distribution (Huang et al., 2015c; Kamel et al., 2020, 2019; Nguyen et al., 2018; Ren et al., 2018). Image-based modelling is a true reflection of the mesoscale structure of ma-



terials and hence shows great potential. However, the application is not always practical, and performing 3D tests is expensive and time-consuming, even more in situations where a large number of samples are often required for meaningful statistical analysis. In addition, image processing and meshing of complex mesoscale structures is not an easy task.

Heterogeneity can also be generated analytically using parameterization modeling methods, where two modeling approaches exist: implicitly creating random fields that satisfy some correlation function and by explicitly modeling different phases. In the implicit approach, the non-homogeneous material properties are modeled as spatially varying random fields assigned to a regular finite element mesh (Yang and Xu, 2008), or by randomly assigning lattice elements to aggregates and cement paste phases in the lattices model (Jivkov et al., 2013). This method can easily generate a large number of samples and is therefore very promising for global statistical analysis. In the latter explicit approach, aggregates of different shapes and sizes are directly generated, randomly filled into a domain, and mixed with cement paste to form digital concrete specimens (Du et al., 2013; Sheng et al., 2016; Wang et al., 1999). This approach allows the algorithm to take into consideration key multiphase parameters such as shape and size, asymptotic and spatial distribution of pores and aggregates, phase volume fraction and aggregate-mortar interface and their influence on the mechanical properties of the sample. This makes explicit approaches to mesoscale modeling attractive, especially when an accurate understanding of detailed failure mechanisms is required.

A number of significant advances have been achieved in the last few decades concerning the generation of mesoscopic structures, the main method is to automatically generate random geometric configurations of aggregate particles based on the basic statistical characteristics of the mesoscopic components (Häfner et al., 2006). For instance, the random aggregate model labeled as a take-and-place method (Wang et al., 2015, 1999) was followed by an extension of the 2D model to a 3D model by Wriggers et al. (Wriggers and Moftah, 2006). Bazant et al. (Bazant et al., 1990) Schlangen and van Mier (Schlangen and Van Mier, 1992) assumed that the aggregated particles have a spherical shape. Xu et al. (Xu and Chen, 2016) generated more realistic 3D fine-scale structures in which aggregates with different shapes, high volume content and a realistic size distribution were modeled.

### 3 Damage prediction

In the theory of BBPD, the interaction between the material points in the reference configuration of the object is actually transferred through the "bonds", and the magnitude

of the interaction force function is proportional to the relative displacement (Stretch  $s$ ) of the material points. Material damage in peridynamics is introduced through elimination of interactions (micro-potentials) among the material points. When the bond's stretch  $s$  exceeds a critical value  $s_0$ , it is assumed that the solid interaction breaks irreversibly, as shown in Fig.IV .2. As a result, the load is redistributed among the material points in the body, leading to progressive damage growth in an autonomous fashion (see Fig.IV .3). And when a crack occurs, all the bonds of the material points across the crack will be broken, and there is no interaction between the material points on both sides of the crack.

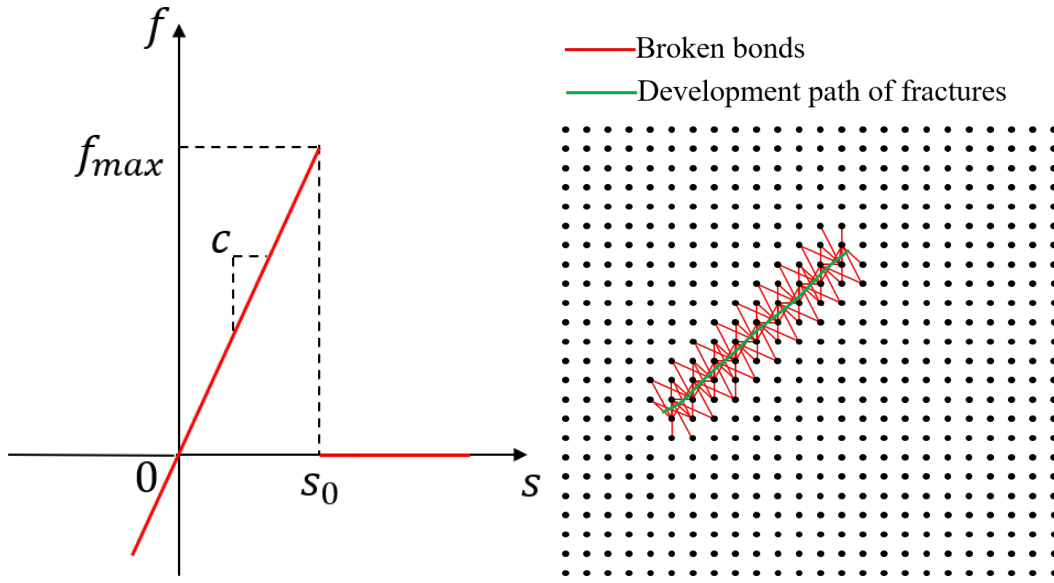


Figure IV .2: Linear damage model

Figure IV .3: Crack initiation and propagation

The criterion is numerically implemented by using the history-dependent scalar-valued function  $\mu(\xi, \mathbf{x}, t)$  in the PD constitutive model.

$$\mu(\xi, \mathbf{x}, t) = \begin{cases} 1 & \text{when } s \leq s_0 \\ 0 & \text{when } s > s_0 \end{cases} \quad (\text{IV .1})$$

where  $s_0$  is the critical stretch of bonds. It is related to the macroscopic fracture energy  $G_0$  which can be identified experimentally. Then the force function can be expressed as

$$\mathbf{f}(\eta, \xi) = \frac{\eta + \xi}{\|\eta + \xi\|} sc(\xi, \delta) \mu(\xi, \mathbf{x}, t) \quad (\text{IV .2})$$

According to the criterion for the bonds rupture, the materiel failure can be modeled by a scalar field called "damage". It is defined by the fraction of broken bonds in a materiel point's horizon. So the local damage at the  $\mathbf{x}$  point is presented as (Silling and Askari, 2005):

$$\psi(\mathbf{x}, t) = 1 - \frac{\int_{H_x} \mu(\xi, \mathbf{x}, t) dV_{x'}}{\int_{H_x} dV_{x'}} \quad (\text{IV .3})$$

Where  $V_{x'}$  is the volume of point  $\mathbf{x}'$ .

For the problem in plane stress condition, the energy  $G_0$  required for breaking all the bonds per unit can be obtained by (Ha and Bobaru, 2010; Madenci and Oterkus, 2014; Silling and Askari, 2005)

$$G_0 = 2h \int_0^\delta \int_z^\delta \int_0^{\cos^{-1}(z/\xi)} (c(\xi, \delta) s_0^2 \xi / 2) \xi d\theta d\xi dz \quad (\text{IV .4})$$

As shown in Fig.IV .4,  $z$  represents the vertical distance between the material point  $\mathbf{x}$  and the crack surface,  $\theta$  represents the rotation angle. Substitute Eq.(III .23) and Eq.(III .24) into Eq.(IV .4), and after some simplifications, we can obtain

$$G_0 \approx \frac{8E\delta s_0^2}{5\pi} \quad (\text{IV .5})$$

So the  $s_0$  under plane stress condition can be expressed as

$$s_0 = \sqrt{\frac{5\pi G_0}{8E\delta}} \quad (\text{IV .6})$$

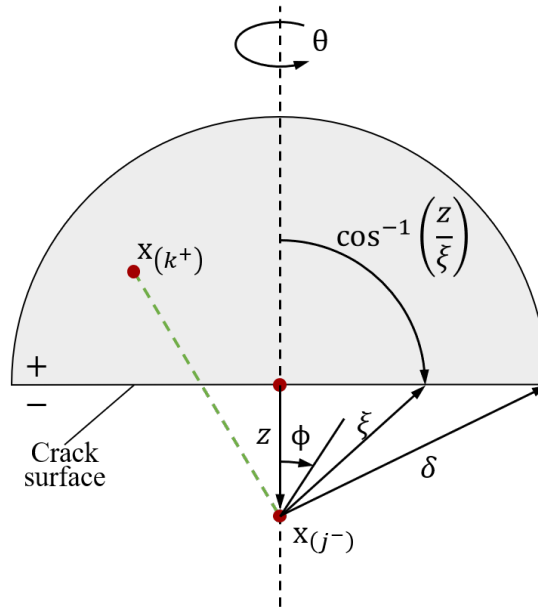


**Figure IV .4:** Integration domain of micro-potentials crossing a crack surface

## 4 Numerical simulations

### 4.1 Validation of the numerical implementation

The efficiency of the PD model is here verified through the simulation of a tension test on heterogeneous concrete sample. Numerical results obtained by the PD model are compared with experimental data reported in Hordijk (Hordijk, 1992) and those issued from finite element simulations (Wang et al., 2015).

In Fig. IV .5, one shows the geometrical size and boundary conditions of a tension test on a two-dimensional concrete plate. In this test, the left boundary surface is fixed and the displacement is uniformly prescribed on the right boundary surface and progressively increased to  $u = 0.1mm$ .

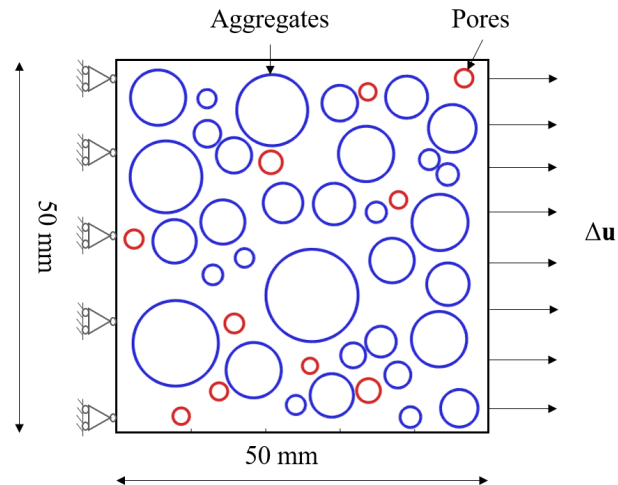


**Figure IV .5:** Geometry and boundary conditions of tension test on concrete plate and an example of distribution of pores and aggregates

The concrete sample is considered as a heterogeneous material composed of cement matrix, aggregates (or inclusions) and pores. Random distributions of pores and aggregates are generated, by using the so-called take-and-place method (Wang et al., 1999), based on the Fuller curve (Fuller and Thompson, 1907). For the sake of simplicity, all aggregates and pores are assumed to have a circular shape. The diameter of pores ranges from 2 to 4mm. The distribution of aggregates size is based on the experimental data presented in (Hirsch, 1962). The aggregates smaller than 2.36mm are considered part of the cement matrix. The sieve size ranges with passing and retaining percentages are presented in Table. IV .1. And the mechanical parameters of each constituent are given in Table. IV .2. The volumetric (or area in two-dimensional configuration) fraction of

aggregates is  $P_{agg} = 40\%$  while that of pores is  $P_{pore} = 2\%$ .

**Table IV .1:** Gradation of coarse aggregates of studied concrete ([Hirsch, 1962](#))

Sieve size (mm)	19.00	12.70	9.50	4.75	2.36
Total passing percentage (%)	100	97	61	10	1.4

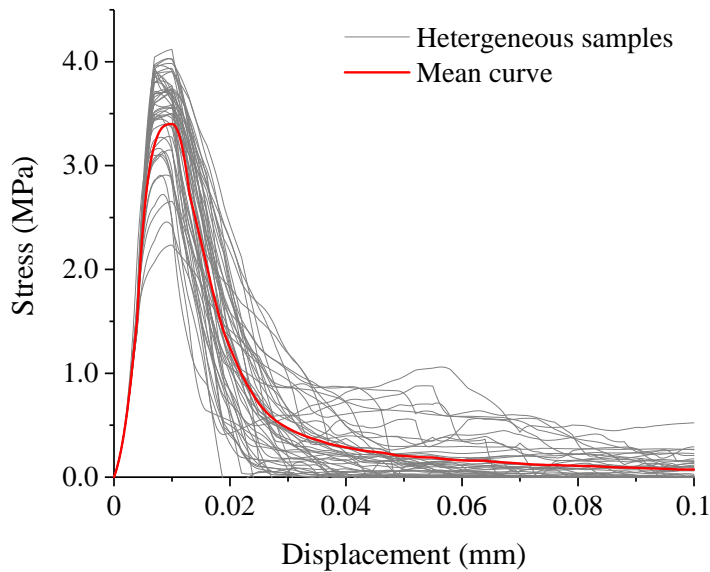
**Table IV .2:** Mechanical properties of constituents ([Wang et al., 2015](#))

Constituent	Young's modulus	Poisson's ratio	Fracture energy
	E (MPa)	$\nu$	$G_0$ (N/mm)
Aggregate	70,000	0.2	-
Motar	25,000	0.2	0.06
ITZ	-	-	0.03

For PD modelling, the discretization spacing is chosen as  $\Delta x = 0.5mm$ . To ensure the stability of numerical results, the displacement increment is selected as  $1 \times 10^{-6}mm$ . As the real distribution of aggregates and pores is not completely known, 50 random realizations are here considered. This allows studying the effect of micro-structure on the overall mechanical responses and cracking patterns.

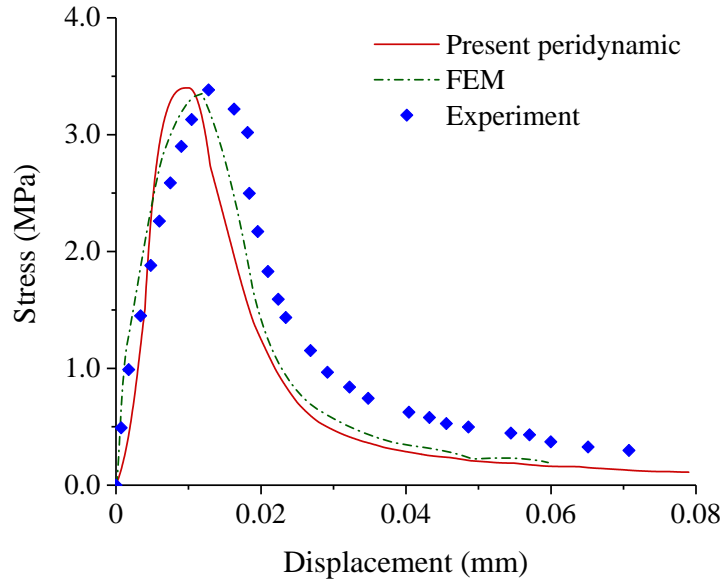
In Fig. IV .6(a), one shows the overall stress-displacement curves obtained from 50 random micro-structures as well as the mean curve. It can be seen that the concrete sample in tension test exhibits an elastic-brittle behavior. One observes a quasi linear elastic response before the peak stress, followed by a sharp material softening in the post-peak regime. There are important scatters between fifty curves. It seems that the overall mechanical response of concrete sample is strongly influenced by the distribution of aggregates and pores. In Fig. IV .6(b), the mean stress-displacement curve obtained with the PD model is compared with that issued from finite element (FE) simulations performed in ([Wang et al., 2015](#)), and the experimental results ([Hordijk, 1992](#)). The FE simulations were also performed on random micro-structures and the mean stress-displacement curve is presented in IV .6(b). One can see that in a global way, the PD model well agrees with the experimental data and the FE result. However, in spite of 50 random realizations

used, there are still some scatters with the experimental data. Several reasons can be invoked. For instance, most cement paste can exhibit important plastic deformation which is neglected here. Cohesive cracks are also observed in concrete materials while a brittle cracking mode is assumed here. Further, the use of a higher number of realizations should also improve the numerical prediction. Some small differences are also observed between the PD and FE results. Such differences can be due to the fact the random micro-structures used in two models are not the same.



(a) Stress-displacement curves obtained from 50 random micro-structures and calculated mean curve

In Fig. IV .7, one shows the cracking patterns of eight random micro-structures among fifty considered ones. It is found that the crack patterns are clearly influenced by the distribution of aggregates and pores. Cracks mainly appear in the weakest areas of the concrete samples, that is, the areas with more pores and around interface between aggregates and cement matrix. After the initiation of micro-cracks in these weak areas, these micro-cracks propagate and gradually connect to form macroscopic cracks, and then expand to the upper and lower boundaries. It can also be observed from the crack patterns that the size and location of the pores have a certain influence on the crack propagation path, and the cracks tend to pass through large pores with more sections in the interface transition zone. Further, there is only one through crack in most of the random specimens, and in a few ones, multiple cracks initiate and expand at the same time. These through cracks



(b) Comparisons of stress-displacement curves respectively obtained from PD and FE models with experimental data

**Figure IV .6:** Global stress-displacement curves in tension test of concrete sample

are affected by the coarse aggregates and interface transition zones, the bifurcation occurs randomly. In addition, although cracks tend to appear in sections with many pores, they do not necessarily appear in weak locations with pores near the surface. The cracking patterns observed in this study are globally consistent with the experimental observations (Hordijk, 1992).

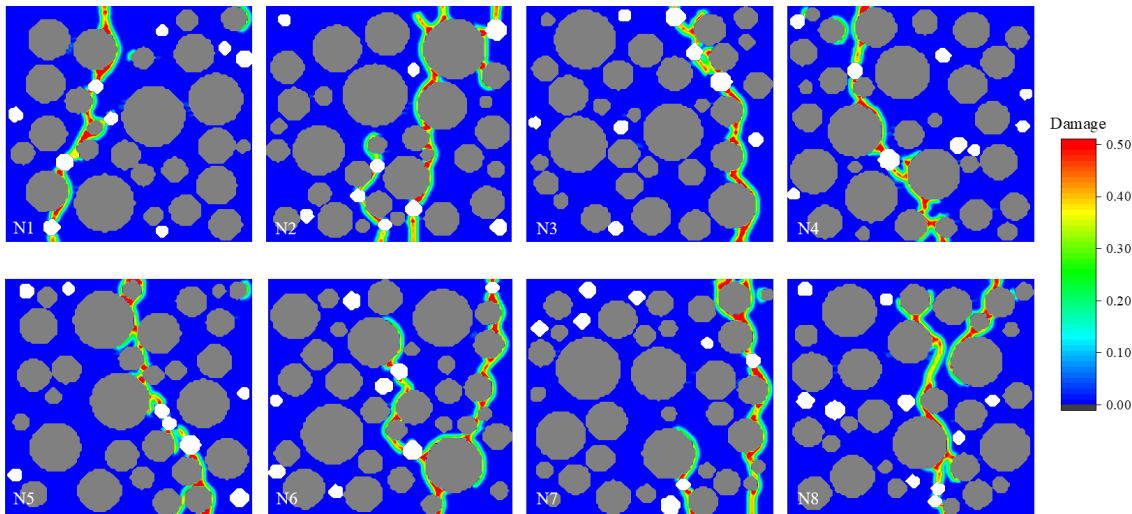


**Figure IV .7:** Cracking patterns in eight selected random micro-structures

After comparing the results obtained with the PD model with those from FE simulations and experimental data, it seems that the PD is able to describe not only the global mechanical responses but also the initiation and propagation of multiple cracks. It seems that the PD model is more efficient than the FE method in capturing complex cracking patterns, in particular with multiple cracks (Wang et al., 2015).

## 4.2 Analysis of shrinkage and heating induced cracking

In this part, we shall investigate both shrinkage and heating-cooling induced cracks in concrete-like materials by using the PD model. Numerical simulations are based on our previous experimental study reported in Section.II 2. The emphasis is put on the study of aggregates (inclusion) stiffness on cracking patterns.

### 4.2.1 Numerical modelling with PD model

Laboratory tests presented above were performed in 3D conditions. In the ideal situation, 3D numerical simulations should be developed. However, due to the complexity of micro-structure and cracking patterns of concrete materials, the 3D numerical modelling requires high computation cost. Therefore, as the first stage of study, simplified 2D numerical simulations have been widely performed on micro-structures taken from some representative planes on 3D micro-tomographic images to investigate the mechanical behaviors of concrete composites. For instance, in the recent work (Ozbek et al., 2019), the



dynamic behavior of different porous concretes was investigated by 2D numerical simulations in the framework of finite element method. The distributions of aggregates and macro-voids in the samples were based on real 3D tomographic images. A good qualitative agreement was obtained between the numerical and experimental results. Furthermore, in the previous study (Ren et al., 2015), 2D meso-scale finite element models have been developed based on 3D high-resolution X-ray tomographic images to simulate crack propagation processes in concrete composites under uniaxial tension loading. They have investigated the effects of mesh type, loading path and fracture parameters on both the global stress-strain curves and cracking patterns. The numerical results agreed qualitatively and quantitatively well with the experimental data. Therefore, the usefulness of simplified 2D numerical simulations has been demonstrated.

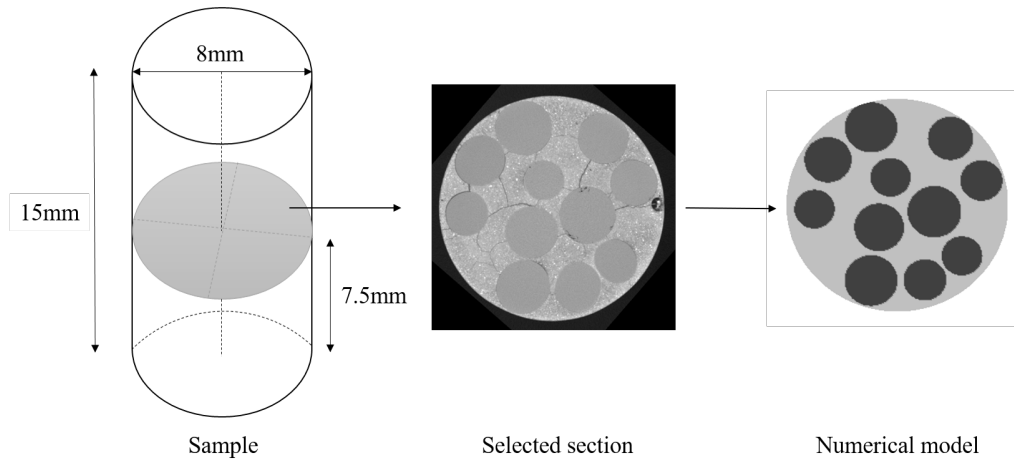


**Figure IV .8:** Selected representative micro-structure of concrete composite for simplified 2D modelling

Inspired by those previous studies, simplified 2D simulations are also performed in this study. The cross section located in the middle of sample is selected as the representative micro-structure of concrete composite. The geometry of the selected section and the distribution of inclusions are shown in Fig. IV .8. For PD modelling, the cross section is discretized into material particles based on a uniform grid with a spacing of  $\Delta x = 0.04mm$ . Further, three basic parameters of the cement paste have been identified by using experimental data reported in (Li, 2016): the volume density is  $1530kg/m^3$  and the Young modulus is  $E_c = 15GPa$ . For the value of critical fracture energy  $G_0$  of the cement paste, different values can be found in literature (Carpinteri and Ingraffea, 2012), ranging in  $3.5 - 20.4J/m^2$ . In this study, the value of  $15J/m^2$  is used. The main properties of inclusions are given in Table. IV .3. And the linear thermal expansion coefficient of the

cement paste used in this study is  $10 \times 10^{-6}/K$  (Li et al., 2018).

**Table IV .3:** Parameters for different materials of inclusions (Li et al., 2020)

	Case 1	Case 2	Case 3	Case 4	Case 5
Materials	Polyamide 6.6	Polyoxymethylene	Glass	Titanium	Zirconium
Density ( $g/cm^3$ )	<u>1.14</u>	<u>1.40</u>	<u>2.50</u>	<u>4.45</u>	<u>6.05</u>
Young's modulus (GPa)	1.70-2.00	2.40-2.80	<u>68</u>	112	<u>200</u>
Linear thermal expansion coefficient ( $10^{-6}/K$ )	70-100	80-100	<u>9.6</u>	8.9	<u>10</u>
Poisson's ratio	0.38-0.45	0.35-0.43	0.17-0.25	0.26-0.34	0.23-0.32

\* The underlined values are provided by the material production company, the others are obtained from the literature review. For sake of comparison, the elastic modulus and linear thermal expansion coefficient of cement paste are  $E_c = 15GPa$  and  $\alpha_c = 10 \times 10^{-6}/K$ , respectively.

#### 4.2.2 Simulation results of step 1

As shown in Fig. II .2, the whole drying process is composed of two steps. In the first step, temperature is held constant while it is increased and decreased during the second step. In order to separate thermal cracking from shrinkage induced one, numerical simulations are also performed by two steps. The emphasis of the first step is put on the drying shrinkage cracking. Further, the concrete composite 3 with glass balls (case 3:  $E_i = 68GPa$ ) is used as a reference material. Similarly to previous studies (Fu et al., 1994; Grassl et al., 2010), the drying shrinkage is represented by a prescribed compressive bond stretch. More precisely, in previous experimental works, the macroscopic shrinkage deformation of cement-based materials has been measured for different types of cement-

based materials. For instance, in (Almudaiheem, 1991), the shrinkage induced strain for neat cement pastes with  $w/c$  ratio of 0.4 – 0.6 and dried at a relative humidity of 11% for 6 – 240 days was about 0.46 – 0.55%. In (Fu et al., 1994), the shrinkage strain values of 0.2 – 1.3% were obtained for neat cement paste with  $w/c$  ratio of 0.25 – 0.70 during a drying period of 6 months. Therefore, as for the previous studies (Fu et al., 1994; Grassl et al., 2010), the value of shrinkage strain of cement composites studied here during the first drying step is estimated as 0.5%. On the other hand, this macroscopic shrinkage strain should be converted to the local compressive bond stretch. According to the relationship between a given macroscopic strain tensor  $\mathbf{E}(x)$  and the equivalent PD deformation state  $\underline{\mathbf{Y}}$  given in (Silling and Lehoucq, 2010):  $\underline{\mathbf{Y}} = \mathbf{E}(\mathbf{x})\xi + o(|\xi|^2)$ , the local bond stretch is approximately equal to the macroscopic linear strain. As a consequence, the prescribed value of compressive bond stretch during the first drying step is taken as  $\bar{s} = 0.5\%$ . Further, in order to represent the progressive propagation of drying process from the external surface to the center of sample, the cross section is divided into 21 layers. And the compressive bond stretch is prescribed layer by layer. In each layer, the maximum value of  $\bar{s} = 0.5\%$  is increased by 10 increments. In Fig. IV .9(a) to IV .9(c), one shows the distribution of prescribed compressive bond stretch at three different instances of drying process. The compressive bond stretch zone (equivalently shrinkage zone) starts from the outside surface and propagates towards to the center of sample. At the final state, all the section of sample is dried and shrined.

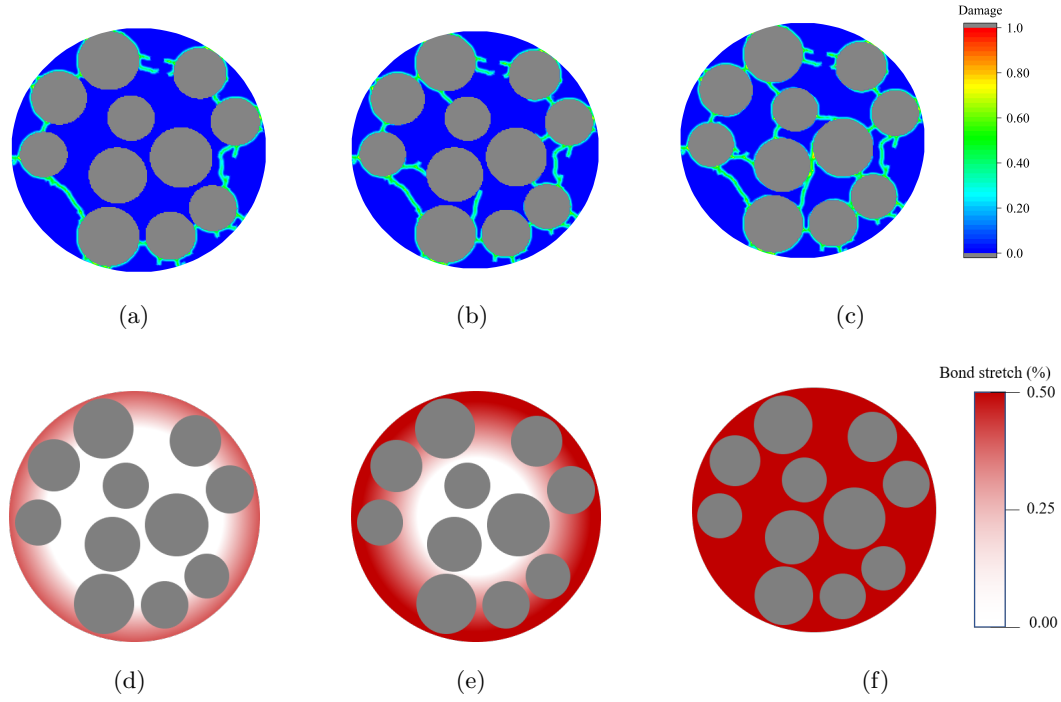


**Figure IV .9:** Evolution of damage distribution in composite case 3 (glass ball) at three instances of drying process represented by prescribe bond stretch value

The evolution of damage distribution is shown in Fig. IV .9 for three successive instances of drying process. In a general way, with the progress of dried zone, cracks initially appear around inclusions (Fig. IV .9(a)) and then propagate into the cement matrix. Cracks between inclusions tend to connect with each other. Further, some cracks spread the exterior board of sample (Fig. IV .9(b) and Fig. IV .9(c)). In case of glass balls, as the stiffness of inclusions is higher than that of cement matrix, the principal cracking mechanism is the fact that the presence of stiff inclusions restrains the shrinkage of cement paste and then induces the local concentration of tensile stress and strain, leading to interface debonding and creation of cracks.

For the purpose of quantifying the stress concentration in the concrete composite, a scalar valued stress invariant, the von Mises equivalent stress is calculated. The relationship between Cauchy stresses and PD forces has been established by (Moës et al., 1999):

$$\sigma_{ij}^{\mathbf{k}} = 2\mathbf{t}_j^{(\mathbf{k})(\mathbf{k}_i)} \Delta x_i^{(k)(k_i)} V^{k_i} \quad (\text{IV .7})$$

with  $i, j = 1, 2, 3$ . The vector  $\mathbf{t}^{(\mathbf{k})(\mathbf{k}_i)} = (t_1, t_2, t_3)^T$  represents the force density that material point  $\mathbf{x}_{(\mathbf{k}_i)}$  exerts on material point  $\mathbf{x}_{(\mathbf{k})}$ , in which  $k_i$  is the index of material

point next to material point  $\mathbf{x}_{(k)}$  in direction  $i$ .  $\Delta x_i^{(k)(k_i)}$  is the distance between the two material point in  $i$ . Then, the von Mises equivalent stress is calculated from the Cauchy stress tensor by  $\sigma_{\text{eq}} = \sqrt{\sigma_{ij}^d \sigma_{ij}^d}$ , with  $\sigma_{ij}^d$  being the deviatoric stresses. The distribution of the equivalent stress is shown in Fig. IV .10. It can be observed that the stress concentration occurs mainly around the inclusions, between the inclusions when they are close to each other generating strong interactions as well as between the inclusions and exterior board of the sample due to the boundary effects. For the same reasons, some stress concentration is also observed around the exterior board of the sample. Physically, when the cement paste is subjected to a compressive strain due to drying shrinkage, due to the presence of stiff inclusions, tensile radial stresses are generated around the inclusions and lead to the creation of radial cracks. The intensity of stress concentration is proportional to the difference of stiffness between the inclusions and cement paste. On the other hand, in the case of spherical inclusions, no interface debonding between the cement paste and inclusions is observed. However, in the presence of inclusions with complex shapes, the interface debonding can be generated. The results presented in Fig. IV .10(a) seem to be coherent with these physical mechanisms and with the cracking patterns observed in the experimental study (Fig. IV .10(b)) even if only 2D calculations are performed here. However, 3D simulations in future studies would improve the description of local stress distribution and provide more complete view of cracking patterns.

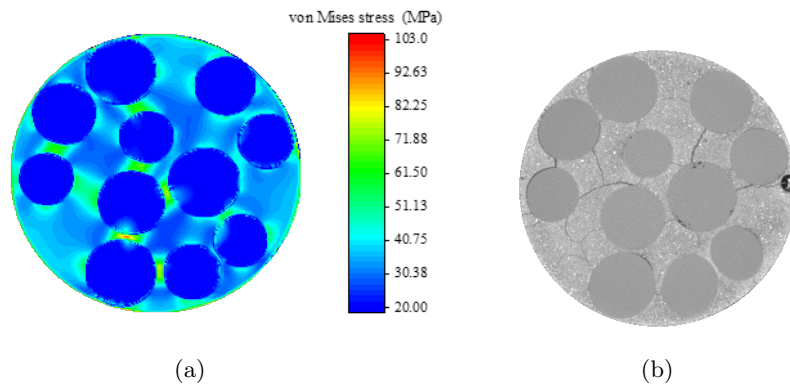


**Figure IV .10:** (a) Distribution of the equivalent stress in composite case 3 (glass ball); (b) Cracked cross section at the end of step 1 of drying

The influence of inclusion stiffness on cracking patterns is here studied by a series of comparative simulations. Six different values of Young modulus are used for different types of inclusions: five values corresponding to those of selected inclusions in laboratory tests (see Table. IV .3)(cases 1-5) and the last one is  $15GPa$  (case 6), which is equal to

the Young modulus of cement paste.

The damage distributions for the six considered cases of inclusions are presented in Fig. IV .11. When the stiffness of inclusions is lower than that of the cement paste, as shown in Figures IV .11(a), IV .11(b) and IV .11(c), the drying shrinkage of cement paste is weakly restrained. However, a number of cracks are still obtained (maybe except the case with the ratio of 2/15). These cracks are mainly generated by the interaction effect between the drying gradient and the presence of inclusions. On the other hand, for the cases of stiffer inclusions shown in Figures IV .11(d), IV .11(e) and IV .11(f), the drying shrinkage is strongly restrained. This generates significant tensile circumferential stresses round the inclusions leading to the creation of radial cracks. Further, there are also strong interactions between the inclusions due to their high volumetric fraction. The interactions are at the origin of cracks between inclusions and even interface debonding in some cases. It is obvious that the tensile stress and interactions are stronger when the stiffness ratio is larger. The density of induced cracks is then higher.

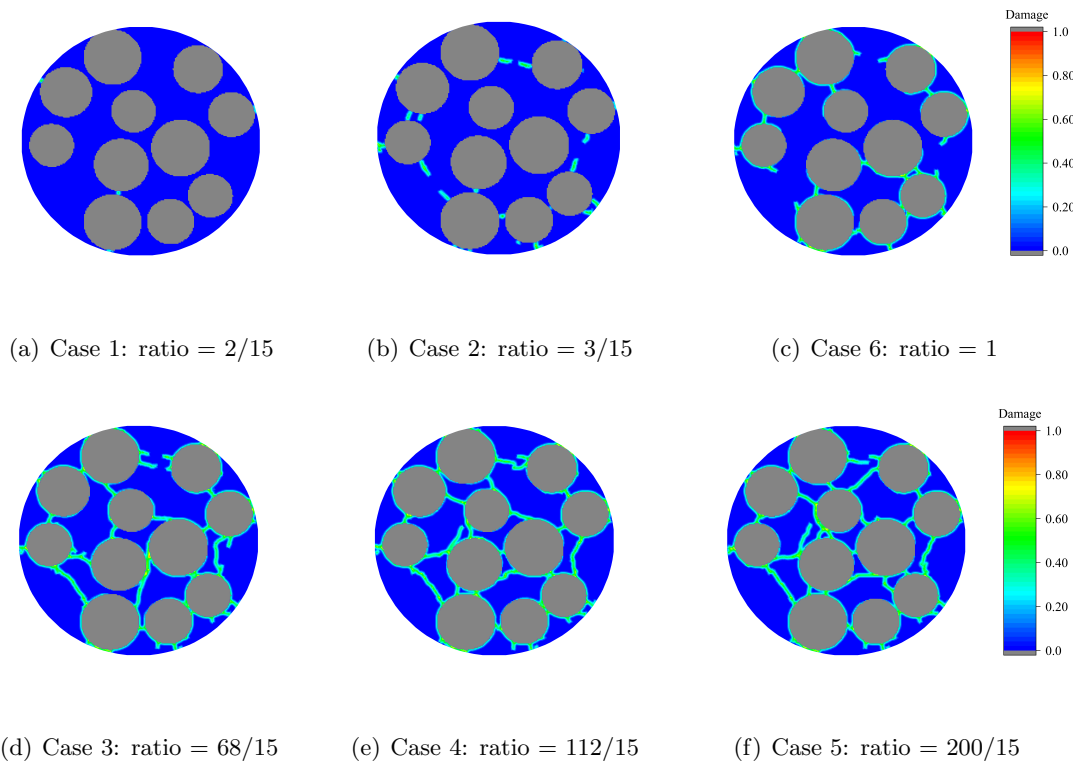


**Figure IV .11:** Distributions of damage for different values of the elastic modulus ratio between inclusions and cement paste

Besides the qualitative analysis of cracking patterns, the effects of inclusion stiffness

on the shrinkage cracks are also quantitatively investigated in terms of the accumulated crack length and average crack width. The accumulated crack length  $l_c$  is assumed as

$$l_c = \sum_{i=1}^{n_c} l_i \quad (\text{IV .8})$$

where  $l_i$  denotes the element size, for instance  $l_i = \Delta x$ .  $n_c$  is the number of cracked elements. On the other hand, the average crack width is calculated by the following expression:

$$w_c = \frac{\sum_{i=1}^{n_c} l_i h_i s_i}{\sum_{i=1}^{n_c} l_i} \quad (\text{IV .9})$$

$s$  is the bond stretch, and  $h = \Delta x$  is the bond length of two connected particles.

In Fig. IV .12, one shows the variations of accumulated crack length and average crack width with the inclusion elastic modulus. It is found that the accumulated crack length increases with the inclusion stiffness while the average crack width decreases.

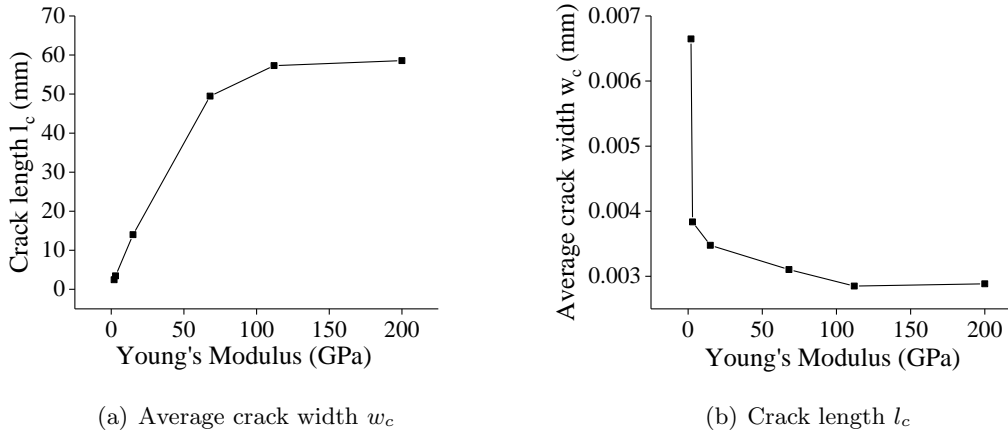


**Figure IV .12:** Variation of accumulated crack length and average crack width with inclusion elastic modulus for a constant modulus of cement matrix ( $15GPa$ )

### 4.2.3 Simulation results of step 2

During the second step, in order to accelerate further drying process, the temperature is increased to  $105^{\circ}C$  (see Fig. II .2) for 20 days before being cooled to  $20^{\circ}C$ . Due to this thermal cycle, the concrete samples are considered as fully dried. However, as the thermal dilation coefficients of inclusions are clearly different with that of cement paste (see Table. IV .3), the temperature change induces non-uniform dilations and contractions which are responsible of thermal cracks. Therefore, both drying induced and thermal cracks should

be taken into account for the second step. Unfortunately, due to the technical limitation, no scanned images were taken under the prescribed temperature of  $105^{\circ}C$ . X-ray images were taken only after the cooling of samples. Therefore, comparisons between numerical results and experimental observations are presented only for the cooled samples.

In order to emphasize the thermal cracking effect, the composite case 2 is specifically investigated here as it has a high thermal dilation coefficient (see Table. IV .3). The basic input parameters are as follows. The elastic modulus of inclusion is  $E_i = 3GPa$  and the linear thermal expansion coefficient is  $\alpha_i = 100 \times 10^{-6}/K$ . The elastic modulus of cement paste is  $E_c = 15GPa$  and the linear thermal expansion coefficient is  $\alpha_c = 10 \times 10^{-6}/K$ . In this simulation, the sample is first heated from  $20^{\circ}C$  to  $105^{\circ}C$  while the RH is decreased from 12% to 3% and then cooled to  $20^{\circ}C$ . Thus, the thermal dilation and drying shrinkage strains are simultaneously prescribed to the related material bonds during the heating phase, while only the thermal strain is applied during the cooling phase. According to some previous studies (Helmuth and Turk, 1967), it was shown that the further drying from 47% RH to 7% RH resulted in an additional 0.1% shrinkage deformation. In (Hansen and Almudaiheem, 1987), it was also found that for neat cements with a  $W/C$  ratio of 0.4 – 0.6, dried at 0% RH resulted in an addition shrinkage of 0.1% – 0.3% compared with that dried at 20% RH. Therefore, the drying shrinkage deformation during the second step is estimated of about 0.1% and it is represented by a compressive bond stretch of  $\bar{s} = 0.1\%$ . On the other hand, the thermal strains are calculated by using the values of temperature change and thermal expansion coefficients and they are prescribed to both the cement matrix and inclusions. More precisely, the thermal strains during the heating phase are  $\bar{s}_{t_i} = -\alpha_i \times (85^{\circ}C) = -0.85\%$  for the inclusions and  $\bar{s}_{t_c} = -\alpha_c \times (85^{\circ}C) = -0.085\%$  for the cement matrix (note that in this paper, tensile strains are denoted as negative values while compressive ones as positive values). The same values of thermal strains but with an opposite sign are used in the cooling phase.



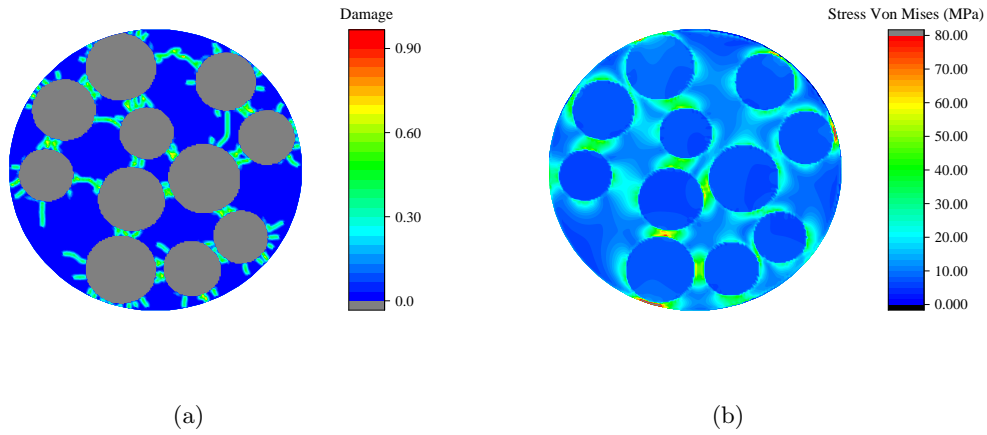


**Figure IV .13:** Distributions of damage (a) and of equivalent stress (b) at the end of heating phase

In Fig. IV .13, one shows the distributions of induced damage and equivalent stress at the end of heating phase. It is clearly seen that due to the fact that the thermal expansion of inclusions is restrained by the surrounding cement paste, a strong stress concentration is generated around the inclusions. It is mainly dominated by the tensile circumferential stress. As a consequence, radial cracks are created by the heating process. One also observes significant interactions between the neighboring inclusions and related cracks in the zones between those inclusions. The numerical results obtained in this study are consistent with some analytical solutions on the stress distribution generated by the expansion of a single spherical inclusion (Garboczi, 1997).

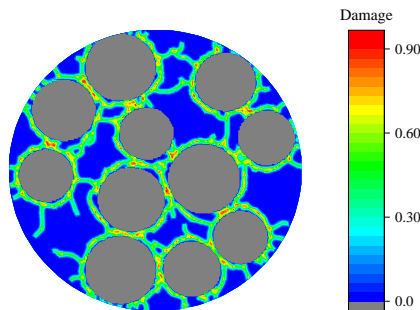


**Figure IV .14:** Distribution of damage at the end of cooling phase

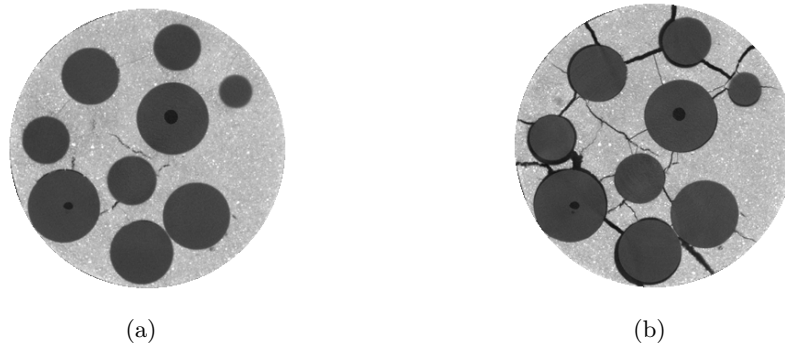


**Figure IV .15:** Experimental observations of cracked cross section before heating (a) and that after heating-cooling process (b) (Li et al., 2020)

By assuming a reversible behavior between heating and cooling, the cooling process induces a thermal contraction. Once more, due to the large difference of thermal dilation coefficient between the inclusions and cement paste, the thermal contraction of inclusions is much larger than that of cement paste. As a basic difference with the heating phase, the differential thermal contraction generates tensile circumferential stresses around the inclusions, especially on the interfaces with the cement paste. As a consequence, the interfacing debonding is generated by the creation of circumferential cracks. This is qualitatively well shown by the distribution of damage at the end of cooling phase presented in Fig. IV .14. This result has a good agreement with the experimental results shown in Fig. IV .15. Specifically, more cracks can be clearly observed after the heating and cooling process.

## 5 Concluding remarks

In the present work, based on the bond-based peridynamics theory (PD), a specific numerical method is presented for the modelling of cracks in brittle heterogeneous materials subjected to drying shrinkage and temperature variation. Based on a previous experimental study, a series of numerical simulations have been performed on concrete composite samples with different types of inclusions. The effects of inclusion stiffness on cracking patterns have been investigated. Based on the obtained results, the following main remarks can be formulated.

Through comparisons with experimental data and finite element simulations, the efficiency of the proposed PD method in modelling cracking process in heterogeneous materials has been verified. Moreover, the proposed method is particularly efficient for the description of initiation and propagation of multiple cracks.

---

The proposed method is also able to deal with multi-physical problems such as cracks induced by drying shrinkage and temperature change. For the specific concrete composites considered in this study, it is found that the elastic stiffness contrast between inclusions and cement past significantly affects the cracking patterns. A high stiffness difference enhances the initiation and propagation of cracks induced by drying shrinkage. The thermal cracking process is mainly controlled by the differential thermal dilation between inclusions and cement paste. In general, cracks are initially generated around interfaces between inclusions and cement paste and then progressively propagate into the matrix.

Although simplified two-dimensional simulations have provided a good approximation of mechanical responses of concrete composites, three-dimensional simulations are more realistic and have to be developed in future studies for a fine description of cracking patterns and for quantitative comparisons with experimental results.



## Chapter V

# A Fully Coupled Hydro-mechanical Peridynamic Model for Saturated and Partially Saturated Porous Media

### 1 Introduction

In the previous chapter, the mechanical mechanisms related to the drying shrinkage cracking have been studied via a series of numerical simulations by using an equivalent drying strain field loading. In this chapter, a fully coupled hydro-mechanical peridynamic model is firstly developed to simulate the hydro-mechanical coupling processes in the cementitious material. The proposed model is capable of simulating the initiation and evolution of cracks in the porous medium as well as the impact of desiccation cracks on the movement of moisture and the mechanical properties of concrete. After that, the proposed numerical model is used to simulate the coupled hydro-mechanical behavior of concrete subjected to drying. Therefore, the obtained shrinkage cracking is more reliable than that obtained with a simple mechanical simulation and can help us to better understand the mechanical response of concrete during drying.

This chapter consists of three parts. In the first part, based on the first law of thermodynamics and PD theory and with the combination of the free energy density formulation, a saturated porous media model is firstly developed in the framework of bond-based PD theory. Then, the proposed numerical model is extended in the partially saturated porous

medium to describe the fully coupled hydro-mechanical processes. In the third part, the proposed model is firstly validated by simulating two classical poromechanics problems: Biot’s one-dimensional consolidation problem and the drainage of soil column. After that, it is used to study the drying processes of cementitious material. The evolution of the drying front and the propagation of cracks in cement paste is studied and analyzed. Finally, in order to study the influence of the matrix behavior and the inclusion size on the evolution of cracking network, a series of parametric studies are carried out.

## 2 Development of a coupled hydro-mechanical peridynamic model for saturated porous medium

The saturated porous medium is considered as a mixture composed of matrix and connected voids, which is filling in the voids. As shown in Fig.V .1, the connected porous space is the voids in which a fluid flow is filled. And the matrix is composed of both a solid part and a possible occluded porosity, in which no water flow occurs. Therefore, the ‘porosity’ is defined as the ratio of the volume of the connected pore space to the total volume of voids.

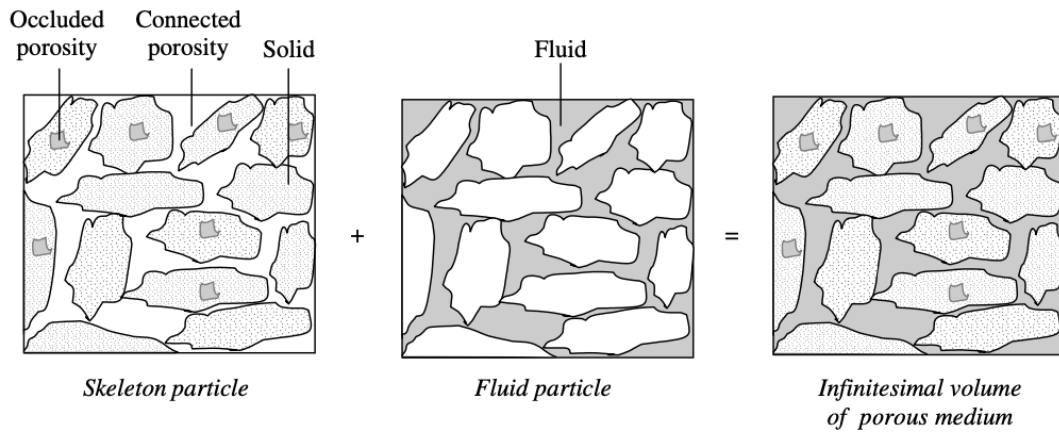


Figure V .1: Composition of the saturated porous medium

In a horizon  $H$ , for the interaction between the studied material point and any other material points, both the solid phase and fluid flow are taken into account. In other words, the fluid flow is non-local too.

## 2.1 Peridynamic thermal diffusion coupling with hydro-mechanics

In peridynamics method, the first law of thermodynamics is written in the form as (Silling and Lehoucq, 2010):

$$\dot{\psi} = w_{abs} + Q_b + s_b \quad (\text{V .1})$$

Where  $\dot{\psi}$  is the time rate of change in the internal energy storage density,  $Q_b$  is the rate of heat energy exchange with other material points, and  $s_b$  is the prescribed volumetric heat generation per unit mass. The  $w_{abs}$  represents the absorbed power density and is defined as:

$$w_{abs} = \int_H \mathbf{t}(\mathbf{x}, \mathbf{x}', t) \cdot [\mathbf{v}'(\mathbf{x}, t) - \mathbf{v}(\mathbf{x}, t)] dV' \quad (\text{V .2})$$

in which  $\mathbf{v}$  is the velocity. the bond force density  $\mathbf{t}(\mathbf{x}, \mathbf{x}')$  is given as  $\mathbf{t}(\mathbf{x}, \mathbf{x}') = \mathbf{f}(\mathbf{x}, \mathbf{x}')/2$ .

Associated with the material point  $\mathbf{x}$ , the relative position in the deformed configuration can be stored in deformation state  $\underline{\mathbf{Y}}$ :

$$\underline{\mathbf{Y}}[\mathbf{x}, t](\mathbf{x}' - \mathbf{x}) = \mathbf{y}(\mathbf{x}', t) - \mathbf{y}(\mathbf{x}, t) \quad (\text{V .3})$$

Similarly, a force state  $\underline{\mathbf{T}}$ , in which the value of any  $\mathbf{t}(\mathbf{x}, \mathbf{x}', t)$  is given, can be defined as:

$$\underline{\mathbf{T}}[\mathbf{x}, t](\mathbf{x}' - \mathbf{x}) = \mathbf{t}(\mathbf{x}, \mathbf{x}', t) \quad (\text{V .4})$$

With the help of these definitions, the absorbed power density takes the form as :

$$w_{abs} = \underline{\mathbf{T}} \bullet \dot{\underline{\mathbf{Y}}} \quad (\text{V .5})$$

It is noted that, the symbol ' $\bullet$ ' means the dot product of the force state and the time rate of deformation state. Similarly in the classical continuum mechanics, the absorbed power density in peridynamic is analogous to the stress power  $\sigma \cdot \dot{\mathbf{F}}$ , where  $\sigma$  is the Piola stress and  $\mathbf{F}$  is the deformation gradient tensor.

In order to define the internal energy of the fluid, the fluid free enthalpy  $g_f = g_f(p, T)$ , which is a function of pressure  $p$  and temperature  $T$  of the fluid, is introduced (Coussy, 2004). Based on the non-local theory, the internal energy density of fluid  $w_f$  is also related to the bonds connected to  $\mathbf{x}$ , similar with the absorbed power density:

$$w_f = \int_H g_f(\bar{p}, \bar{T}) \dot{m}_f(\mathbf{x}', \mathbf{x}, t) dV' \quad (\text{V .6})$$

where  $\dot{m}_f$  is the fluid mass through a bond. The  $g_f$  is the free enthalpy state which depends on the mean pressure  $\bar{p}$  and mean temperature  $\bar{T}$  of a bond.

Similar with the absorbed power density, two state variables are defined : the free enthalpy state  $\underline{\mathbf{G}}_f$  and fluid mass state  $\underline{\mathbf{m}}_f$  of all the bonds connected to  $\mathbf{x}$ . The internal energy density of the fluid in peridynamics could be written as:

$$w_f = \underline{\mathbf{G}}_f \bullet \underline{\dot{\mathbf{m}}}_f \quad (\text{V .7})$$

As the emphasis of the present work is put on the coupling of peridynamics method and hydro-mechanical coupling processes, an isothermal condition is adopted. Under isothermal conditions, the first law of thermodynamics could be rewritten as:

$$\dot{\psi} = \underline{\mathbf{T}} \bullet \underline{\dot{\mathbf{Y}}} + \underline{\mathbf{G}}_f \bullet \underline{\dot{\mathbf{m}}}_f \quad (\text{V .8})$$

## 2.2 Linear poroelastic constitutive equations in peridynamics

By combining the classical linear theory of thermoporoelastic (Jia, 2006) and the peridynamics theory (Silling, 2010), the free-energy density is given as a potential function:

$$\psi(\underline{\mathbf{U}}, \underline{\mathbf{m}}_f) = \psi(\underline{\mathbf{Y}}^0) + \underline{\mathbf{T}}^0 \cdot \underline{\mathbf{U}} + \frac{1}{2} \underline{\mathbf{U}} \cdot \underline{\mathbb{K}} \cdot \underline{\mathbf{U}} + \underline{\mathbf{G}}_f^0 \cdot \underline{\mathbf{m}}_f - \frac{Q_b}{\rho_f} \underline{\mathbf{B}} \cdot \underline{\mathbf{m}}_f \cdot \underline{\mathbf{U}} + \frac{1}{2} Q_b \left( \frac{\underline{\mathbf{m}}_f}{\rho_f} \right)^2 \quad (\text{V .9})$$

where  $\underline{\mathbf{Y}}^0$  and  $\underline{\mathbf{T}}^0$  are defined as the equilibrated deformation and force state, respectively.  $\underline{\mathbf{U}}$  is the displacement vector state, and  $\underline{\mathbf{U}} = \underline{\mathbf{Y}} - \underline{\mathbf{X}}$ .  $\underline{\mathbb{K}}$  presents the modulus state, and given by (Silling, 2010) :

$$\underline{\mathbb{K}} = \underline{\mathbf{T}}_{,y}^0 \quad (\text{V .10})$$

$Q_b$  and  $\rho_f$  represent the Biot's modulus and the pore fluid density, respectively. Analogous to the poromechanics of (Coussy, 2004), the tensor of Biot coefficient can be defined as:

$$\underline{\mathbf{B}} = \psi_{,p} \underline{\mathbf{Y}} \quad (\text{V .11})$$

According to the nullity of the intrinsic dissipation law of a reversible transformation, the state equations of partially saturated porous medium are given as:

$$\underline{\mathbf{T}} = \psi_{,\underline{\mathbf{Y}}} = \underline{\mathbb{K}} \cdot \underline{\mathbf{U}} - \frac{Q_b}{\rho_f} \underline{\mathbf{B}} \cdot \underline{\mathbf{m}}_f \quad (\text{V .12})$$

$$\underline{\mathbf{G}}_f = \psi_{,\underline{\mathbf{m}}_f} = \underline{\mathbf{G}}_f^0 - \frac{Q_b}{\rho_f} \underline{\mathbf{B}} \cdot \underline{\mathbf{U}} + \frac{Q_b}{\rho_f} \left( \frac{\underline{\mathbf{m}}_f}{\rho_f} \right) \quad (\text{V .13})$$

using the linear fluid state equation (Jia, 2006):

$$g_f = g_f^0 + \frac{p - p^0}{\rho_f} \quad (\text{V .14})$$

and combining the Eq. (V .13), the bond force density state can be rewritten as:

$$\underline{\mathbf{T}} = \underline{\mathbb{K}}^b \cdot \underline{\mathbf{U}} - \underline{\mathbf{B}} \cdot \underline{\mathbf{P}}_f \quad (\text{V .15})$$



in which  $\underline{\mathbf{P}}_f$  is the state of pore pressure. It is interesting to notice that the term  $\underline{\mathbf{T}}^{eff} = \underline{\mathbf{K}}^b \cdot \underline{\mathbf{U}}$  is analogous to the effective stress definition in classical continuum theory (Jia, 2006), thus  $\underline{\mathbf{K}}^b = \underline{\mathbf{K}} - Q_b(\underline{\mathbf{B}} \otimes \underline{\mathbf{B}})$  can be seen as the modulus state in drained condition.

### 2.3 Peridynamic motion equations coupling with hydro-mechanical process

By substituting the force density state Eq. (V.15) into the peridynamic equation of motion, the peridynamic equation of motion for porous medium can be expressed as:

$$\rho \ddot{\mathbf{u}}(\mathbf{x}, t) = \int_H c(s - b\gamma \bar{P}) \frac{\mathbf{y}' - \mathbf{y}}{|\mathbf{y}' - \mathbf{y}|} dV' + \mathbf{b}(\mathbf{x}, t) \quad (\text{V.16})$$

in which  $\bar{P}$  is the average fluid pore pressure of the bond connecting the materials  $\mathbf{x}$  and  $\mathbf{x}'$  and defined as:

$$\bar{P} = \frac{p(\mathbf{x}, t) + p(\mathbf{x}', t)}{2} \quad (\text{V.17})$$

The tensor of Biot coefficient is given as following (Oterkus et al., 2017; Zhou et al., 2020):

$$\underline{\mathbf{B}}(\mathbf{x}' - \mathbf{x}) = \frac{c}{2} b\gamma \frac{\mathbf{y}' - \mathbf{y}}{|\mathbf{y}' - \mathbf{y}|} \quad (\text{V.18})$$

where,  $b$  is the Biot coefficient and  $\gamma$  is called the coefficient of fluid pore pressure:

$$\begin{aligned} \gamma &= \frac{1}{E} & (1 - D) \\ \gamma &= \frac{1 - \nu}{E} & (2 - D) \\ \gamma &= \frac{1 - 2\nu}{E} & (3 - D) \end{aligned} \quad (\text{V.19})$$

### 2.4 Fluid flow state peridynamic equation for porous medium

The governing equations for the fluid flow in a porous medium can be described by Darcy's Law as (Biot, 1941):

$$\frac{\vec{\omega}}{\rho_f} = \frac{k}{\mu_f} (-\nabla p + \rho_f \mathbf{g}) \quad (\text{V.20})$$

and the mass balance equation:

$$\dot{m}_f = -div(\vec{\omega}) \quad (\text{V.21})$$

Here,  $k$  is the intrinsic permeability,  $\mu_f$  is the dynamic fluid viscosity and  $\mathbf{g}$  is the gravitational acceleration.

Combining with the constitutive relation Eq. (V.13), the fluid flow equation in peridynamics could be obtained as:

$$\dot{p}(\mathbf{x}, t) = \int_H Q_b(k_p \frac{p(\mathbf{x}', t) - p(\mathbf{x}, t)}{|\mathbf{x}' - \mathbf{x}|} - \frac{c}{2} b\gamma \dot{\mathbf{e}}) dV' \quad (\text{V.22})$$

$[p(\mathbf{x}', t) - p(\mathbf{x}, t)]/|\mathbf{x}' - \mathbf{x}|$  represents the fluid gradient at bond in the reference configuration (Oterkus, 2015).  $k_p$  represents the permeability in peridynamics model depends on the dimension of studied problems (Oterkus et al., 2017; Zhou et al., 2020):

$$\begin{aligned} k_p &= \frac{2k}{\mu_f A \delta^2} \quad (1 - D) \\ k_p &= \frac{6k}{\pi \mu_f h \delta^3} \quad (2 - D) \\ k_p &= \frac{6k}{\pi \mu_f \delta^4} \quad (3 - D) \end{aligned} \tag{V.23}$$

According to (Jia, 2006), the Biot modulus  $Q_b$  is a function of the porosity  $\phi$  and the bulk modulus of solid skeleton  $K_s$  and pore fluid  $K_f$ :

$$\frac{1}{Q_b} = \frac{(b - \phi)}{K_s} + \frac{\phi}{K_f} \tag{V.24}$$

### 3 Extension to the partially saturated porous medium

In partially saturated porous medium, the connected pores are filled with a liquid and gas mixture while all the connected pores are fully filled with fluid in the saturated one (see Fig.V.2). Therefore, the porosity of partially porous medium is composed of two parts: a liquid part  $\phi_f$  and a gas part  $\phi_a$ . The degree of saturation is represented by:

$$S_l = \frac{\phi_f}{\phi_f + \phi_a} \tag{V.25}$$

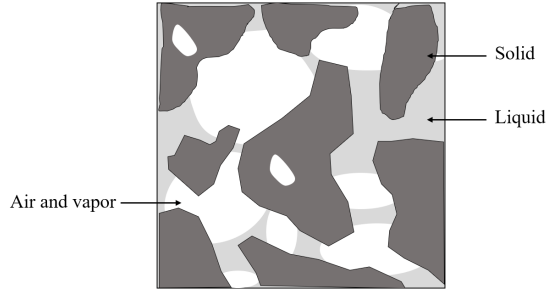


**Figure V.2:** Composition of the partial saturated porous medium

As in the laboratory tests, the variation of gas pressure is very small with respect to the variation of liquid pressure. For reason of simplicity, it is assumed that the gas pressure is zero ( $p_a \approx 0$ ) (Callari and Abati, 2009; Kim et al., 2012; Lewis and Schrefler, 1998; Vaunat et al., 1997). As a result, the relationship between capillary pressure and pore liquid pressure is given as:

$$p_c = -p_f \tag{V.26}$$

### 3.1 Peridynamic motion equation for partially saturated porous medium

Comparing with the full saturation condition, the pressure in partial saturation pore is composed by not only the liquid pressure but also the gas pressure. Hence, the pore pressure  $p^*$  is introduced for partially saturated porous medium,

$$p^* = S_l p_f \quad (\text{V .27})$$

Substituting Eq. (V .26) and Eq. (V .27) into the peridynamic motion equation Eq. (V .16), one can get the peridynamic motion equation for partially saturated porous medium:

$$\rho \ddot{\mathbf{u}}(\mathbf{x}, t) = \int_H c(s - S_l b \gamma \bar{P}_f) \frac{\mathbf{y}' - \mathbf{y}}{|\mathbf{y}' - \mathbf{y}|} dV' + \mathbf{b}(\mathbf{x}, t) \quad (\text{V .28})$$

in which  $\bar{P}_f$  is the mean fluid pore pressure of the bond connecting the materials  $\mathbf{x}$  and  $\mathbf{x}'$  and defined as:

$$\bar{P}_f = \frac{p_f(\mathbf{x}, t) + p_f(\mathbf{x}', t)}{2} \quad (\text{V .29})$$

### 3.2 Fluid flow state peridynamic equation for partially saturated porous medium

It is well known that the liquid–gas interface possesses its own proper interfacial energy and entropy because of the existence of surface tension. In view of this, the concept of equivalent pore pressure  $p^e$  has been introduced by (Coussy, 1995; Coussy et al., 1998):

$$p^e = p^* - U \quad (\text{V .30})$$

where  $U = \int_{S_l}^1 p_c(S_l) dS_l$  is the interfacial energy which accounts for the tensile stresses along the interfaces. It is interesting to noticed that  $U(S_l = 1) = 0$  in saturated porous medium, and the equivalent pore pressure is then equal to the liquid pressure.

Substituting Eq. (V .30) into the fluid flow constitutive equation Eq. (V .22), one can get the fluid flow equation for partially saturated porous medium:

$$\dot{p}_f(\mathbf{x}, t) = \int_H Q_b(k_r k_p \frac{p_f(\mathbf{x}', t) - p_f(\mathbf{x}, t)}{|\mathbf{x}' - \mathbf{x}|} - \frac{c}{2} S_l b \gamma \dot{\epsilon}) dV' \quad (\text{V .31})$$

in which  $Q_b$  is the Biot modulus for partially saturated porous medium and depends on the capillary pressure–saturation curves  $p_c(S_l)$ . As a result, the Eq. (V .24) is reformed as:

$$\frac{1}{Q_b} = \frac{S_l^2(b - \phi)}{K_s} + \frac{S_l \phi}{K_f} - \phi \frac{\partial S_l}{\partial p_c} \quad (\text{V .32})$$

Inspired by the anterior research works (ANDRA, 2005; Baroghel-Bouny et al., 2002; Bossart et al., 2002; Shao et al., 2005), the function proposed by Van Genuchten (Van Genuchten, 1980) is used:

$$S_l = S_l^r + (1 - S_l^r) [1 + (\epsilon p_c)^n]^{-m} \quad (V .33)$$

where  $S_l^r$  is the residual saturation degree,  $\epsilon$  is a scaling factor,  $m$  and  $n$  are two constants and can be fitted by using the experimental data.

The relative permeability of partially saturated porous medium is described by the following function (Coussy, 2004):

$$k_r = S_l^{1/2} \left[ 1 - \left( 1 - S_l^{1/m} \right)^m \right]^2 \quad (V .34)$$

$m$  is the same parameter in Eq.(V .33).

## 4 Numerical simulations

In this section, the proposed hydro-mechanical peridynamic model and the developed code will be firstly used to study two benchmark problems: the one dimensional consolidation of soil sample and the one dimensional desaturation of a sand column. To valid the performance of proposed model and developed code, the obtained numerical results will be compared with the analytical solution and the FEM solutions. After that, the developed model will be used to study the shrinkage drying cracks in cementitious materials.

### 4.1 Validation of proposed numerical model

In the two benchmark problems, two structures with simple geometries and under simple loads are studied. The consolidation of soil sample is firstly studied.

#### 4.1.1 One dimensional consolidation of soil sample

The studied soil sample is considered as fully saturated. The soil skeleton is assumed as a homogeneous elastic material with Young's modulus  $E = 1.0 \times 10^8 N/m^2$  and Poisson's ratio  $\nu = 1/3$ . The density of the material is specified as  $\rho = 1900 kg/m^3$ . Hydraulic conductivity of the soil skeleton  $k/\mu_f$  is  $1.02 \times 10^{-9} m^4/Ns$ , and the Biot modulus of the material is specified as  $Q_b = 1/(1.65 \times 10^{-10}) N/m^2$ . The fluid density  $\rho_f$  is  $1000 kg/m^3$  and is assumed incompressible.

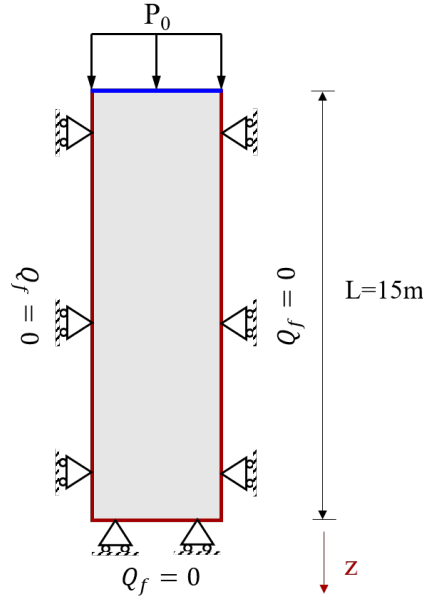


**Figure V .3:** Biot's one-dimensional consolidation: configuration and applied boundary conditions

The geometry and applied boundary condition are given in Fig.V .3. The specimen is  $L = 15m$  in height. It is subjected to a constant pressure of  $P_0 = 1 \times 10^4 N/m^2$  on the upper surface ( $z = 0$ ) while all the displacements on the bottom ( $z = L$ ) are blocked. On two lateral boundaries, only the horizontal displacement is blocked. The problem domain is discretized into 1000 material points with a characteristic dimension of  $\Delta x = 0.015m$ . The horizon  $\delta$  is assumed as  $3.015\Delta x$ . The time step size is chosen as  $\Delta t = 1 \times 10^{-6}s$ . According to the theory of Biot's consolidation (Biot, 1941) and the initial conditions, the pore water pressure and the displacement induced by the applied pressure  $P_0$  are given as

$$P(z, t = 0) = \frac{a - a_i}{ba} P_0 \quad (V .35)$$

$$u_z(z, t = 0) = a_i P_0 (L - z) \quad (V .36)$$

where  $b = 0.5$  is the Biot parameter,  $a$  and  $a_i$  are the final and instantaneous compressibility coefficients:

$$a = \frac{1 - 2\nu}{2G(1 - \nu)} \quad (V .37)$$

and

$$a_i = \frac{a}{1 + b^2 a Q_b} \quad (V .38)$$

where  $G$  is the shear modulus of studied material.

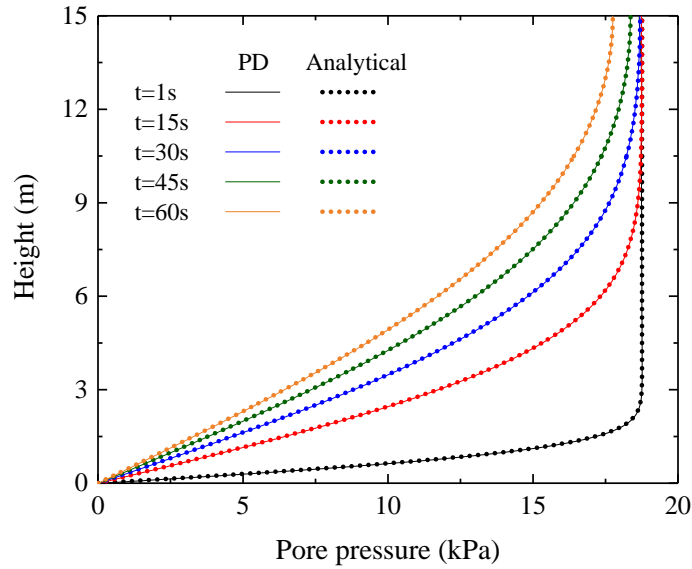


Figure V .4: Comparison of analytical and PD pore pressure along the region

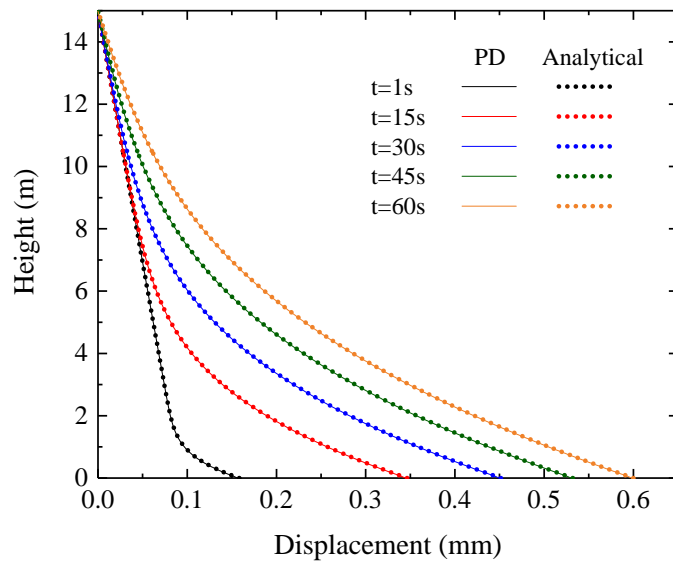


Figure V .5: Comparison of analytical and PD vertical displacements along the region

The obtained numerical results will be compared with the analytical solution in (Wang, 2000). The evolution of pore pressure and vertical displacement is given, respectively, in

Fig. V .5 and Fig. V .4. Due to the drainage of upper surface, the pore pressure decreases progressively with time in the sample. Meanwhile, the soil deformation increases gradually under the applied external stress  $P_0$ . As a result, the size of the soil column decreases and the soil consolidates. In general, a good agreement is obtained between the numerical results and analytical solution of Wang et al. (Wang, 2000).

### 4.1.2 Desaturation of a sand column

The drainage tests performed by Liakopoulos (Liakopoulos, 1964) is studied by using the proposed model. The studied structure is a fully saturated vertical sand column, measuring  $1m$  in height. Both lateral boards were restrained by rigid and impermeable walls while a high permeability sand stone was installed at the lower board of the column to support the specimen. In order to get a fully saturated, before testing, the upper surface of the column was continuously injected with a steady water flow until water freely drained out from the lower board of the column. At the beginning of the experiment, the water flow was cut off. The water then flows out from the lower board of the column. The distribution of pore pressure at different periods was measured.

In the numerical simulation, the initial conditions and boundary conditions are shown in the Fig. V .6. The materials parameters are listed in the Table. V .1. The column is discretized into uniform material points with a characteristic length of  $\Delta x = 0.01m$ . The horizon  $\delta$  is assumed as  $3.015\Delta x$ , and the time step size is chosen as  $\Delta t = 1.0 \times 10^{-4}s$ .

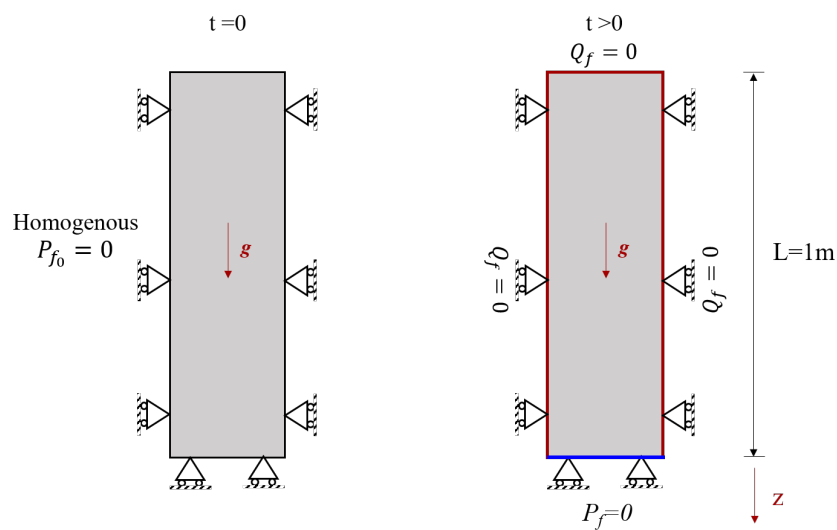


Figure V .6: Desaturation of a sand column: Geometry and boundary conditions

Porous solid density	$\rho$	1700kg/m <sup>3</sup>
Drained Young Modulus	$E_{sk}$	1300kPa
Drained Poisson coefficient	$\nu_{sk}$	0.4
Biot coefficient	$b$	1.0
Solid phase volumic stiffness	$K_s$	1000GPa
Single phase permeability	$k_f^{sat}$	$4.5 \times 10^{-7}$
Initial porosity	$n_0$	0.2975

**Table V .1:** Material parameters used in the numerical simulate (Callari and Abati, 2009)

Based on the experimental data provided by Liakopoulos, the water retention curve and the relative permeability to water are given as (Lewis and Schrefler, 1998)

$$S_l = 1 - (1.9722 \times 10^{-11})(-p_l)^{2.4279} \quad (\text{V .39})$$

$$k_r = 1 - 2.207(1 - S_l)^{1.021} \quad (\text{V .40})$$

The numerical results are given in Fig.V .7 and Fig.V .8. In Fig.V .7, the evolution of fluid pressures are studied. The obtained numerical results will be compared with the experimental data as well as the FEM solution (Callari and Abati, 2009). In general, a very good concordance is observed between the obtained PD numerical simulation results and the experimental data/the FEM solution. Due to the lack of available measurement of material properties, the approximate values are used in the numerical simulation. Therefore, there is a little difference between the numerical results and the experimental observation. The settlement of sand column is presented in Fig.V .8. Again, a good agreement is obtained between the obtained numerical results and the experimental observation/ FEM solution. In conclusion, the PD simulation successfully captures the experimental observations.



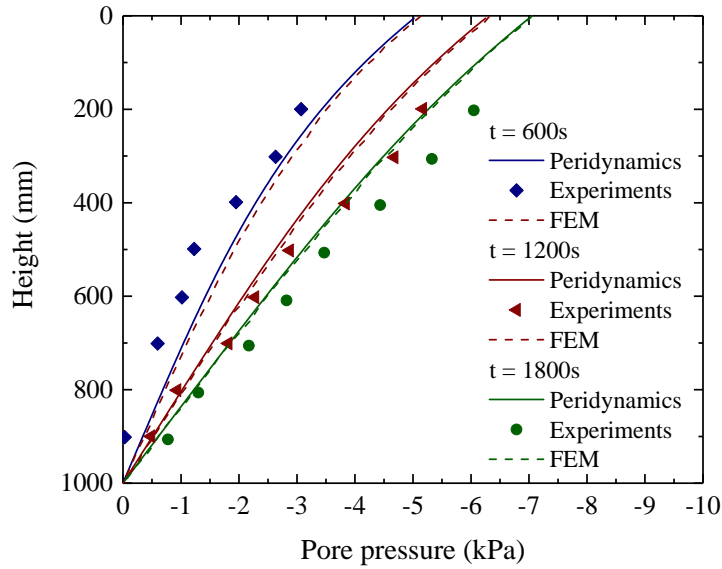


**Figure V .7:** Comparison between experimental data and numerical results with PD and FEM results: Evolution of fluid pressure

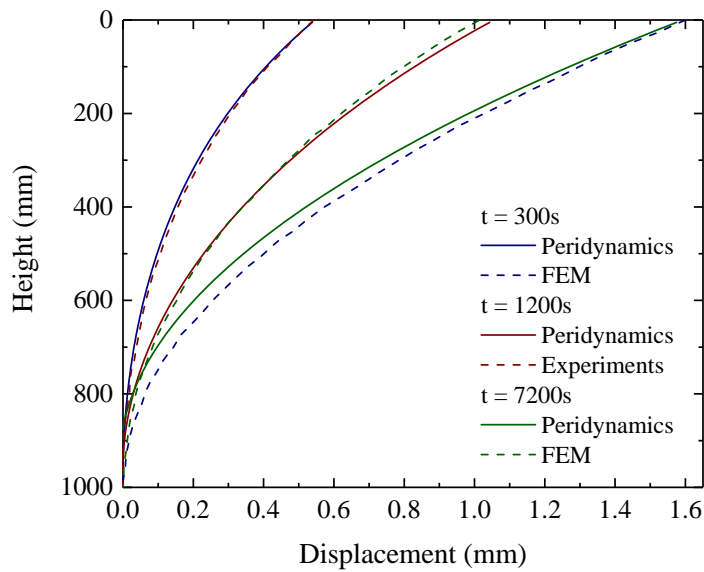


**Figure V .8:** Comparison of FEM and PD results: settlement of sand column

## 4.2 Numerical analysis of drying shrinkage cracking

In this section, we will study the drying shrinkage cracks in concrete-like materials by using the coupled hydro-mechanical PD model. The numerical simulations will be compared with the experimental study Chapter II 3.

### 4.2.1 Presentation of studied concrete-like composite

The drying shrinkage cracking in concrete-like material is studied in this section. All the numerical simulations are performed in 2D conditions. The cross-section in the middle of the scanned part of the specimen was selected to represent the micro-structure of the concrete composite. The cross sections of two types of specimens with 2 mm and 3 mm inclusions, respectively, are shown in Fig.V .9. And the dimensions for the model is  $20mm \times 20mm$ .

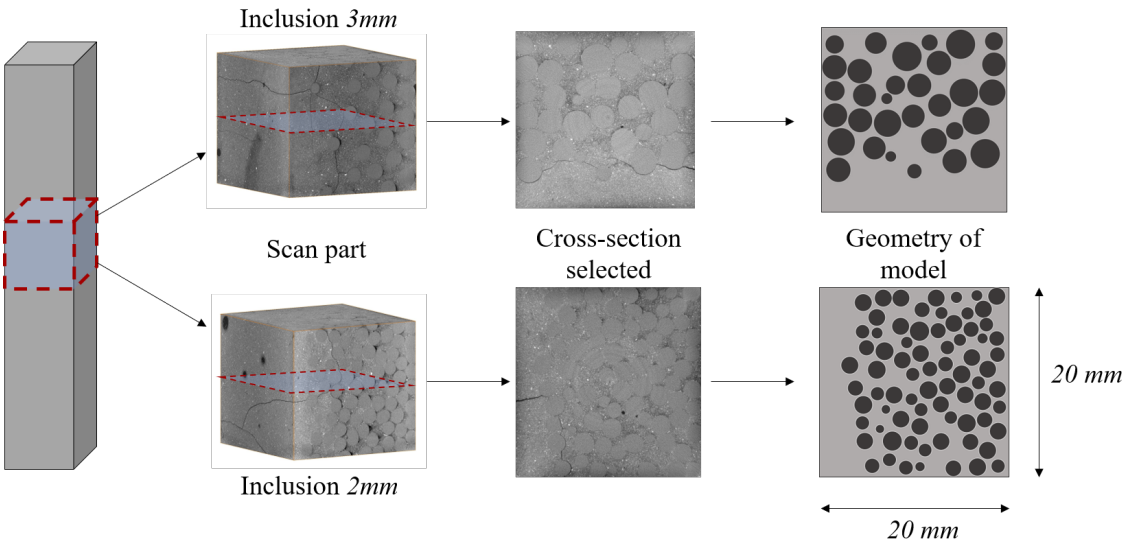


**Figure V .9:** Selected representative micro-structure of concrete composite for simplified 2D modelling

For PD modelling, the cross section is discretized into material  $200 \times 200$  particles with a characteristic length  $\Delta x = 0.1mm$ . The horizon  $\delta = 3.015\Delta x$ . Based on the experimental data and the work of Li (Li, 2016), the material properties used in the model are summarized in Table.V .2. Based on the experimental data of Rougelot et al. (Rougelot et al., 2009), the parameter values of the retention curve for cementitious material are:  $S_l^r = 0$ ,  $\epsilon = 2.09 \times 10^{-8}$ ,  $n = 1.9$ ,  $m = 0.47$ . Then the function of  $S_l$  can be

expressed as

$$S_l = [1 + (2.09 \times 10^{-8} p_c)^{1.9}]^{-0.47} \quad (\text{V .41})$$

In the drying tests, the saturated specimens are kept at a temperature of  $25^\circ\text{C}$  and a relative humidity of 12%. The relationship between hydraulic pressure and relative humidity is described by to the Kelvin's law:

$$p_f = -p_c = -\ln(H_r) \frac{p_f R T}{M} \quad (\text{V .42})$$

where  $H_r$  is the relative humidity,  $M$  is the molar volume of the liquid,  $R$  is the universal gas constant,  $T$  is temperature. Therefore, a humidity of 12% imposed on the outer contour of the samples is equal to a water pressure of  $-95.4\text{MPa}$ . In the numerical simulation, the aggregates are assumed to be linearly elastic and are always fully saturated.

Parameters	Cement paste	Aggregate
Young Modulus, $E(\text{GPa})$	15	68
Poisson coefficient, $\nu_{sk}$	1/3	1/3
Biot coefficient, $b$	0.63	-
Initial permeability, $k_f(\text{m}^2)$	$1.0 \times 10^{-18}$	$1.0 \times 10^{-23}$
Initial porosity, $n_0$	0.35	-
Density, $\rho(\text{kg}/\text{m}^3)$	1530	2500
Critical stretch, $s_0$	0.001	-

**Table V .2:** Material parameters used in the numerical simulations

#### 4.2.2 Simulations results

The distribution of pore pressures in the matrix is shown in Fig. V .10. It is observed that the obtained results of two specimens evolve in a similar manner. Because the glass inclusions are almost impermeable to water, the pore pressure in the inclusions can be considered as zero. The desaturation front penetrates progressively in the cement matrix until the matrix is completely desaturated. Finally, a uniform distribution of pore pressure is observed in the cement matrix, except a small zone near the inclusions. This observation is due to the impermeability of the inclusions.

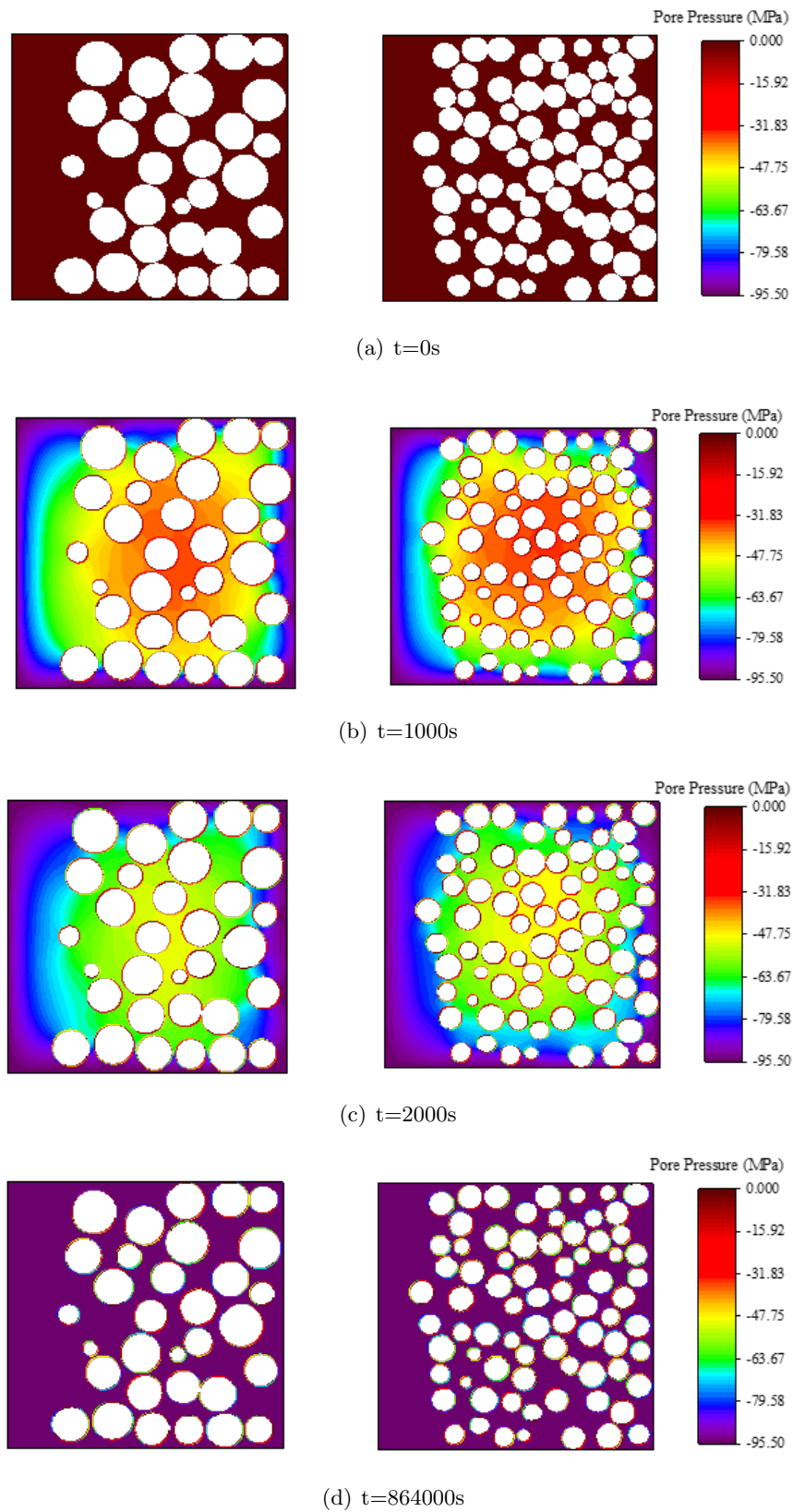
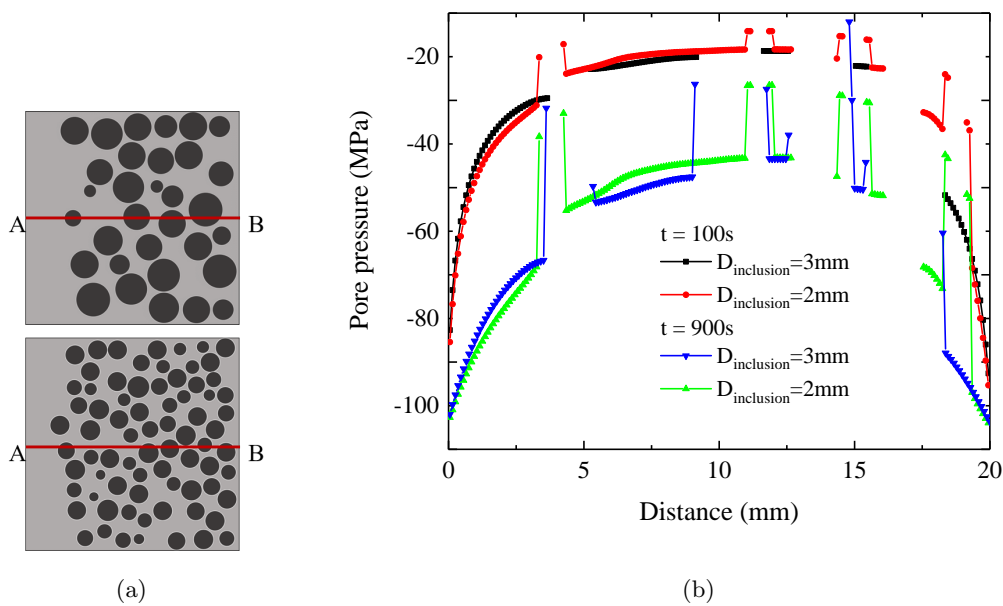
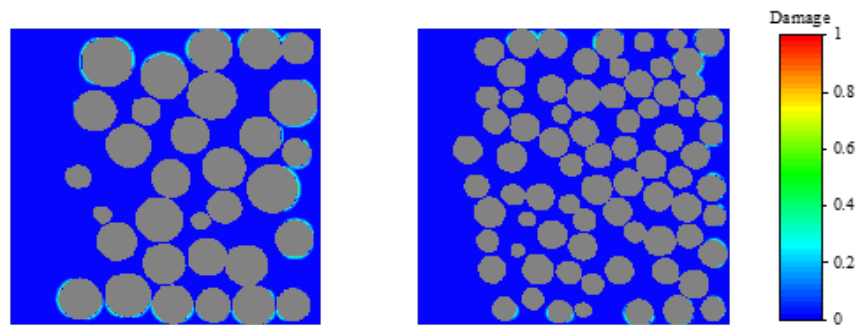


Figure V .10: Distribution of the pore pressure in two composites with different size of inclusions (left:3mm,right:2mm)

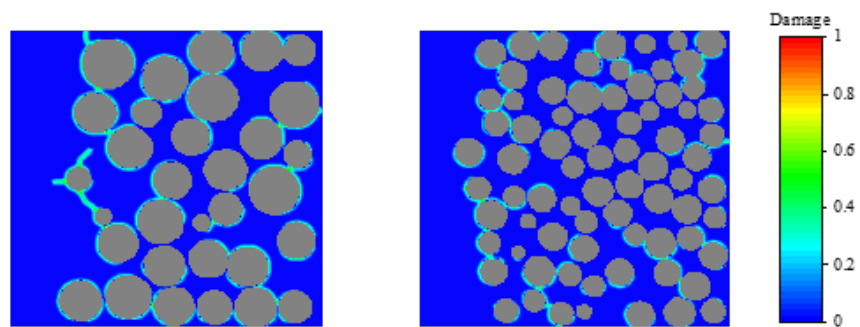
In Fig. V .11, the evolution of pore pressure in the middle of two types of specimen AB line is compared at two different drying times. A hydraulic gradient is generally observed between the surface and the center of the specimens during the drying process. This hydraulic gradient gradually decreases with the desaturation of cement paste. The discontinuities in each curve correspond to the presence of aggregates in the middle line analyzed. It's observed that the desaturation processes of cement paste around the inclusions are relatively slow with respected to the other positions of matrix. This observation can be captured by a non-uniform distribution of pore pressure around the inclusions Fig. V .10. At the end, the evolution of pore pressure in two types of specimens are compared at the same time. The obtained results are almost the same. We can conclude that the size of the inclusions has almost no effect on the drying process.



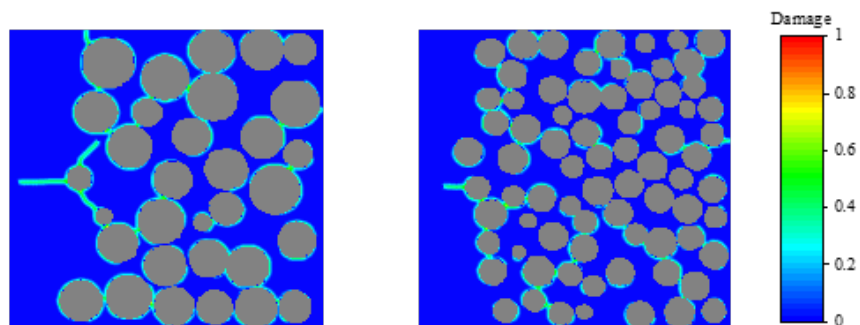
**Figure V .11:** (a) Location of line AB, (b) Evolution of pore pressure along the line AB



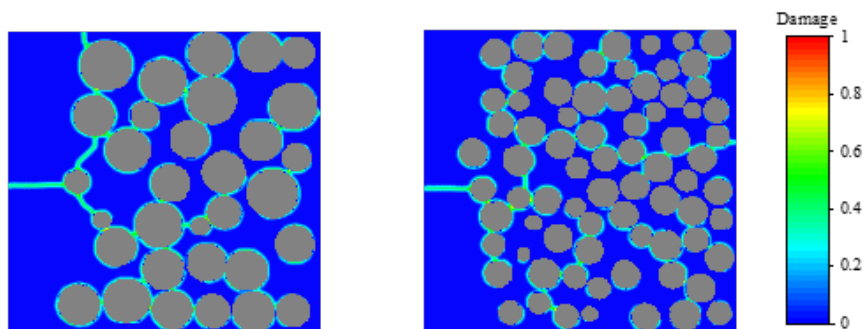
(a)  $t=100s$



(b)  $t=400s$



(c)  $t=600s$



(d)  $t=3000s$

**Figure V .12:** Damage distribution in two composites with different sizes of inclusions (left:3mm,right:2mm)

The damage distributions in two types of specimens are shown in Fig. V .12. At the beginning of drying, due to the great hydraulic gradient between the outside surface and the inner part of specimens, the cement matrix shrinks and the shrinkage of cement paste is constrained by the aggregate (see Fig. V .12(a)). Cracks then appear quickly at the interfaces between the aggregate and the cement matrix as well as in the cement matrix close to the outside surface and the aggregate. Afterwards, with the advancement of the drying front, the cracks propagate towards the inner part of the specimen. More circumferential cracks are observed around the aggregate as well as in the low-density aggregate zone, shown on the left side of the specimen (see Fig. V .12(b)). Two types of cracks are generally observed: circumferential cracks around the aggregate and radial cracks developing towards the surface of the specimen (see Fig. V .12(c) and V .12(d)). By comparing the damage distribution diagrams of two specimens, the pattern of drying shrinkage cracks is independent of the aggregate distribution or size. Moreover, the damage distribution patterns observed in the numerical simulations are coherent with that observed in the laboratory tests (Section. II 3). As the experimental observations have been obtained by using a scan resolution of  $18\mu m$ , cracks below this set resolution cannot be detected experimentally. Therefore, the number of cracks obtained in the simulation results is higher than that observed in the experimental results.

### 4.3 Influence of inclusion size on drying shrinkage cracks

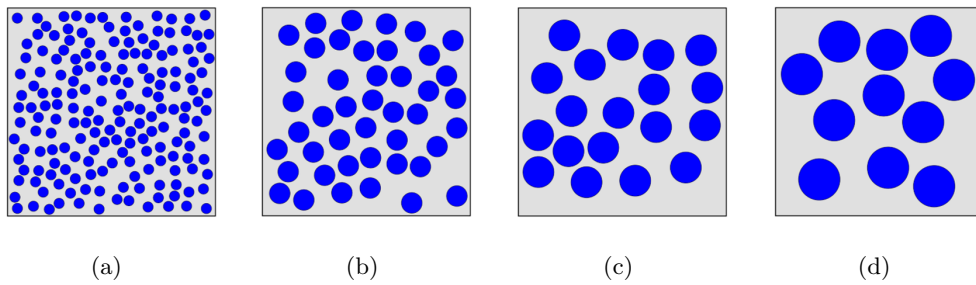


**Figure V .13:** Inclusions distribution in the numerical concrete-like composites for  $\rho_v = 35\%$  with different inclusion sizes  $\phi = 1mm$ , (b)  $\phi = 2mm$ , (c)  $\phi = 3mm$ , (d)  $\phi = 4mm$ ,

In order to study the influence of inclusions size on the drying micro-cracking in the cementitious materials, a parametric study is performed by using a series of concrete-like composite with a random inclusion distribution. In all the numerical simulations, a fixed aggregate volume fraction of  $\rho_v = 35\%$  is applied by using different aggregate diameters of  $\phi = 1mm, 2mm, 3mm, 4mm$  respectively. The inclusions distribution are shown in Fig.

V .13. The used model parameters, material properties and boundary conditions are the same as those of the previous section.

The cracking patterns of four numerical samples are shown in Fig.V .14. In general, the similar results are obtained in four cases, such as the random orientations of cracks, the appearance of partially bonded cracks around some aggregate particles, and matrix cracks connecting with several aggregate particles.

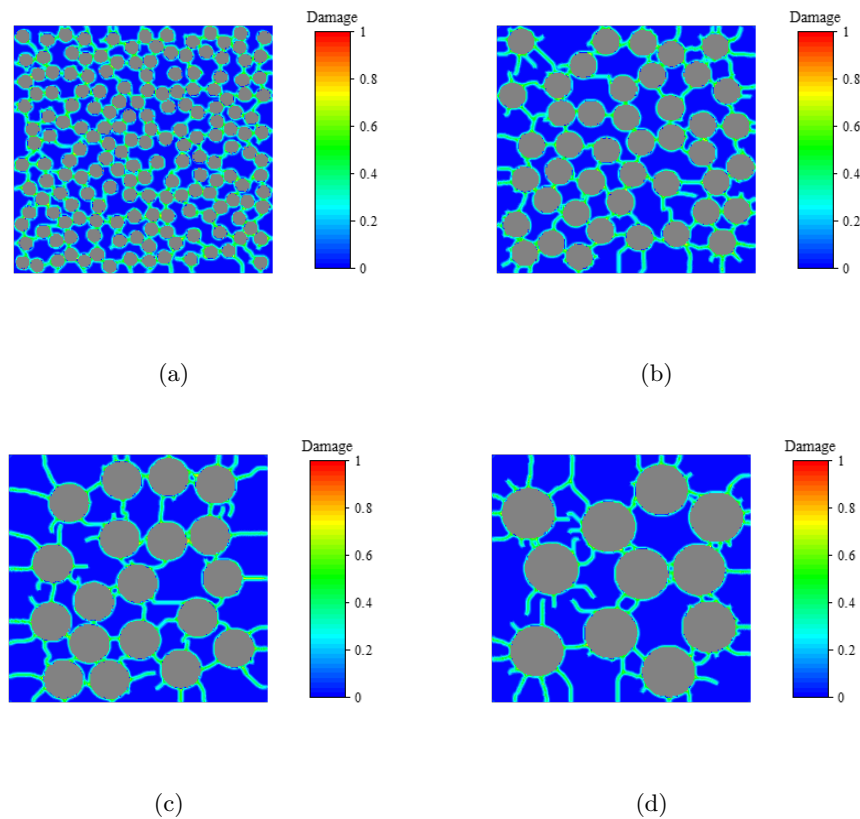


**Figure V .14:** Crack patterns of model for  $\rho_v = 35\%$  and (a)  $\phi = 1mm$ , (b)  $\phi = 2mm$ , (c)  $\phi = 3mm$ , (d)  $\phi = 4mm$ ,

By using the Eq. (IV .8) et Eq. (IV .9), the crack length and the average crack width can be obtained and are illustrated in the Fig. V .15. We can observe that the crack length decreases as the aggregate size increases, while the average crack width increases with the increasing of aggregate size.



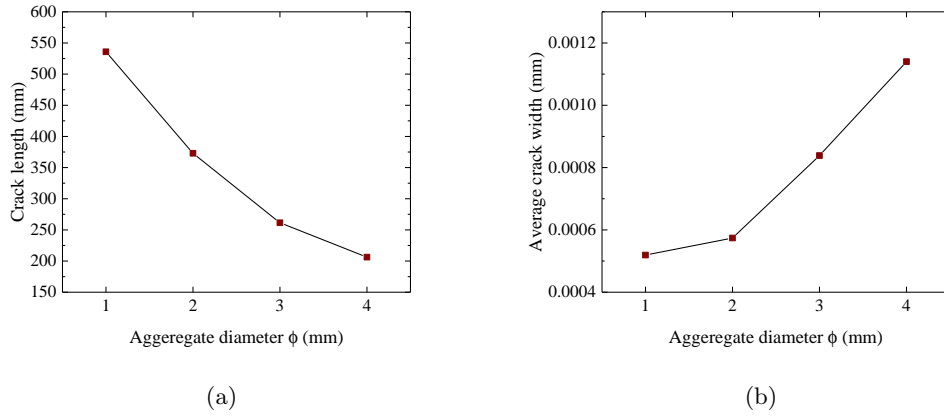


**Figure V .15:** (a) Crack length and (b) average crack width for different aggregates size

## 5 Concluding remarks

In this chapter, a fully coupled hydro-mechanical PD model is proposed for saturated and partially saturated porous media based on the bond-based PD theory. The proposed model is firstly validated by simulating two benchmark problems: the one-dimensional consolidation of soil sample and the one-dimensional drainage of a sand column.

After that, the PD partially saturated model is used to study the drying shrinkage cracking in cementitious material. The drying process and the evolution of drying shrinkage cracking are analyzed. In general, a consistent pattern of crack morphology is obtained between the numerical simulation results and the experimental observations.

Finally, an emphasis is put on the influence of the size of aggregates. A parametric analysis is performed by using different sizes of aggregates with the same volume fraction. The obtained numerical results show that aggregate size has no significant effect on the formation, propagation and distribution of cracks. The crack length decreases as the aggregate size increases while the average crack width increases with the increasing of aggregate size.



# Chapter VI

## Conclusions and Perspectives

### 1 Conclusions

In this thesis, the mechanism of drying induced cracking is studied via a series of experimental investigation and numerical modeling. The emphasis is put on the influences of inclusion size and stiffness on drying shrinkage-induced cracking in concrete composites. A series of experimental program have been firstly presented. Based on the experimental observations, the peridynamic theory has been used for the numerical analysis of the drying shrinkage-induced cracking in concrete composites. In the numerical simulation, a series of mechanical simulations has been firstly performed while the drying shrinkage is simulated as a imposed strain. Then, a fully coupled hydro-mechanical peridynamic model has been proposed and used to study the drying shrinkage cracks.

Based on the researches performed in the present work, the following main remarks can be obtained.

- Based on the X-ray micro-tomography of samples, it is shown that the cracks are mainly created around the interface between the inclusions and the matrix. Moreover, the distribution of cracks induced by dry shrinkage is independent on the inclusions size. However, by comparing the volume fraction of cracks and pores before and after drying, we can conclude that the quantity of drying shrinkage cracks increases with the increase of inclusions size. On the other hand, the restraining effects of inclusions during the drying processes increase with the Young's modulus of inclusions;
- Some parametric studies have been conducted in order to study the adopted numerical methods/models on the calculation accuracy and efficiency, such as horizon

particle density, grid size, and horizon size. And the bending of a two-dimensional concrete cantilever beam is used to valid the perforation of the developed bond-based PD code;

- The developed PD code is used to study the cracking process in heterogeneous materials. The good agreement obtained between the numerical simulation and experimental observation confirm that the proposed model and the developed code is able to satisfactorily predict the drying shrinkage cracks. The cracking patterns strongly depends on the difference of elastic stiffness between inclusions and cement past: for a given cement paste, the initiation and propagation of the drying shrinkage cracks increase with the rigidity of inclusions.
- A coupled hydro-mechanical PD model is proposed for the description of hydro-mechanical processes in saturated and partially saturated porous medium. The developed code and proposed model are firstly validated by simulating two benchmark problems. After that, they are used to study the drying shrinkage cracks. Again, a good concordance is obtained between the numerical simulations and experimental observations. The analysis of obtained results can help us to get a good understanding of the influence of inclusions on the drying shrinkage cracks. The larger the aggregate diameter is, the smaller the crack length and the larger the average crack width are observed.

## 2 Perspectives

This thesis focused on studying drying shrinkage cracking in cementitious materials. In order to identify the influence factors and understand the mechanism of cracks, a series of experimental and numerical programs have been performed. In the near future, these researches can be completed by the flowing:

- The XCMT technique allows us to get a real evolution/distribution of drying cracks and also can help us get a good understanding of the mechanisms controlling the shrinkage cracks. However, only the preliminary processing analysis of the XCMT scan results have been carried out in the present study. The comparative analysis with the numerical results is limited to a qualitative analysis. Therefore, more in-depth processing analysis of experimental results will be needed to obtain more quantitative analysis between experimental observations and numerical simulations.

For instance, the size of open crack can be estimated by using a dedicated algorithm or volume image correlation;

- The obtained experimental results exhibit that the presence of aggregate segregation strongly alters the evolution of drying cracks. Therefore, some certain techniques will be used to avoid this effect. For example, in the study of MALBOIS (Malbois, 2019), a viscosifying agent had been convincingly used to reduce segregation;
- According to the experimental investigation, the thermal expansion induced cracks should be characterized by suitable experimental methods in order to distinguish them from those induced by the drying shrinkage;
- the time-dependent deformation of the matrix phase (i.e. the aging viscoelasticity of the hardened cement paste, the characters of creep) will be considered in the numerical study;
- The obtained numerical results exhibit that the bond-based peridynamics is suitable to describe the cracking processes of elastic-brittle material. Moreover, it can be adapted to the failure behavior of different types of materials with a modification of the interaction force function. However, many simplifications used in the bond-based peridynamics are necessary to be enriched. For instance: the interaction between particles is oversimplified by a central potential that is completely independent of other local conditions and then induce a fixed Poisson's ratio. Moreover, in the mechanics of continuous media, the mechanical behaviour of material is described by the stress-strain tensor, while the bond-based peridynamics uses the interaction forces between particles. As a result, it is difficult to describe satisfactorily the mechanical behaviour of cementitious materials. Therefore, the state-based peridynamics theory proposed by Silling et al. (Silling et al., 2007) will be applied in the future study;
- For reason of simplicity, the permeability is assumed to be constant in the present study. However, an eventual increase of transport properties is generally observed in cracked materials. In view of this, the coupling between the induced damage and transport properties will be taken into account in the future study, for instance the intrinsic permeability, the mention curve and the relative permeability, etc...
- Although the simplified two-dimensional simulations have provided a good prediction of drying shrinkage cracks, three-dimensional simulations are still needed to get a more detailed description of cracking patterns and quantitative comparisons with

experimental results. Moreover, the real shape of aggregates is necessary to be taken into account in the future study;

- Although the peridynamic method has many advantages to reproduce numerically the drying cracking process in cementitious materials, the computational efficiency is still needed to be ameliorated, for example, by using parallel operations etc.

# Bibliography

- Aifantis, E. C. (1992). On the role of gradients in the localization of deformation and fracture. *International Journal of Engineering Science*, 30(10):1279–1299.
- Aifantis, E. C. (1999). Strain gradient interpretation of size effects. In *Fracture Scaling*, pages 299–314. Springer.
- Alam, S. Y., Saliba, J., and Loukili, A. (2014). Fracture examination in concrete through combined digital image correlation and acoustic emission techniques. *Construction and Building Materials*, 69:232–242.
- Almudaiheem, J. A. (1991). Prediction of drying shrinkage of portland cement paste: influence of shrinkage mechanisms. *Journal of King Saud University-Engineering Sciences*, 3(1):69–86.
- ANDRA (2005). Dossier 2005, référentiel du site meuse/haute-marne. andra. *Report n C. RP. ADS*, 4.
- Askari, E., Bobaru, F., Lehoucq, R., Parks, M., Silling, S. A., Weckner, O., et al. (2008). Peridynamics for multiscale materials modeling. In *Journal of Physics: Conference Series*, volume 125, page 012078. IOP Publishing.
- Barcelo, L., Moranville, M., and Clavaud, B. (2005). Autogenous shrinkage of concrete: a balance between autogenous swelling and self-desiccation. *Cement and Concrete Research*, 35(1):177–183.
- Barenblatt, G. I. et al. (1962). The mathematical theory of equilibrium cracks in brittle fracture. *Advances in applied mechanics*, 7(1):55–129.
- Baroghel-Bouny, V., Arnaud, S., Henry, D., Caracasses, M., and Quenard, D. (2002). Vieillissement des bétons en milieu naturel: une expérimentation pour le xxie siècle. iii-propriétés de durabilité des bétons mesurées sur éprouvettes conservées en laboratoire. *Bulletin des laboratoires des Ponts et Chaussées*, (241).
- Bauska, I. (1986). *Accuracy estimates and adaptive refinements in finite element computations*. John Wiley & Sons.

- Bazant, Z. P. (1984). Imbricate continuum and its variational derivation. *Journal of Engineering Mechanics*, 110(12):1693–1712.
- Bazant, Z. P. (1988). *Mathematical modeling of creep and shrinkage of concrete*. Wiley.
- Bazant, Z. P., Belytschko, T. B., Chang, T. P., et al. (1984). Continuum theory for strain-softening. *Journal of Engineering Mechanics*, 110(12):1666–1692.
- Bazant, Z. P. and Oh, B. H. (1983). Crack band theory for fracture of concrete. *Matériaux et construction*, 16(3):155–177.
- Bazant, Z. P. and Oh, B. H. (1985). Microplane model for progressive fracture of concrete and rock. *Journal of Engineering Mechanics*, 111(4):559–582.
- Bazant, Z. P., Tabbara, M. R., Kazemi, M. T., and Pijaudier-Cabot, G. (1990). Random particle model for fracture of aggregate or fiber composites. *Journal of engineering mechanics*, 116(8):1686–1705.
- Belytschko, T. and Black, T. (1999). Elastic crack growth in finite elements with minimal remeshing. *International journal for numerical methods in engineering*, 45(5):601–620.
- Belytschko, T., Lu, Y. Y., and Gu, L. (1994). Element-free galerkin methods. *International journal for numerical methods in engineering*, 37(2):229–256.
- Biot, M. A. (1941). General theory of three-dimensional consolidation. *Journal of applied physics*, 12(2):155–164.
- Bisschop, J., Pel, L., and Van Mier, J. (2001). Effect of aggregate size and paste volume on drying shrinkage microcracking in cement-based composites. *Creep, Shrinkage and Durability Mechanics of Concrete and other Quasi-Brittle Materials*, pages 75–80.
- Bisschop, J. and Van Mier, J. G. M. (2002a). Effect of aggregates on drying shrinkage microcracking in cement-based composites. *Materials and Structures*, 35(8):453–461.
- Bisschop, J. and Van Mier, J. G. M. (2002b). How to study drying shrinkage microcracking in cement-based materials using optical and scanning electron microscopy? *Cement and concrete research*, 32(2):279–287.
- Bissonnette, B., Pierre, P., and Pigeon, M. (1999). Influence of key parameters on drying shrinkage of cementitious materials. *Cement and Concrete Research*, 29(10):1655–1662.
- Bobaru, F. and Ha, Y. D. (2011). Adaptive refinement and multiscale modeling in 2d peridynamics.



- Bossart, P., Meier, P. M., Moeri, A., Trick, T., and Mayor, J. C. (2002). Geological and hydraulic characterisation of the excavation disturbed zone in the opalinus clay of the mont terri rock laboratory. *Engineering Geology*, 66(1-2):19–38.
- Breitenfeld, M. S., Geubelle, P. H., Weckner, O., and Silling, S. A. (2014). Non-ordinary state-based peridynamic analysis of stationary crack problems. *Computer Methods in Applied Mechanics and Engineering*, 272:233–250.
- Burlion, N., Bernard, D., and Chen, D. (2006). X-ray microtomography: application to microstructure analysis of a cementitious material during leaching process. *Cement and Concrete research*, 36(2):346–357.
- Burlion, N., Bourgeois, F., and Shao, J. F. (2005). Effects of desiccation on mechanical behaviour of concrete. *Cement and concrete composites*, 27(3):367–379.
- Butt, S. N., Timothy, J. J., and Meschke, G. (2017). Wave dispersion and propagation in state-based peridynamics. *Computational Mechanics*, 60(5):725–738.
- Callari, C. and Abati, A. (2009). Finite element methods for unsaturated porous solids and their application to dam engineering problems. *Computers & structures*, 87(7-8):485–501.
- Carpinteri, A. and Ingrassia, A. R. (2012). *Fracture mechanics of concrete: Material characterization and testing: Material Characterization and Testing*, volume 3. Springer Science & Business Media.
- Chen, P. W. and Chung, D. (1995). Effect of polymer addition on the thermal stability and thermal expansion of cement. *Cement and concrete research*, 25(3):465–469.
- Chen, X. T., Davy, C. A., Shao, J. F., and Skoczylas, F. (2010). Experimental and micro-mechanical analysis of the mechanical and transport properties of mortar containing heat-induced micro-cracks. *Cement and Concrete Composites*, 32(9):678–685.
- Cheng, C. C., Cheng, T. M., and Chiang, C. H. (2008). Defect detection of concrete structures using both infrared thermography and elastic waves. *Automation in Construction*, 18(1):87–92.
- Chiaia, B., Vervuurt, A. H. J. M., and Van Mier, J. G. M. (1997). Lattice model evaluation of progressive failure in disordered particle composites. *Engineering Fracture Mechanics*, 57(2-3):301–318.

- Coussy, O. (1995). *Mechanics of porous continua*. Wiley.
- Coussy, O. (2004). *Poromechanics*. John Wiley & Sons.
- Coussy, O., Eymard, R., and Lassabatère, T. (1998). Constitutive modeling of unsaturated drying deformable materials. *Journal of Engineering Mechanics*, 124(6):658–667.
- Cox, B. N., Gao, H., Gross, D., and Rittel, D. (2005). Modern topics and challenges in dynamic fracture. *Journal of the Mechanics and Physics of Solids*, 53(3):565–596.
- Creath, M., Newman, J., and Newman, K. (1969). The influence of aggregate particles on the local strain distribution and fracture mechanism of cement paste during drying shrinkage and loading to failure. *Matériaux et Construction*, 2(1):73–85.
- Cundall, P. A. and Hart, R. D. (1993). Numerical modeling of discontinua. In *Analysis and design methods*, pages 231–243. Elsevier.
- Cundall, P. A. and Strack, O. D. L. (1979). A discrete numerical model for granular assemblies. *geotechnique*, 29(1):47–65.
- Dela, B. F. and Stang, H. (2000). Two-dimensional analysis of crack formation around aggregates in high-shrinkage cement paste. *Engineering Fracture Mechanics*, 65(2-3):149–164.
- Diamond, S. (1986). The microstructure of cement paste in concrete. In *Proceedings of the 8th International Congress on the Chemistry of Cement*, volume 1, pages 113–121.
- Dougill, J. W. (1976). On stable progressively fracturing solids. *Zeitschrift für angewandte Mathematik und Physik ZAMP*, 27(4):423–437.
- Du, X. L., Jin, L., and Ma, G. W. (2013). A meso-scale analysis method for the simulation of nonlinear damage and failure behavior of reinforced concrete members. *International Journal of Damage Mechanics*, 22(6):878–904.
- Dugdale, D. S. (1960). Yielding of steel sheets containing slits. *Journal of the Mechanics and Physics of Solids*, 8(2):100–104.
- Duhem, P. (1893). Le potentiel thermodynamique et la pression hydrostatique. In *Annales scientifiques de l'École Normale Supérieure*, volume 10, pages 183–230.
- Edelen, D. G. B., Green, A. E., and Laws, N. (1971). Nonlocal continuum mechanics. *Archive for Rational Mechanics and Analysis*, 43(1):36–44.

- Edelen, D. G. B. and Laws, N. (1971). On the thermodynamics of systems with nonlocality. *Archive for Rational Mechanics and Analysis*, 43(1):24–35.
- Elaqra, H., Godin, N., Peix, G., R'Mili, M., and Fantozzi, G. (2007). Damage evolution analysis in mortar, during compressive loading using acoustic emission and x-ray tomography: Effects of the sand/cement ratio. *Cement and Concrete Research*, 37(5):703–713.
- Eringen, A. C. (1972). Linear theory of nonlocal elasticity and dispersion of plane waves. *International Journal of Engineering Science*, 10(5):425–435.
- Eringen, A. C. and Edelen, D. (1972). On nonlocal elasticity. *International journal of engineering science*, 10(3):233–248.
- Eringen, A. C. and Kim, B. S. (1974). Stress concentration at the tip of crack. *Mechanics Research Communications*, 1(4):233–237.
- Fathifazl, G., Razaqpur, A. G., Isgor, O. B., Abbas, A., Fournier, B., and Foo, S. (2011). Creep and drying shrinkage characteristics of concrete produced with coarse recycled concrete aggregate. *Cement and Concrete Composites*, 33(10):1026–1037.
- Fu, Y., Gu, P., Xie, P., and Beaudoin, J. (1994). Development of eigenstress due to drying shrinkage in hardened portland cement pastes: Thermomechanical analysis. *Cement and concrete research*, 24(6):1085–1091.
- Fuller, W. B. and Thompson, S. E. (1907). The laws of proportioning concrete.
- Gallucci, E., Scrivener, K., Groso, A., Stampanoni, M., and Margaritondo, G. (2007). 3d experimental investigation of the microstructure of cement pastes using synchrotron x-ray microtomography ( $\mu\text{ct}$ ). *Cement and Concrete Research*, 37(3):360–368.
- Garboczi, E. J. (1997). Stress, displacement, and expansive cracking around a single spherical aggregate under different expansive conditions. *Cement and concrete research*, 27(4):495–500.
- Garboczi, E. J. and Bentz, D. P. (1991). Digital simulation of the aggregate–cement paste interfacial zone in concrete. *Journal of materials Research*, 6(1):196–201.
- Gerstle, W., Sau, N., and Aguilera, E. (2007a). Micropolar peridynamic constitutive model for concrete.

- Gerstle, W., Sau, N., and Silling, S. A. (2005). Peridynamic modeling of plain and reinforced concrete structures. In *SMiRT18: 18th Int. Conf. Struct. Mech. React. Technol., Beijing*.
- Gerstle, W., Sau, N., and Silling, S. A. (2007b). Peridynamic modeling of concrete structures. *Nuclear engineering and design*, 237(12-13):1250–1258.
- Gerstle, W. H., Sau, N., and Sakhavand, N. (2009). On peridynamic computational simulation of concrete structures. *Special Publication*, 265:245–264.
- Ghorbel, A., Saintier, N., and Dhiab, A. (2011). Investigation of damage evolution in short glass fibers reinforced polyamide 6, 6 under tensile loading using infrared thermography. *Procedia Engineering*, 10:2123–2128.
- Goldman, L. W. (2007). Principles of ct: radiation dose and image quality. *Journal of nuclear medicine technology*, 35(4):213–225.
- Goltermann, P. (1995). Mechanical predictions of concrete deterioration; part 2: Classification of crack patterns. *Materials Journal*, 92(1):58–63.
- Grassl, P., Grégoire, D., Solano, L. R., and Pijaudier-Cabot, G. (2012). Meso-scale modelling of the size effect on the fracture process zone of concrete. *International Journal of Solids and Structures*, 49(13):1818–1827.
- Grassl, P., Wong, H. S., and Buenfeld, N. R. (2010). Influence of aggregate size and volume fraction on shrinkage induced micro-cracking of concrete and mortar. *Cement and concrete research*, 40(1):85–93.
- Griffith, A. A. (1921). Vi. the phenomena of rupture and flow in solids. *Philosophical transactions of the royal society of london. Series A, containing papers of a mathematical or physical character*, 221(582-593):163–198.
- Ha, Y. D. and Bobaru, F. (2010). Studies of dynamic crack propagation and crack branching with peridynamics. *International Journal of Fracture*, 162(1-2):229–244.
- Häfner, S., Eckardt, S., Luther, T., and Könke, C. (2006). Mesoscale modeling of concrete: Geometry and numerics. *Computers & structures*, 84(7):450–461.
- Hansen, W. and Almudaiheem, J. A. (1987). Ultimate drying shrinkage of concrete— influence of major parameters. *Materials Journal*, 84(3):217–223.

- Havlásek, P. and Jirásek, M. (2016). Multiscale modeling of drying shrinkage and creep of concrete. *Cement and concrete research*, 85:55–74.
- Hearn, N. (1999). Effect of shrinkage and load-induced cracking on water permeability of concrete. *Materials Journal*, 96(2):234–241.
- Helmuth, R. A. and Turk, D. H. (1967). The reversible and irreversible drying shrinkage of hardened portland cement and tricalcium silicate pastes. Technical report.
- Hillerborg, A., Modéer, M., and Petersson, P.-E. (1976). Analysis of crack formation and crack growth in concrete by means of fracture mechanics and finite elements. *Cement and concrete research*, 6(6):773–781.
- Hirsch, T. J. (1962). Modulus of elasticity of concrete affected by elastic moduli of cement paste matrix and aggregate. In *Journal Proceedings*, volume 59, pages 427–452.
- Hordijk, D. A. (1992). Tensile and tensile fatigue behaviour of concrete; experiments, modelling and analyses. *Heron*, 37(1).
- Hsu, T. T., Slate, F. O., Sturman, G. M., and Winter, G. (1963). Microcracking of plain concrete and the shape of the stress-strain curve. In *Journal Proceedings*, volume 60, pages 209–224.
- Hu, W., Ha, Y. D., and Bobaru, F. (2012). Peridynamic model for dynamic fracture in unidirectional fiber-reinforced composites. *Computer Methods in Applied Mechanics and Engineering*, 217:247–261.
- Hua, C., Acker, P., and Ehrlacher, A. (1995). Analyses and models of the autogenous shrinkage of hardening cement paste: I. modelling at macroscopic scale. *Cement and Concrete research*, 25(7):1457–1468.
- Huang, D., Lu, G., and Qiao, P. (2015a). An improved peridynamic approach for quasi-static elastic deformation and brittle fracture analysis. *International Journal of Mechanical Sciences*, 94:111–122.
- Huang, D., Lu, G. D., Wang, C. W., and Qiao, P. Z. (2015b). An extended peridynamic approach for deformation and fracture analysis. *Engineering Fracture Mechanics*, 141:196–211.
- Huang, Y. J., Yang, Z. J., Ren, W. Y., Liu, G. H., and Zhang, C. Z. (2015c). 3d meso-scale fracture modelling and validation of concrete based on in-situ x-ray computed

- tomography images using damage plasticity model. *International Journal of Solids and Structures*, 67:340–352.
- Idiart, A., Bisschop, J., Caballero, A., and Lura, P. (2012). A numerical and experimental study of aggregate-induced shrinkage cracking in cementitious composites. *Cement and Concrete Research*, 42(2):272–281.
- Idiart, A. E. (2009). *Coupled analysis of degradation processes in concrete specimens at the meso-level*. Universitat Politècnica de Catalunya.
- Jamet, P., Millard, A., and Nahas, G. (1984). Triaxial behaviour of a micro-concrete complete stress-strain curves for confining pressures ranging from 0 to 100 mpa. Technical report, CEA Centre d'Etudes Nucleaires de Saclay.
- Jenabidehkordi, A., Abadi, R., and Rabczuk, T. (2020). Computational modeling of meso-scale fracture in polymer matrix composites employing peridynamics. *Composite Structures*, 253:112740.
- Jia, Y. (2006). *Contribution à la modélisation thermo-hydro-mécanique des roches partiellement saturées: application au stockage des déchets radioactifs*. PhD thesis, Lille 1.
- Jin, L., Du, X. L., and Ma, G. W. (2012). Macroscopic effective moduli and tensile strength of saturated concrete. *Cement and Concrete Research*, 42(12):1590–1600.
- Jivkov, A. P., Engelberg, D. L., Stein, R., and Petkovski, M. (2013). Pore space and brittle damage evolution in concrete. *Engineering Fracture Mechanics*, 110:378–395.
- Kamel, K. E. M., Colliat, J. B., Gerard, P., and Massart, T. J. (2020). Comparison of advanced discretization techniques for image-based modelling of heterogeneous porous rocks. *Acta Geotechnica*, 15(1):57–77.
- Kamel, K. E. M., Sonon, B., and Massart, T. J. (2019). An integrated approach for the conformal discretization of complex inclusion-based microstructures. *Computational mechanics*, 64(4):1049–1071.
- Kaplan, M. F. (1961). Crack propagation and the fracture of concrete. In *Journal Proceedings*, volume 58, pages 591–610.
- Kesler, C. E., Naus, D. J., and Lott, J. L. (1972). Fracture mechanics-its applicability to concrete. In *Proceedings of the Society of Materials Science Conference on the Mechanical Behavior of Materials.*, number Conf Paper.

- Kilic, B. (2008). Peridynamic theory for progressive failure prediction in homogeneous and heterogeneous materials.
- Kim, J., Jeong, S., and Regueiro, R. A. (2012). Instability of partially saturated soil slopes due to alteration of rainfall pattern. *Engineering Geology*, 147:28–36.
- Klein, P. A., Foulk, J. W., Chen, E. P., Wimmer, S., and Gao, H. J. (2001). Physics-based modeling of brittle fracture: cohesive formulations and the application of meshfree methods. *Theoretical and Applied Fracture Mechanics*, 37(1-3):99–166.
- Knab, L. I., Walker, H. N., Clifton, J. R., and Fuller J r, E. R. (1984). Fluorescent thin sections to observe the fracture zone in mortar. *Cement and concrete research*, 14(3):339–344.
- Krajcinovic, D. and Fonseka, G. U. (1981). The continuous damage theory of brittle materials, part 1 and part 2.
- Kumar, R. and Bhattacharjee, B. (2003). Porosity, pore size distribution and in situ strength of concrete. *Cement and concrete research*, 33(1):155–164.
- Kunin, I. A. (1982). *Elastic media with microstructure I: one-dimensional models*, volume 26. Berlin-Heidelberg-New York, Springer-Verlag.
- Kunin, I. A. (1984). *Elastic Media with Microstructure II. Three-Dimensional Models*, volume 64.
- Landis, E. N. and Nagy, E. N. (2000). Three-dimensional work of fracture for mortar in compression. *Engineering Fracture Mechanics*, 65(2-3):223–234.
- Latiere, H. and Mazerolle, F. (1987). The x-ray scanner. a tool for the examination of the intravoluminal crystalline state of aluminum. *Engineering Fracture Mechanics*, 27(4):413–463.
- Le, Q. V. and Bobaru, F. (2018). Surface corrections for peridynamic models in elasticity and fracture. *Computational Mechanics*, 61(4):499–518.
- Lewis, R. W. and Schrefler, B. A. (1998). *The finite element method in the static and dynamic deformation and consolidation of porous media*. Number BOOK. John Wiley.
- Li, L. (2016). *Etude de la fissuration engendrée par le séchage dans les matériaux cimentaires: influence des inclusions*. PhD thesis, Lille 1.

- Li, L., Jia, Y., Rougelot, T., and Burlion, N. (2018). Effects of inclusion stiffness on the cracking of cement-based composites under drying: a numerical study. *European Journal of Environmental and Civil Engineering*, 22(sup1):s246–s268.
- Li, L., Jin, Y. D., Jia, Y., Rougelot, T., Burlion, N., and Shao, J. F. (2020). Influence of inclusion rigidity on shrinkage induced micro-cracking of cementitious materials. *Cement and Concrete Composites*, page 103773.
- Li, W. J. and Guo, L. (2018). Meso-fracture simulation of cracking process in concrete incorporating three-phase characteristics by peridynamic method. *Construction and Building Materials*, 161:665–675.
- Li, X., Xu, Y., and Chen, S. h. (2016). Computational homogenization of effective permeability in three-phase mesoscale concrete. *Construction and Building Materials*, 121:100–111.
- Liakopoulos, A. C. (1964). *Transient flow through unsaturated porous media*. PhD thesis, University of California, Berkeley.
- Limodin, N., Rougelot, T., and Hosdez, J. (2020). Isis4d - in situ innovative set-ups under x-ray microtomography. *isis4d.univ-lille.fr*.
- Liu, G. R. and Gu, Y. T. (2005). *An introduction to meshfree methods and their programming*. Springer Science & Business Media.
- Liu, L., Shen, D. J., Chen, H. s., and Xu, W. X. (2014). Aggregate shape effect on the diffusivity of mortar: a 3d numerical investigation by random packing models of ellipsoidal particles and of convex polyhedral particles. *Computers & structures*, 144:40–51.
- Løland, K. E. (1980). Continuous damage model for load-response estimation of concrete. *Cement and Concrete Research*, 10(3):395–402.
- Lu, S., Landis, E., and Keane, D. (2006). X-ray microtomographic studies of pore structure and permeability in portland cement concrete. *Materials and structures*, 39(6):611–620.
- Madenci, E. and Oterkus, E. (2014). *Peridynamic theory and its applications*, volume 17. Springer.
- Malbois, M. (2019). *Analyse multi-échelle des déformations différées dans les matériaux cimentaires sous dessiccation ou réaction sulfatique interne*. PhD thesis, Université Paris-Saclay.



- Malek, A., Scott, A., Pampanin, S., and MacRae, G. (2017). Post-event damage assessment of concrete using the fluorescent microscopy technique. *Cement and Concrete Research*, 102:203–211.
- Mazars, J. (1984). Application de la mécanique de l'endommagement au comportement non linéaire et à la rupture du béton de structure. *THESE DE DOCTEUR ES SCIENCES PRESENTEE A L'UNIVERSITE PIERRE ET MARIE CURIE-PARIS 6*.
- Mindlin, R. D. (1963). Microstructure in linear elasticity. Technical report, Columbia Univ New York Dept of Civil Engineering and Engineering Mechanics.
- Moës, N., Dolbow, J., and Belytschko, T. (1999). A finite element method for crack growth without remeshing. *International journal for numerical methods in engineering*, 46(1):131–150.
- Mohamed, A. R. and Hansen, W. (1999). Micromechanical modeling of concrete response under static loading—part 1: model development and validation. *Materials Journal*, 96(2):196–203.
- Neto, A. A. M., Cincotto, M. A., and Repette, W. (2008). Drying and autogenous shrinkage of pastes and mortars with activated slag cement. *Cement and Concrete Research*, 38(4):565–574.
- Neville, A. M. (1959). Some aspects of the strength of concrete. *Civil Engineering (London)*, 54:1153–5.
- Ngo, D. and Scordelis, A. C. (1967). Finite element analysis of reinforced concrete beams. In *Journal Proceedings*, volume 64, pages 152–163.
- Nguyen, T., Ghazlan, A., Kashani, A., Bordas, S., and Ngo, T. (2018). 3d meso-scale modelling of foamed concrete based on x-ray computed tomography. *Construction and Building Materials*, 188:583–598.
- Ni, T., Zhu, Q. z., Zhao, L.-Y., and Li, P.-F. (2018). Peridynamic simulation of fracture in quasi brittle solids using irregular finite element mesh. *Engineering Fracture Mechanics*, 188:320–343.
- Ohno, K. and Ohtsu, M. (2010). Crack classification in concrete based on acoustic emission. *Construction and Building Materials*, 24(12):2339–2346.
- Omar, T. and Nehdi, M. L. (2017). Remote sensing of concrete bridge decks using unmanned aerial vehicle infrared thermography. *Automation in Construction*, 83:360–371.

- Oñate, E. and Rojek, J. (2004). Combination of discrete element and finite element methods for dynamic analysis of geomechanics problems. *Computer methods in applied mechanics and engineering*, 193(27-29):3087–3128.
- Oterkus, S. (2015). Peridynamics for the solution of multiphysics problems.
- Oterkus, S., Madenci, E., and Oterkus, E. (2017). Fully coupled poroelastic peridynamic formulation for fluid-filled fractures. *Engineering geology*, 225:19–28.
- Ozbek, A. S. A., Pedersen, R. R., Weerheijm, J., and van Breugel, K. (2019). Mesoscopic modeling of the impact behavior and fragmentation of porous concrete. *Cement and Concrete Composites*, 102:116–133.
- Peron, H., Hueckel, T., Laloui, L., and Hu, L. (2009). Fundamentals of desiccation cracking of fine-grained soils: experimental characterisation and mechanisms identification. *Canadian Geotechnical Journal*, 46(10):1177–1201.
- Rao, B. N. and Rahman, S. (2000). An efficient meshless method for fracture analysis of cracks. *Computational mechanics*, 26(4):398–408.
- Rashid, Y. R. (1968). Ultimate strength analysis of prestressed concrete pressure vessels. *Nuclear engineering and design*, 7(4):334–344.
- Ren, W., Yang, Z., Sharma, R., McDonald, S. A., and Mummary, P. M. (2018). Three-dimensional in situ xct characterisation and fe modelling of cracking in concrete. *Complexity*, 2018.
- Ren, W., Yang, Z., Sharma, R., Zhang, C. H., and Withers, P. J. (2015). Two-dimensional x-ray ct image based meso-scale fracture modelling of concrete. *Engineering Fracture Mechanics*, 133:24–39.
- Rice, J. R. (1968). A path independent integral and the approximate analysis of strain concentration by notches and cracks.
- Rodrigues, E. A., Manzoli, O. L., and Bitencourt Jr, L. A. (2020). 3d concurrent multiscale model for crack propagation in concrete. *Computer Methods in Applied Mechanics and Engineering*, 361:112813.
- Rougelot, T., Burlion, N., Bernard, D., and Skoczylas, F. (2010). About microcracking due to leaching in cementitious composites: X-ray microtomography description and numerical approach. *Cement and concrete research*, 40(2):271–283.

- Rougelot, T., Skoczylas, F., and Burlion, N. (2009). Water desorption and shrinkage in mortars and cement pastes: experimental study and poromechanical model. *Cement and Concrete Research*, 39(1):36–44.
- Rountree, C. L., Kalia, R. K., Lidorikis, E., Nakano, A., Van Brutzel, L., and Vashishta, P. (2002). Atomistic aspects of crack propagation in brittle materials: Multimillion atom molecular dynamics simulations. *Annual Review of Materials Research*, 32(1):377–400.
- Samouh, H., Rozière, E., and Loukili, A. (2018). Shape effect on drying behavior of cement-based materials: Mechanisms and numerical analysis. *Cement and Concrete Research*, 110:42–51.
- Sánchez, P. J., Huespe, A. E., Oliver, J., Diaz, G., and Sonzogni, V. E. (2012). A macroscopic damage-plastic constitutive law for modeling quasi-brittle fracture and ductile behavior of concrete. *International journal for numerical and analytical methods in geomechanics*, 36(5):546–573.
- Schlangen, E. and Garboczi, E. J. (1997). Fracture simulations of concrete using lattice models: computational aspects. *Engineering fracture mechanics*, 57(2-3):319–332.
- Schlangen, E. and Van Mier, J. G. M. (1992). Simple lattice model for numerical simulation of fracture of concrete materials and structures. *Materials and Structures*, 25(9):534–542.
- Scrivener, K. L., Crumbie, A. K., and Laugesen, P. (2004). The interfacial transition zone (itz) between cement paste and aggregate in concrete. *Interface science*, 12(4):411–421.
- Seleson, P., Parks, M., et al. (2011). On the role of the influence function in the peridynamic theory. *International Journal of Multiscale Computational Engineering*, 9(6):689–706.
- Sfer, D., Carol, I., Gettu, R., and Etse, G. (2002). Study of the behavior of concrete under triaxial compression. *Journal of engineering mechanics*, 128(2):156–163.
- Shao, J. F., Zhou, H., and Chau, K. T. (2005). Coupling between anisotropic damage and permeability variation in brittle rocks. *International Journal for Numerical and Analytical Methods in Geomechanics*, 29(12):1231–1247.
- Sheng, P., Zhang, J., and Ji, Z. (2016). An advanced 3d modeling method for concrete-like particle-reinforced composites with high volume fraction of randomly distributed particles. *Composites Science and Technology*, 134:26–35.

- Shi, H., Hosdez, J., Rougelot, T., Xie, S., Shao, J. f., Talandier, J., and Lacidogna, G. (2020). Digital volume correlation applied to x-ray micro-tomography images in uniaxial creep tests on anisotropic clayey rock. *Applied Sciences*, 10(14):4898.
- Shiotani, T., Bisschop, J., and Van Mier, J. G. M. (2003). Temporal and spatial development of drying shrinkage cracking in cement-based materials. *Engineering Fracture Mechanics*, 70(12):1509–1525.
- Sidoroff, F. and Dogui, A. (2001). Some issues about anisotropic elastic–plastic models at finite strain. *International journal of solids and structures*, 38(52):9569–9578.
- Silling, S. A. (2000). Reformulation of elasticity theory for discontinuities and long-range forces. *Journal of the Mechanics and Physics of Solids*, 48(1):175–209.
- Silling, S. A. (2010). Linearized theory of peridynamic states. *Journal of Elasticity*, 99(1):85–111.
- Silling, S. A. and Askari, E. (2005). A meshfree method based on the peridynamic model of solid mechanics. *Computers & structures*, 83(17-18):1526–1535.
- Silling, S. A., Demmie, P. N., Cole, R. A., and Taylor, P. (2006). Emu user’s manual. *Sandia National Laboratories, Albuquerque, NM*.
- Silling, S. A., Epton, M., Weckner, O., Xu, J., and Askari, E. (2007). Peridynamic states and constitutive modeling. *Journal of Elasticity*, 88(2):151–184.
- Silling, S. A. and Lehoucq, R. B. (2010). Peridynamic theory of solid mechanics. *Advances in applied mechanics*, 44:73–168.
- Sukumar, N. and Prévost, J.-H. (2003). Modeling quasi-static crack growth with the extended finite element method part i: Computer implementation. *International journal of solids and structures*, 40(26):7513–7537.
- Szczesniak, M., Rougelot, T., Burlion, N., and Shao, J.-F. (2013). Compressive strength of cement-based composites: Roles of aggregate diameter and water saturation degree. *Cement and Concrete Composites*, 37:249–258.
- Tal, D. and Fish, J. (2018). Stochastic multiscale modeling and simulation framework for concrete. *Cement and Concrete Composites*, 90:61–81.
- Underwood, P. (1986). Dynamic relaxation. *Computational method for transient analysis*, 1:245–263.

- Unger, J. F. and Eckardt, S. (2011). Multiscale modeling of concrete. *Archives of Computational Methods in Engineering*, 18(3):341.
- Van Genuchten, M. T. (1980). A closed-form equation for predicting the hydraulic conductivity of unsaturated soils. *Soil science society of America journal*, 44(5):892–898.
- Van Mier, J. G. M. (1996). *Fracture processes of concrete*, volume 12. CRC press.
- Vaunat, J., Jommi, C., Gens, A., et al. (1997). A strategy for numerical analysis of the transition between saturated and unsaturated flow conditions.
- Wang, H. F. (2000). *Theory of linear poroelasticity with applications to geomechanics and hydrogeology*, volume 2. Princeton University Press.
- Wang, X. F., Yang, Z. J., Yates, J. R., Jivkov, A. P., and Zhang, C. H. (2015). Monte carlo simulations of mesoscale fracture modelling of concrete with random aggregates and pores. *Construction and Building Materials*, 75:35–45.
- Wang, X. F., Zhang, M. Z., and Jivkov, A. P. (2016). Computational technology for analysis of 3d meso-structure effects on damage and failure of concrete. *International Journal of Solids and Structures*, 80:310–333.
- Wang, Y. T., Zhou, X. P., and Kou, M. M. (2018). A coupled thermo-mechanical bond-based peridynamics for simulating thermal cracking in rocks. *International Journal of Fracture*, 211(1-2):13–42.
- Wang, Z. M., Kwan, A. K. H., and Chan, H. C. (1999). Mesoscopic study of concrete i: generation of random aggregate structure and finite element mesh. *Computers & structures*, 70(5):533–544.
- Warren, T. L., Silling, S. A., Askari, A., Weckner, O., Epton, M. A., and Xu, J. (2009). A non-ordinary state-based peridynamic method to model solid material deformation and fracture. *International Journal of Solids and Structures*, 46(5):1186–1195.
- Wells, A. A. (1961). Crack propagation symposium proceedings. *Cranfield College of Aeronautics*, 1:210.
- Wittmann, F., Roelfstra, P., and Sadouki, H. (1985). Simulation and analysis of composite structures. *Materials science and engineering*, 68(2):239–248.
- Wittmann, F. H. (1983). Structure of concrete with respect to crack formation. *Fracture mechanics of concrete*, 43(5):6.

- Wittmann, F. H. and Roelfstra, P. E. (1980). Total deformation of loaded drying concrete. *Cement and Concrete Research*, 10(5):601–610.
- Wong, H., Zobel, M., Buenfeld, N., and Zimmerman, R. (2009). Influence of the interfacial transition zone and microcracking on the diffusivity, permeability and sorptivity of cement-based materials after drying. *Magazine of Concrete Research*, 61(8):571–589.
- Wriggers, P. and Moftah, S. O. (2006). Mesoscale models for concrete: Homogenisation and damage behaviour. *Finite elements in analysis and design*, 42(7):623–636.
- Xu, X.-P. and Needleman, A. (1994). Numerical simulations of fast crack growth in brittle solids. *Journal of the Mechanics and Physics of Solids*, 42(9):1397–1434.
- Xu, Y. and Chen, S. h. (2016). A method for modeling the damage behavior of concrete with a three-phase mesostructure. *Construction and Building Materials*, 102:26–38.
- Yaghoobi, A., Chorzepa, M. G., Kim, S. S., et al. (2017). Mesoscale fracture analysis of multiphase cementitious composites using peridynamics. *Materials*, 10(2):162.
- Yang, J., Wang, F. Z., Liu, Z. C., Liu, Y. P., and Hu, S. G. (2019). Early-state water migration characteristics of superabsorbent polymers in cement pastes. *Cement and Concrete Research*, 118:25–37.
- Yang, Z. and Xu, X. F. (2008). A heterogeneous cohesive model for quasi-brittle materials considering spatially varying random fracture properties. *Computer methods in applied mechanics and engineering*, 197(45-48):4027–4039.
- Yang, Z. j., Ren, W., Sharma, R., McDonald, S., Mostafavi, M., Vertyagina, Y., and Marrow, T. J. (2017). In-situ x-ray computed tomography characterisation of 3d fracture evolution and image-based numerical homogenisation of concrete. *Cement and Concrete Composites*, 75:74–83.
- Yurtdas, I., Burlion, N., Shao, J. F., and Li, A. (2011). Evolution of the mechanical behaviour of a high performance self-compacting concrete under drying. *Cement and Concrete Composites*, 33(3):380–388.
- Zheng, J. J., Li, C. Q., and Zhou, X. Z. (2005). Thickness of interfacial transition zone and cement content profiles around aggregates. *Magazine of Concrete Research*, 57(7):397–406.

- 
- Zhou, X. P., Wang, Y. T., and Shou, Y. D. (2020). Hydromechanical bond-based peridynamic model for pressurized and fluid-driven fracturing processes in fissured porous rocks. *International Journal of Rock Mechanics and Mining Sciences*, 132:104383.